# FIRST-PRINCIPLES STUDY ON HARD/SOFT $SmCo_5$/Co(Fe) NANOCOMPOSITE MAGNETIC MATERIALS

by

DANGXIN WU

Presented to the Faculty of the Graduate School of

The University of Texas at Arlington in Partial Fulfillment

of the Requirements

for the Degree of

DOCTOR OF PHILOSOPHY

THE UNIVERSITY OF TEXAS AT ARLINGTON

AUGUST 2008

ACKNOWLEDGEMENTS

I sincerely appreciate the guidance and support of my supervisor Dr. Qiming Zhang for the last five years. This dissertation would not be possible without his efforts, time and help. I would also like to thank Dr. Nail Fazleev, Dr. Asok K. Ray, Dr. Ping Liu and Dr. Manfred Cuntz for serving in my dissertation defense committee.

I am thankful to all the faculty and staff of the Physics Department for providing me with their help and support in various ways during the years. I would also like to express my gratitude to my colleagues and friends both in this department and in China for their encouragements, discussions and sharing in my study, my research and my life.

Last but not the least, special thanks to my family, especially my wife Jinli Li, for their love, support and encouragement.

This work was supported in part by the U.S. DoD/MURI under the Grant No. N00014-05-1-0497.

July 2, 2008

# ABSTRACT

## FIRST-PRINCIPLES STUDY ON HARD/SOFT $SmCo_5$/Co(Fe) NANOCOMPOSITE MAGNETIC MATERIALS

Dangxin Wu, PhD.

The University of Texas at Arlington, 2008

Supervising Professor: Qiming Zhang

More than a decade ago, exchange-spring permanent magnets containing soft and hard magnetic phases have been proposed to enlarge maximum energy product values through exchange coupling between the magnetically soft and hard phases. Indeed some later experiments have shown some promises in this regard. However, there are still many pending fundamental issues in the understanding and enhancement of the exchange coupling. In this dissertation, we have performed first-principles study based on the density functional theory to tackle some of these issues, including the effects of soft phase properties and interfacial conditions on the exchange coupling, using $SmCo_5$ as hard phase material and Co (CoFe) as soft phase material.

On the soft phase effects, we have investigated the structural, electronic and magnetic properties of FeCo alloys and found that the alloys are only stable in bcc-type structures and prefer chemically non-cubic geometries in a wide composition range. Due to this non-cubic preference, appreciable uniaxial magnetic anisotropy energies have been produced, which consequently facilitates the inter-phase magnetic interaction and enhances the overall magnetization in exchange-coupled nanocomposite systems.

On the interface effects, we have constructed a $SmCo_5$/Co multilayer model system with optimized atomic structure. The non-collinear magnetic structures were calculated to explore the exchange coupling dependence on the variation of the atomic composition across the interface. It is found that the inter-phase exchange coupling is strongly dependent on the interfacial conditions between the hard and soft phases.

We have also investigated the possibility of FeCo nanowires as potential high performance permanent magnets considering their high shape anisotropy. We studied the electronic structure and magnetic properties of FeCo nanowires and calculated their magnetocrystalline anisotropy energies and shape anisotropy energies.

TABLE OF CONTENTS

LIST OF ILLUSTRATIONS

LIST OF TABLES

# CHAPTER 1

# INTRODUCTION

Permanent or hard magnetic materials have been playing a very important part in modern technology and they are indispensable in our modern life. They are used to fabricate generators, motors, loudspeakers, microphones, computer hard discs, sensors and countless other products for uses in automotives, telecommunication, data processing, all kinds of electronics, aerospace and medical imaging, etc.

One of the most important parameters of a permanent magnetic material is its maximum energy product, $(BH)_{max}$, which characterizes the strength of the permanent magnet. The past century has witnessed significant development in permanent magnetic materials, particularly in the progress of maximum energy product. During the past century, the maximum energy product has been improved exponentially, doubling every 12 years. Although further improvement of maximum energy product is expected, the task of keeping this trend of growth is not easy since it is not simple to find a single-phase permanent magnet with high maximum energy product. In 1991, Kneller and Hawig [1] proposed the so called exchange-coupled nanocomposite magnets or exchange-spring magnets consisting of exchange-coupled hard and soft magnetic phases as an alternative approach to achieve high maximum energy product. The idea of the exchange-coupled nanocomposite magnets is to combine high saturation

magnetization of soft phase and large coercivity of hard phase so the maximum energy product of the nanocomposite material is expected to be higher than the single-phase constituent hard or soft magnetic materials.

Since Kneller and Hawig's seminal work, extensive research has been carried out in exchange-coupled nanocomposite magnets. Limited success has been achieved in obtaining high maximum energy product until 2002, Zeng *et al*. [2] reported that the maximum energy product of 20.1 MGOe was achieved in exchange-coupled isotropic FePt/$Fe_3$Pt nanocomposite, which is 50% higher than the theoretical value from a single-phase isotropic FePt. This shows a great promise for attaining potential high maximum energy product in exchange-coupled nanocomposite magnets.

As progresses made in the experimental aspect in the exchange-coupled nanocomposite magnets, although challenges still remain in synthesis and processing of the nanocomposite, theoretical understanding also advanced. For example, shortly after Kneller and Hawig's work, Skomski and Coey [3, 4] predicted, using micromagnetic simulations, that a giant energy product of 120 MGOe might be achieved by exploiting the exchange-spring mechanism in oriented nanostructured magnets. According to their simulations, the grain size of soft phase material should not be larger than twice the domain-wall thickness of hard phase material for effective exchange coupling. However, the advances in theoretical understanding are far behind the advances in experiments. There are still many unsolved fundamental issues in the understanding of hard/soft exchange-coupled nanocomposite magnets need to be addressed. For example, the dependence of the exchange coupling between soft and hard phases on the effects of the

soft phase properties and interface conditions are not clear. This incomplete theoretical understanding of these atomic-scale effects has partly hindered the development of the exchange-coupled nanocomposite magnets.

To study these atomic-scale effects we must solve the quantum mechanical many-body problem which presents a great challenge that can only be partly mastered using approximations. Since its establishment in the 1960's, Density Functional Theory (DFT) with local (spin) density functional approximation (L(S)DA) [5, 6] has become one of the most important approximations of this kind and has demonstrated its power in the study of the ground state properties of real materials. In this dissertation, first-principles study based on density functional theory is performed to investigate the soft phase effects and interface effects on the inter-phase exchange coupling between soft and hard phases. In a prototype model system, we use $SmCo_5$ as hard phase material and Co or FeCo alloys as soft phase material. On the soft phase effects, we have investigated the structural, electronic and magnetic properties of FeCo alloys. It is found that the alloys are only stable in bcc structures and prefer chemically non-cubic geometries in a wide composition range. Due to this non-cubic preference, appreciable uniaxial magnetic anisotropy energies have been produced, which consequently facilitates the inter-phase magnetic interaction and enhances the overall magnetization in exchange-coupled nanocomposite systems. On the interface effects, we have constructed a $SmCo_5$/Co multilayer model system with optimized atomic structure. The non-collinear magnetic structures were calculated to explore the exchange coupling dependence on the variation of the atomic composition across the interface. It is found

that the inter-phase exchange coupling is strongly dependent on the interfacial conditions between the hard and soft phases.

The remainder of this dissertation is organized as follows. Chapter 2 is devoted to a brief introduction to magnetism and magnetic materials which are the major topic in this study. In Chapter 3, I will describe the methodology we used in the study. The density functional theory, on which our calculations are based, necessary approximations and the methods we used are provided in this chapter. Then I focus on the enhancements of magnetic properties of soft phase material in Chapter 4. The results of the structural and magnetic properties of FeCo alloys are presented. In Chapter 5, the interface effects are discussed. We show in detail of the dependence of inter-phase exchange coupling between hard and soft phases on the interfacial conditions. In chapter 6, we explored the possibility of FeCo nanowires as potential permanent magnets with high maximum energy product or as soft phase component in an anisotropic assembled nanocomposite system. We presented our study of the electronic structure and magnetic properties of FeCo nanowires. Finally, we will summarize the conclusions of this work with potential future work for deeper understanding of the exchange coupling in Chapter 7.

# CHAPTER 2

# MAGNETISM AND MAGNETIC MATERIALS

Magnetism and magnetic materials have been known to mankind since ancient times. From magnetite ($Fe_3O_4$), the first magnetic material ever known to mankind, to elementary magnetic metals Fe, Co and Ni, to more complex magnetic compounds and alloys, magnetic materials have been widely used in our daily life and in industry for a long time. Nowadays they are still in the forefront of materials research since many important technologies depend on advances in magnetic materials and their manipulations. In this chapter, I will present a short introduction to magnetism and magnetic materials, including the classification of magnetism and magnetic materials, certain important concepts needed in the following chapters and properties of ferromagnetic materials. In addition, I will also explain why we are interested in $SmCo_5$ as hard phase material and FeCo alloys as soft phase materials in our study. Most of the introduction is based on references [7-10].

## 2.1 Classification of Magnetism and Magnetic Materials

Macroscopically, magnetism is a phenomenon by which materials assert an attractive or repulsive force on other materials. Microscopically, magnetism in materials originates from the electrons' spin motion and their orbital motion around the nucleus.

These motions produce the spin magnetic moment and the orbital magnetic moment of an electron, respectively. The total magnetic moment of an atom is the resultant magnetic moments from these two contributions together with a small contribution from the nucleus, taking into account the magnetic moments cancellations due to the electrons being grouped in pairs.

Magnetic moments of atoms in materials couple to each other, parallel, antiparallel, or not at all. The individual atomic magnetic moments may be randomly oriented if they do not interact with each other. This provides us a way of classifying materials. The five types of magnetism based on this criterion are: diamagnetism, paramagnetism, ferromagnetism, antiferromagnetism and ferrimagnetism.

Diamagnetism is a very weak form of magnetism. All materials are diamagnetic to some extent although this behavior may be superseded by a more dominant effect, such as ferromagnetism. In diamagnetic substances, the atoms have no net magnetic moments when there is no external applied field. When an external magnetic field is applied, a magnetization in the opposite direction to that of the applied field will be produced. When the applied field increases, the magnetization also increases in the opposite direction. In terms of the concept of susceptibility, which is defined as the variation in magnetization M of a material with applied magnetic field H, diamagnetic materials have small and negative susceptibilities. The value of susceptibility is independent of temperature. Examples of diamagnetic materials are Cu, He, Au.

In paramagnetic materials, the atoms have net magnetic moments. However, these magnetic moments are only weakly coupled to each other, and so thermal energy

causes random alignment of the magnetic moments. Therefore, overall the paramagnetic material has no net magnetic moments without an applied magnetic field. When an external magnetic field is applied, the magnetic moments start to align to the same direction of the applied magnetic field, but only a small fraction is aligned for all practical field strengths because thermal energy is large relative to the magnetic energy. Thus the susceptibilities of paramagnetic materials are small and positive. In addition, the susceptibility is temperature dependent because as the temperature increases, the thermal agitation will also increase and so the atomic magnetic moments will become harder to align to the direction of the applied magnetic field. Some examples of paramagnetic materials are Na, Al and Mn.

Ferromagnetism is one of the strongest forms of magnetism. In ferromagnetic materials, the atoms are arranged in a lattice and the atomic magnetic moments coupled to align parallel to each other even in the absence of an applied magnetic field. In quantum mechanics, the Heisenberg model of ferromagnetism describes the parallel alignment of magnetic moments in terms of an exchange interaction between neighboring moments. This parallel alignment of the atomic magnetic moments in ferromagnetic materials results in a strong permanent internal magnetic field within the material. The susceptibilities of ferromagnetic materials are positive and large, as high as $10^6$. Common ferromagnetic materials include Fe, Co and Ni.

Antiferromagnetic materials are very similar to ferromagnetic materials but the exchange interaction between neighboring atoms results in antiparallel alignment of the atomic magnetic moments. The magnetic moments of opposing directions cancel each

other leading to zero net magnetization of the materials and the material appears to behave in the same way as a paramagnetic material. They also have small and positive susceptibilities. The paramagnetic and antiferromagnetic substances can be distinguished from on another by magnetic measurement only if the measurements extend over a range of temperature. Examples of antiferromagnetic materials are Cr, MnO and FeO.

Ferrimagnetism is another type of magnetic ordering and is only observed in compounds. In ferrimagnetic materials, the exchange interactions also cause the magnetic moments of adjacent atoms in antiparallel alignment like those in antiferromagnetic materials. However, these antiparallel aligned magnetic moments do not cancel out so there are net magnetic moments in the materials. Therefore, ferrimagnetic materials behave very much like ferromagnetic materials, except that they usually have much lower susceptibility. The ferrimagnetic and ferromagnetic substances can be distinguished from on another by magnetic measurement only if the measurements extend over a range of temperature. A famous example of ferrimagnetic materials is magnetite $Fe_3O_4$. MnZn and NiZn are also ferrimagnetic materials.

Because of the ordering in magnetic moments of atoms, ferromagnetic materials, antiferromagnetic materials and ferrimagnetic materials are called magnetically ordered. Both diamagnetic and paramagnetic materials are considered to be nonmagnetic because they have no ordering in magnetic moments and only exhibit magnetization in the presence of an external magnetic field.

The orderings of magnetic moments and M-H relations for these five types of materials are illustrated in Figure 2.1.

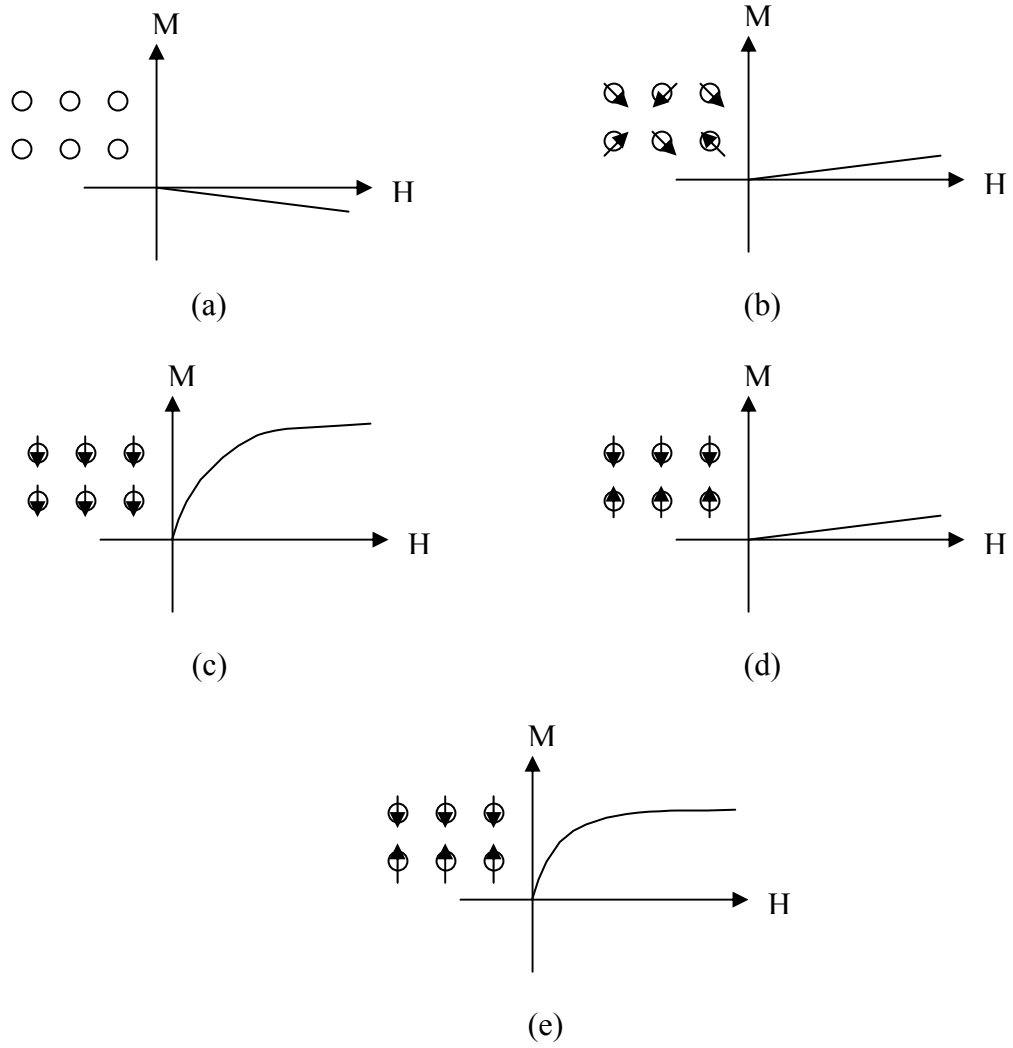


Figure 2.1 Ordering of magnetic moments of atoms and M-H relation in (a) Diamagnetism; (b) Paramagnetism; (c) Ferromagnetism; (d) Antiferromagnetism; and (e) Ferrimagnetism.

## 2.2 Some Properties and Concepts of Ferromagnetic Materials

Among all kinds of magnetic materials, ferromagnetic materials are the most widely used. Some related concepts and their properties are introduced in the following.

### 2.2.1 Domain, Hysteresis, Saturation Magnetization, and Coercivity

As we discussed above, the exchange interactions align adjacent atomic magnetic moments parallel in ferromagnetic materials, causing an internal magnetic field even in the absence of an applied field. This brings up another question from our practical experience: if ferromagnetic materials, for example iron, have internal magnetic fields, how can we explain that usually we obtain a piece of iron in the demagnetized condition? This is because a ferromagnetic material in the demagnetized is divided into domains, which are small regions in ferromagnetic materials within which all the atomic magnetic moments are aligned parallel to each other. The boundaries between neighboring domains are called domain walls, across which the direction of magnetization changes gradually. Figure 2.2 shows a simplified picture of magnetic domains in an iron crystal with the spatial variation of the atomic moments within the domain wall shown in an expanded view. When a ferromagnetic material is in its demagnetized state, the magnetizations in different domains have such different orientations that the ferromagnetic material as a whole has no net magnetization. Although a single domain would minimize the exchange contribution to the total energy, there are a number of other contributions to the total magnetic energy. These include magnetostatic energy, magnetocrystalline energy and magnetostrictive energy. The formation of domains allows a ferromagnetic material to minimize its total magnetic energy, of which the exchange energy is just one component.

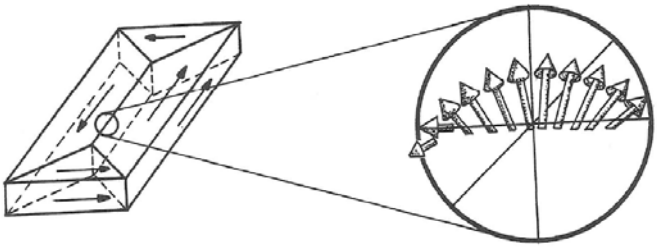

Figure 2.2 Simplified picture of magnetic domains in an iron crystal. The spatial variation of the atomic moments within the domain wall is shown in an expanded view. Copied from Ref. [9].

Another phenomenon about ferromagnetic materials is hysteresis, which describes the magnetic behavior of a ferromagnetic material when applied with a magnetic field, as shown in Figure 2.3. It is evident that ferromagnetic materials have nonlinear magnetization curves and show hysteresis and the magnetization does not return to zero after the applied filed returns to zero.

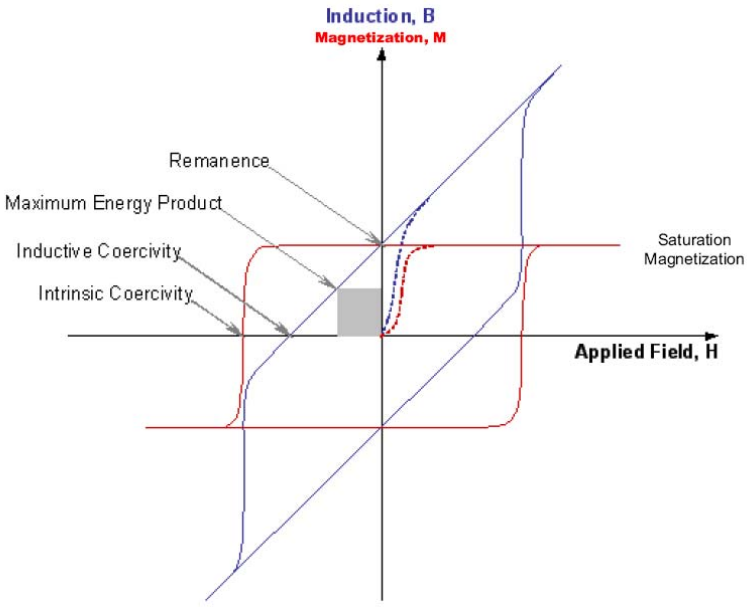


Figure 2.3 A typical hysteresis loop for a ferromagnetic material. Adapted from Ref. [11].

In the initial demagnetized state, the domains are arranged randomly so there is no net magnetization as we just discussed. When an external magnetic field is applied, the domain whose magnetization is closest to the direction of the applied field starts to grow through domain wall motion, at the expense of shrinking of other domains that are unfavorably oriented. Usually the moving domain walls will encounter imperfections such as defects or dislocations in the ferromagnetic crystal. When a domain boundary intersects the imperfection, the magnetostatic energy associated with the imperfection will be eliminated. The intersection of the domain boundary with the imperfection is a local energy minimum. As a result the domain boundary will tend to stay pinned at the imperfection, and energy is required to move it past the imperfection. The external applied magnetic field provides this energy. Eventually, all domain walls in the ferromagnetic material are eliminated with sufficient high applied field. This leads to a single domain, with its magnetization pointing to the easy axis oriented most closely to the external magnetic field. Further increase of the applied field will rotates the magnetization of the single domain from the easy axis to the direction of the applied field. At this stage the magnetization can be increased no more with increasing applied field and the saturation is reached. This magnetization is called saturation magnetization, $M_s$. It measures the maximum amount of field that a ferromagnetic material can generate. Based on what we have discussed, it will depend on the values of the magnetic moments of the atoms that make up the material and how densely these atoms are packed together.

When the applied field is reduced, the magnetization first rotates back to the easy axis. Next reverse magnetic domains grow to allow the material to be partially demagnetized, initiated by the demagnetizing field inside the ferromagnetic material. However, the domain walls are unable to fully reverse their motion back to their original positions. This is because the demagnetizing field, not the applied magnetic field, drives the demagnetization process, and the demagnetizing field is not strong enough to overcome the energy barriers encountered when the domain walls intersect the imperfections. As a result, a hysteresis effect is produced and some magnetization, called remnant magnetization $M_r$, remains in the ferromagnetic material even when the field is completely removed. The coercivity $H_c$ is defined as the reverse field applied to reduce the magnetization to zero. It is closely related to the ferromagnetic material's magnetic anisotropy, as we will introduce in the section 2.2.3.

### 2.2.2 Curie Temperature: $T_c$

Curie temperature is the temperature above which a ferromagnetic material loses magnetization. Below its Curie temperature, a ferromagnetic material is ordered in atomic scale. With rising temperature, thermal energy increases, counteracting the exchange interactions between the atoms and resulting in a decrease in the saturation magnetization of the materials. When the temperature reaches the Curie temperature, the increasing thermal energy eventually overcomes the exchange interactions and randomizes the directions of the aligned magnetic moments due to exchange interaction, resulting in zero saturation magnetization. So above the Curie temperature, the

ferromagnetic material becomes paramagnetic with randomly oriented atomic magnetic moments.

### 2.2.3 Magnetic Anisotropy

Magnetic anisotropy simply means that the magnetic properties of ferromagnetic materials depend on the direction in which they are measured. The magnetization tends to align along certain preferred directions, which are called easy axes since it is easier to magnetize a demagnetized ferromagnetic material to saturation if the external magnetic field is applied along a preferred direction. The energy difference between magnetizations along the easy and hard axes is called magnetic anisotropy energy.

There are several kinds of magnetic anisotropy, including magnetocrystalline anisotropy, shape anisotropy, stress anisotropy, exchange anisotropy and anisotropy induced by material processing. Only magnetocrystalline anisotropy is intrinsic to the ferromagnetic material and all the others are extrinsic. The magnitude and type of magnetic anisotropy affect magnetization and hysteresis loop in ferromagnetic properties. In this section, I will only introduce magnetocrystalline anisotropy and shape anisotropy since these are the properties we will investigate in our study.

Magnetocrystalline anisotropy is the tendency of the magnetization to align itself along the easy axis. The origin of magnetocrystalline anisotropy mainly comes from the spin-orbit coupling, which is the interaction between the spin and the orbital motion of an electron. When an external applied field tries to reorient the spin of an

electron, the orbit of that electron also tends to be reoriented because of this spin-orbital coupling. However, the orbit is strongly coupled to the crystal lattice and therefore resists the attempt to rotate the spin axis. The energy required to rotate the spin system of a domain away from the easy axis to the hard axis, which is defined as magnetocrystalline anisotropy energy, is actually just the energy required to overcome the spin-orbit coupling.

Shape anisotropy is another kind of magnetic anisotropy which origins in the non-spherical shape of a ferromagnetic sample. If it is spherical in shape, the same applied magnetic field will magnetize it to the same extent in every direction. However if it is not spherical, it will be easier to magnetize it along a long axis than along a short axis because the demagnetizing field along a short axis is stronger than along a long axis. The applied field along a short axis then has to be stronger to produce the same magnitude of magnetization inside the sample.

Figure 2.4 (a) shows schematic magnetization curves for a ferromagnetic material with the external field applied along the easy and hard axes. In both cases the same saturation magnetization is achieved, but a much larger applied field is required to reach saturation along the hard axis than along the easy axis. Figure 2.4 (b) demonstrates the easy, medium and hard directions of magnetization in a unit cell of *bcc* iron. In this case the easy axis is along one of the (100) crystal directions. A large magnetic field is required to saturate the magnetization along the (111) direction, the hard axis of magnetization. In *fcc* Ni the easy and hard axes of magnetization are the (111) and (110) directions, respectively. For *hcp* Co the easy axis of magnetization is

along the *c* (0001) direction while the hard axis lies in the basal plane of the conventional *hcp* unit cell.

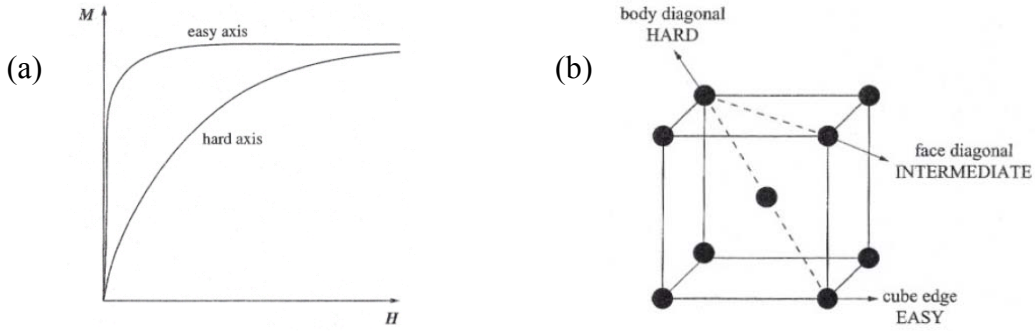


Figure 2.4 (a) Schematic magnetization curves for a ferromagnetic material with the applied field oriented along the hard and easy directions; (b) Easy, medium and hard directions of magnetization in a unit cell of bcc iron. Copied from Ref. [8].

### 2.2.4 Maximum Energy Product $(BH)_{max}$

The maximum energy product $(BH)_{max}$ is one of a few measures of quality of a ferromagnetic material, representing the energy required to demagnetize the material. It is defined as the maximum value of the product of *B* and *H*, corresponding to the area of the largest rectangular that can be constructed in the second quadrant of the B-H loop. The value of the maximum energy product increases with increasing both coercivity and saturation magnetization. However, for materials with sufficiently high coercivity, there is a theoretical upper limit of $\mu_0 M_s^2 / 4$, which is obtained from an ideal rectangular B-H loop. Figure 2.5 [12] shows the growth history of maximum energy product of permanent magnets in the $20^{th}$ century.

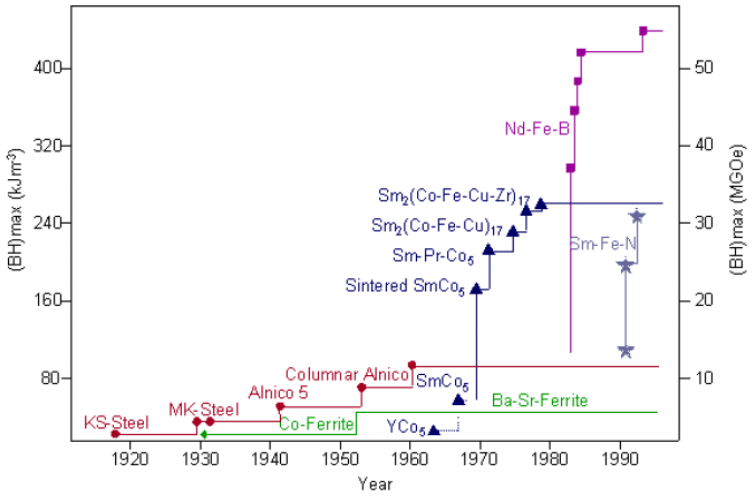


Figure 2.5. The development of permanent magnets in the 20th century. $(BH)_{max}$ has improved exponentially, doubling every 12 years. Copied from Ref. [12].

## 2.3 Hard and Soft Magnetic Materials

In terms of their magnetic properties and uses, ferromagnetic materials can be classified into soft magnetic materials and hard or permanent magnetic materials.

Soft magnetic materials can be easily magnetized and demagnetized by low magnetic field. Expressed in the hysteresis loop, as shown in Figure 2.6 (a), they have high saturation magnetization but low coercive field. When the applied external magnetic field is removed, soft magnetic materials will return to a state of low residual magnetization. Soft magnetic materials are used in electromagnets and transformer cores, where they must be able to reverse their direction of magnetization rapidly.

Hard magnetic materials are very hard to be demagnetized. Expressed in the hysteresis loop, they have large coercivity but low saturation magnetization, as illustrated in Figure 2.6 (b). After the applied external magnetic field is removed, hard

magnetic materials can still retain very high magnetization, and are hard to demagnetize them. Hard magnetic materials find very wide applications in industry and in our everyday life. They are used almost everywhere: in computer hard drives, in ipods, in MRI machines, in motors, in generators, and in magnetic levitation trains.

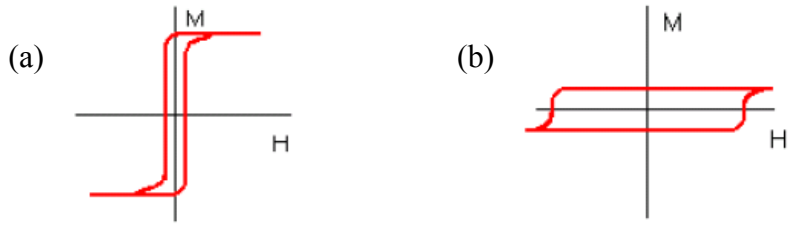


Figure 2.6 Hysteresis loops for (a) soft magnetic materials; and (b) hard magnetic materials.

## 2.4 Exchange-Coupled Nanocomposite Magnets

We have seen from Figure 2.5 that the maximum energy product of permanent magnets has improved exponentially, doubling every 12 years, during the last century. A natural question is: can we keep this trend of the growth of maximum energy product to make more powerful permanent magnets? Researchers in the field of permanent magnets have been competing for new record of the value of maximum energy product. However, it seems that it is not easy to find single-phase permanent magnets with higher maximum energy product. Thus, exchange-coupled nanocomposite magnets were proposed as a possible approach to enhance the maximum energy product. In these exchange-coupled nanocomposite magnets, the soft phase material provides the high magnetization and the hard phase material provides the high coercivity and stabilizes the soft phase against demagnetization via exchange coupling between the two phases,

as schematically shown in Figure 2.7. If the soft phase and hard phase are magnetically exchange coupled with each other, the nanocomposite material is expected to behave like a single-phase permanent magnet with both high coercivity and high saturation magnetization and thus increased maximum energy product. The strength of the exchange coupling between the hard and soft phases is affected not only by the soft and hard phase materials, but also by their dimensions and the interfacial condition between them.

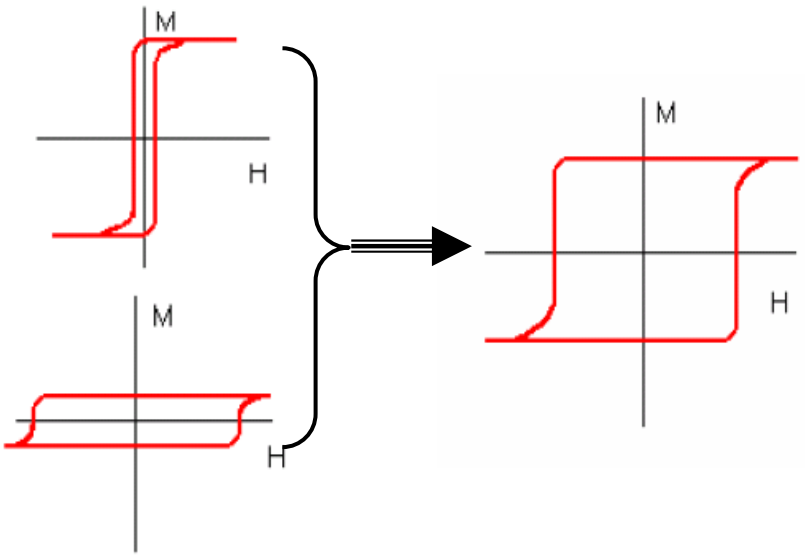


Figure 2.7 Illustration of the idea of nanocomposite magnet, which combines the high saturation magnetization from the soft phase magnet and large coercivity from the hard phase magnet.

## 2.5 Why FeCo Alloys and $SmCo_5$?

In searching for specific hard and soft magnetic materials as constituents of the nanocomposite magnet for our study, we have three considerations.

Firstly, as discussed in the last section, the potential hard magnetic material should have high coercivity, which usually related to a large magnetic anisotropy. In the meantime, the potential soft magnetic material should have high saturation magnetization, as well as appreciable magnetic anisotropy. As reported in previous research work [13-16], magnetic anisotropy in the soft phase material is also an important factor in affecting the exchange coupling between the hard and soft phases.

Secondly, both the hard and soft magnetic materials need to have high Curie temperatures. As a result, the nanocomposite magnet will potentially have high Curie temperature so it can retain its magnetic strength and resist demagnetization in the temperature range of application. Nowadays, many applications require the working temperature of permanent magnetic higher than 400 ℃.

The last consideration is the lattice match between the soft and hard magnetic materials. In general, lattice mismatch at the interface will induce defects during growth of materials and thus affect the quality and characteristics of the grown materials. Lattice match is also important for our theoretical study since we may need to use much larger unit cell in our model calculations if the lattice constants mismatch is big.

Having these three considerations in mind, and looking at the magnetic properties of the commonly used ferromagnetic materials as compile in Table 2.1 [7, 9, 10], we come up with the first model with $SmCo_5$ as hard phase material, and hcp Co as soft phase material. $SmCo_5$ has highest anisotropy and high Curie temperature, whereas Co has high saturation magnetization and highest Curie temperature. The lattice mismatch between them along $(10\bar{1}0)$ direction is only 0.2% from our calculations as

we will report later. The other possible model is to use $Sm_2Co_{17}$ as hard phase material and bcc Fe as soft phase material since they also satisfy our three considerations. We have done some research work on this model but they will not be reported here since it is not in the scope of this dissertation. It is worth noting that although $Nd_2Fe_{14}B$ has relatively high saturation magnetization and high coercivity and potentially highest maximum energy product, it is not chosen in our study because it has low Curie temperature.

Table 2.1 Magnetic properties of some commonly used ferromagnetic materials. The data are compiled from References [7, 9, 10].

| Material | Saturation Magnetization (T) | Anisotropy Energy ($J/m^3$) | Curie Temperature (℃) | $(BH)_{max}$ ($KJ/m^3$) (theoretical) |
|---|---|---|---|---|
| $SmCo_5$ | 1.07 | $1.5\times10^7$ | 725 | 240 |
| $Sm_2Co_{17}$ | 1.28 | $3.2\times10^6$ | 926 | 326 |
| $Nd_2Fe_{14}B$ | 1.61 | $4.3\times10^6$ | 312 | 510 |
| FePt | 1.43 | $6.7\times10^6$ | 477 | 105 |
| Fe | 2.14 | $4.8\times10^4$ | 770 | -- |
| Co | 1.78 | $4.1\times10^5$ | 1130 | -- |
| Ni | 0.62 | $-4.5\times10^3$ | 358 | -- |

# CHAPTER 3

# METHODOLOGY

First-principles calculations refer to quantum mechanical calculations without any external parameters except the atomic numbers of the atoms involved in the calculations. In this chapter, the theoretical background of density functional theory, necessary approximations needed for practical calculations, and various methods implemented based on density functional theory are described.

## 3.1 The Born-Oppenheimer Approximation

When dealing with a solid consisting of nuclei and electrons, we are dealing with a quantum, many-body problem. In principle this problem is covered by the time-dependent Schrödinger equation

$$\hat{H}\Psi(R,r,t) = i\hbar\frac{\partial\Psi(R,r,t)}{\partial t}, \tag{3.1}$$

where $\hat{H}$ is the Hamiltonian operator corresponding to the total energy of the system, $\Psi(R,r,t)$ is the wavefunction, a function of all the self-variants of the system, including the nuclear positions $R$, electron positions and spins $r$ and time $t$.

Suppose there are no external fields, the Hamiltonian of a system consisting of $M$ nuclei (each with charge $Z_\alpha$ and mass $m_\alpha$ ) and $N$ electrons, in atomic units ( $m_e = 1, e = 1, \hbar = 1$ ), is given by

$$\hat{\mathrm{H}} = \hat{\mathrm{T}} + \hat{\mathrm{V}}, \tag{3.2}$$

where

$$\hat{T} = -\frac{1}{2m_\alpha}\sum_{\alpha}^{M}\nabla_\alpha^2 - \frac{1}{2}\sum_{i}^{N}\nabla_i^2 \tag{3.3}$$

representing the kinetic energies of the nuclei and electrons respectively, and

$$\hat{V} = \sum_{\alpha}^{M}\sum_{\beta>\alpha}^{M}\frac{Z_\alpha Z_\beta}{\left|R_\alpha - R_\beta\right|} - \sum_{\alpha}^{M}\sum_{i}^{N}\frac{Z_\alpha}{\left|R_\alpha - r_i\right|} + \sum_{i}^{N}\sum_{j>i}^{N}\frac{1}{\left|r_i - r_j\right|} \tag{3.4}$$

describing the Coulomb interactions between nuclei and other nuclei, between electrons and nuclei, and between electrons and other electrons, respectively.

Since the Hamiltonian above is independent of time, using the technique of separation of variables the solution of the Schrödinger equation can be written as

$$\Psi(R, r, t) = \Psi(R, r) f(t). \tag{3.5}$$

By substituting this equation back to Equation (3.1), the time-dependent Schrödinger Equation is reduced to a time-independent Schrödinger Equation

$$\hat{H}\Psi = E\Psi \tag{3.6}$$

and

$$\Psi(R, r, t) = \Psi(R, r)\exp(-iEt/\hbar). \tag{3.7}$$

This equation shows that if the potential is independent of time and the system is in a state of energy E, all that is required to construct the time-dependent wavefunction from the time-independent wavefunction is multiplication by $\exp(-iEt/\hbar)$, which is simply a modulation of its phase.

While theoretically the Schrödinger equation describes the many-body problem, it is out of the question to solve this equation exactly in practice. It is too complicated to be solved for all except the simplest systems. To overcome this difficulty, we will need to make approximations to find acceptable approximate eigenstates. The first level of approximation is the Born-Oppenheimer Approximation [17, 18].

In the Born-Oppenheimer Approximation, the electrons and the ions in a real system are treated separately because of the large mass difference between them. The forces on both electrons and nuclei due to their electric charge are of the same order of magnitude, and so the changes which occur in their momenta as a result of these forces must also be the same. One might therefore assume that the actual momenta of the electrons and nuclei were of similar magnitude. In this case, since the nuclei are so much more massive than the electrons, they must accordingly have much smaller velocities and move much slower. Thus it is plausible that on the typical time scale of the nuclear motion, the electrons will very rapidly relax to the instantaneous ground state configuration. So that in solving the time independent Schrödinger equation resulting from the Hamiltonian in equation, we can assume that the nuclei are stationary at fixed positions and the electrons are in instantaneous equilibrium with them. After applying this approximation, we are left with a collection of electrons moving in an

external potential produced by the nuclei. So instead of solving the original Schrödinger equation (3.6), we solve for the electronic ground state first and then calculate the energy of the system in that configuration and solve for the nuclear motion. In mathematical terms, the ionic wavefunction $\xi(\mathrm{R})$ is independent of the electronic wavefunction and the total wavefunction of the system can be approximately written as the product of ionic and electronic terms

$$\Psi(\mathrm{R},\mathrm{r}) = \xi(\mathrm{R})\psi_{\mathrm{R}}(\mathrm{r}), \tag{3.8}$$

where the notation of the electronic wavefunction $\psi_{\mathrm{R}}(\mathrm{r})$ implies that it only depends parametrically on the ionic positions R.

As a consequence of the Born-Oppenheimer approximation, the first term in equation (3.3), i.e. the kinetic energy of nuclei, is zero. The first term in equation (3.4), i.e. the potential energies due to the nuclear-nuclear interactions, reduces to a constant. Therefore, we are left with three terms. If we write the external Coulomb potential produced by the nuclei as $V_{ext}(r)$

$$V_{ext}(r_i) = -\sum_{\alpha} \frac{Z_\alpha}{|R_\alpha - r_i|}, \tag{3.9}$$

and define

$$\hat{V}_{ext}(r) = \sum_i V_{ext}(r_i), \tag{3.10}$$

and

$$\hat{F} = -\sum_{i=1}^{N}(-\frac{1}{2}\nabla_i^2) + \sum_i^N \sum_{j>i}^N \frac{1}{|r_i - r_j|}, \tag{3.11}$$

then the electronic Hamiltonian after applying the Born-Oppenheimer approximation can be written as

$$\hat{H} = \hat{V}_{ext} + \hat{F} \,. \tag{3.12}$$

It is worth noting that $\hat{F}$ is universal for all N-electron systems, independent of the particular kind of many-electron system. The Hamiltonian and hence the ground state wave function $|\psi_0\rangle$ will be completely determined by $N$ and $\hat{V}_{ext}$. Therefore, the ground state wave function $|\psi_0\rangle$ and electronic charge density $\rho_0(r)$ are both functionals of the number of electrons $N$ and the external potential $V_{ext}(r)$. The ground state electronic charge density in terms of $|\psi_0\rangle$ is

$$\rho_0(r_1) = N \int |\psi_0|^2 dr_2 \cdots dr_N \,. \tag{3.13}$$

## 3.2 Density Functional Theory

Separate treatment of electronic and ionic movements in the Born-Oppenheimer approximation simplifies the original many-body problem and allows us to treat the ions in a classical formalism. However, because of the mutual interactions between electrons, the electronic problem is still a far too complicated many-body quantum problem to be solved exactly in practical computations. Owing to this difficulty, further developments are required to convert a many-body problem into many one-body problems for real materials. Density Functional Theory provides a framework for these developments.

Density Functional Theory, based on two theorems first proved by Hohenberg and Kohn [5] in the 1960's, makes it possible to describe the ground state properties of

a real system in terms of its ground state charge density instead of the far more complicated wavefunction. This theory allows us to find the ground state properties of a system in terms of the ground state charge density without explicit recourse to many-particle wavefunctions. Since the electronic charge density depends only on four variables (three Cartesian variables and electron spin), the original 4M (where M is the number of electrons) variables problem involving the complicated wavefunctions is reduced to a much simpler problem in which only four variables are needed to define the charge density at a point. Thus the computational efforts will be drastically reduced and the problem will be feasible to be solved computationally.

### 3.2.1 The Hohenberg-Kohn Theorems

The two Hohenberg-Kohn theorems state that:

**Theorem I**: For any system of interacting particles in an external potential $V_{ext}(r)$, the potential $V_{ext}(r)$ is determined uniquely, except for a constant, by the ground state electronic charge density $\rho_0(r)$.

**Theorem II**: A universal functional for the energy in terms of the density $\rho(r)$ can be defined, valid for any external potential $V_{ext}(r)$. For any particular $V_{ext}(r)$, the exact ground state energy of the system is the global minimum value of this functional, and the density $\rho(r)$ that minimizes the functional is the exact ground state density $\rho_0(r)$.

A schematic representation of these two theorems is shown in Figure 3.1.

The proofs of the Hohenberg-Kohn theorems are disarmingly simple. To prove Theorem I, we use the method of *reductio ad absurdum*: suppose that there was a second different external potential $V_{ext}'(r)$ which differs from $V_{ext}(r)$ by more than a constant. These two external potentials give rise to the same ground state density $\rho_0(r)$ but lead to two different Hamiltonians, $\hat{H}$ and $\hat{H}'$, which have two different non-degenerate ground state wavefunctions, $\psi$ and $\psi'$. Since $\psi'$ is not the ground state wavefunction of $\hat{H}$, it follows that

$$\begin{aligned} E_0 &= \langle \psi | \hat{H} | \psi \rangle < \langle \psi' | \hat{H} | \psi' \rangle = \langle \psi' | \hat{H}' | \psi' \rangle + \langle \psi' | \hat{H} - \hat{H}' | \psi' \rangle \\ &= E_0' + \int d^3 r \left[ V_{ext}(r) - V_{ext}'(r) \right] \rho_0(r), \end{aligned} \tag{3.14}$$

where $E_0$ and $E_0'$ are the ground state energies for $\hat{H}$ and $\hat{H}'$, respectively. Similarly, if we consider $E_0'$ in exactly the same way, we have an equation

$$\begin{aligned} E_0' &= \langle \psi' | \hat{H}' | \psi' \rangle < \langle \psi | \hat{H}' | \psi \rangle = \langle \psi | \hat{H} | \psi \rangle + \langle \psi | \hat{H}' - \hat{H} | \psi \rangle \\ &= E_0 - \int d^3 r \left[ V_{ext}(r) - V_{ext}'(r) \right] \rho_0(r). \end{aligned} \tag{3.15}$$

Adding these two equations, we would obtain the contradictory inequality

$$E_0 + E_0' < E_0 + E_0', \tag{3.16}$$

which is absurd. This shows that there cannot be two different external potentials differing by more than a constant which give the same ground state charge density.

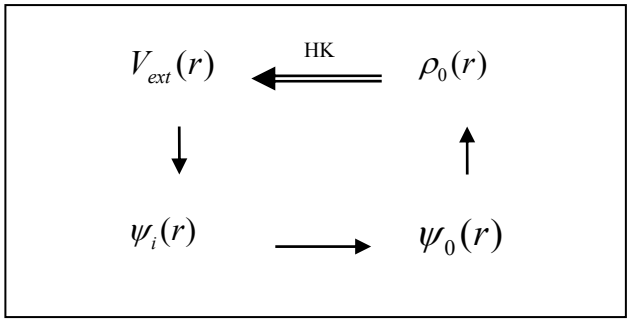


Figure 3.1 Schematic representation of Hohenberg-Kohn theorems. The single arrows denote the usual solution of the Schrödinger equation where the potential $V_{ext}(r)$ determines all states of the system $\psi_i(r)$, including the ground state $\psi_0(r)$ and ground density $\rho_0(r)$. The double arrow labeled "HK" denotes the Hohenberg-Kohn theorems, which completes the cycle. Adapted from Ref. [19].

The charge density uniquely determines $N$ and the external potential $V_{ext}(r)$ within a constant. Because the external potential and number of electrons $N$ determine all the ground state properties of the system since the Hamiltonian and ground state wave function are determined by them. Hence all properties of the ground state, for example the kinetic energy $T[\rho]$, the potential energy $V[\rho]$ and the total energy $E[\rho]$, are uniquely determined by the charge density $\rho(r)$. Then we have, for the total energy

$$E[\rho] = T[\rho] + V_{ne}[\rho] + V_{ee}[\rho] = \int \rho(r)V(r)dr + F[\rho], \tag{3.17}$$

where

$$F[\rho] = T[\rho] + V_{ee}[\rho] \tag{3.18}$$

is an introduced functional as defined above.

The second Theorem can be easily proved by using the variational principle: by the first Theorem, a given electronic charge density $\rho(r)$ determines its own external potential $V_{ext}(r)$ and ground state wavefunction $\psi_0[\rho]$. If this wavefunction is used as a trial function for the Hamiltonian having external potential $V(r)$, then

$$\begin{aligned}&\langle\psi_0[\rho]|\hat{H}|\psi_0[\rho]\rangle = \langle\psi_0[\rho]|\hat{F}|\psi_0[\rho]\rangle + \langle\psi_0[\rho]|\hat{V}|\psi_0[\rho]\rangle \\ &= F[\rho] + \int \rho(r)V(r)dr = E_V[\rho] \geq E_V[\rho_0] = E_0 = \langle\psi_0[\rho_0]|\hat{H}|\psi_0[\rho_0]\rangle.\end{aligned} \tag{3.19}$$

For non-degenerate ground states, the equality holds only if

$$\psi_0[\rho] = \psi_0[\rho_0], \tag{3.20}$$

and therefore

$$\rho = \rho_0. \tag{3.21}$$

This shows that the ground state density is indeed the density that minimizes the functional.

The inequality follows from Rayleigh–Ritz's variational principle for the wave function, but applied to the electronic density. Assuming differentiability of $E[\rho]$, the variational principle requires that the ground state density satisfy

$$\delta\left\{E[\rho] - \mu\left[\int \rho_0(r)dr - N\right]\right\} = 0, \tag{3.22}$$

which gives the Euler-Lagrange equation of the form

$$\mu = \frac{\delta E[\rho_0]}{\delta\rho_0(r)} = V(r) + \frac{\delta F[\rho_0]}{\delta\rho_0(r)}, \tag{3.23}$$

Where $\mu$ is the Lagrange multiplier corresponding to the chemical potential associated with the constraint

$$\int \rho_0(r)dr = N. \tag{3.24}$$

Equation (3.23) is the basic working equation of density functional theory.

The above proofs assumed the non-degeneracy of the ground states. It has been shown that this condition can be lifted by the so-called "constrained search formulation" proposed by Levy [20-22] and Lieb [23-25] and therefore the density functional formalism can be generalized to deal with both non-degenerate and degenerate ground states.

$F[\rho]$ of equation (3.18) is a universal functional of $\rho(r)$ in a sense that $F[\rho]$ is defined independently of the external potential $V(r)$. If we knew the exact functional $F[\rho]$, the equation (3.22) would be an exact equation for the ground state electron density. Therefore, once we have an explicit form for $F[\rho]$, we can apply this method to any system. However, accurate implementations of the density functional theory are far from easy to achieve because of the unfortunate fact that the functional $F[\rho]$ is hard to come by in explicit form.

### 3.2.2 The Kohn-Sham Method

Density functional theory is the most widely used method today for electronic structure calculations because of the approach proposed by Kohn and Sham in 1965 [6] to replace the original many-body problem by an auxiliary independent-particle problem. This is an ansatz that, in principle, leads to exact calculations of properties of many-body systems using independent-particle methods; in practice, it has made

possible approximate formulations that have proved to be remarkably successful. As a self-consistent method, the Kohn-Sham approach involves independent particles but an interacting density, an appreciation of which clarifies the way the method is used.

The Kohn-Sham ansatz assumes that the exact ground state density $\rho_0(r)$ can be represented by the ground sate density $\rho(r)$ of an auxiliary system of non-interacting particles as illustrated in Figure 3.2. Although there are no rigorous proofs for real systems of interest, it is assumed this equivalent non-interacting system does exist.

The auxiliary Hamiltonian is chosen to have the usual kinetic operator and an effective local potential $V_{eff}(r)$ acting on an electron but have no electron-electron repulsion terms. Using the atomic units, this Hamiltonian is written as

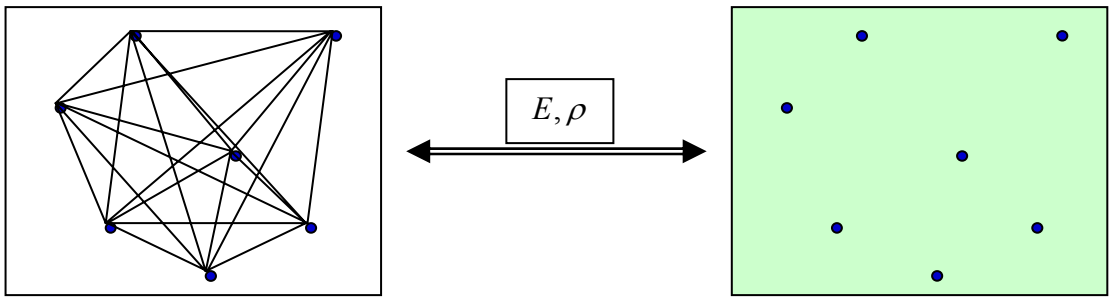


Figure 3.2 A cartoon representing the relationship between the real many body system (left hand side) and the auxiliary non-interacting system of Kohn-Sham method.

$$\hat{H}_s = \sum_i^N \left( \frac{1}{2} \nabla_i^2 \right) + \sum_i^N V_{eff}(r_i). \tag{3.25}$$

There will be an exact determinantal ground state wavefunction for this system,

$$\psi_s = \frac{1}{\sqrt{N!}} \det\left[\varphi_1 \varphi_2 ... \varphi_N\right], \tag{3.26}$$

where the $\varphi_i$ are called KS orbitals corresponding to the $N$ lowest eigenstates of the one-electron Hamiltonian $\hat{h}_s$:

$$\hat{h}_s \varphi_i = \left[-\frac{1}{2}\nabla^2 + V_{eff}(r)\right]\varphi_i = \varepsilon_i \varphi_i. \tag{3.27}$$

The electronic charge density will be given as

$$\rho(r) = \sum_{i=1}^{N} \left|\varphi_i(r)\right|^2 \tag{3.28}$$

and the kinetic term is

$$\begin{aligned} T_s\left[\rho\right] &= \left\langle \psi_s \middle| \sum_{i=1}^{N} \left(-\frac{1}{2}\nabla_i^2\right) \middle| \psi_s \right\rangle \\ &= \sum_{i=1}^{N} \left\langle \varphi_i \middle| -\frac{1}{2}\nabla^2 \middle| \varphi_i \right\rangle. \end{aligned} \tag{3.29}$$

Using this kinetic energy form, the universal functional $F\left[\rho\right]$ in equation (3.18) can be rewritten as

$$\begin{aligned} F\left[\rho\right] &= T\left[\rho\right] + V_{ee}\left[\rho\right] \\ &= T_s\left[\rho\right] + J\left[\rho\right] + \left\{T\left[\rho\right] - T_s\left[\rho\right] + V_{ee}\left[\rho\right] - J\left[\rho\right]\right\} \\ &= T_s\left[\rho\right] + J\left[\rho\right] + E_{xc}\left[\rho\right], \end{aligned} \tag{3.30}$$

where $J\left[\rho\right]$ is the classical electrostatic interaction energy corresponding to a charge distribution $\rho(r)$,

$$J\left[\rho\right] = \frac{1}{2}\int \frac{\rho(r)\rho(r')}{\left|r - r'\right|} dr dr'. \tag{3.31}$$

Equation (3.30) also defines the exchange-correlation energy as a functional of density

$$E_{xc}[\rho] = T[\rho] - T_s[\rho] + V_{ee}[\rho] - J[\rho]. \tag{3.32}$$

From this definition, we can see clearly that the exchange-correlation energy $E_{xc}[\rho]$ includes two parts of contributions: the non-classical electron-electron interaction energy and the difference between the two kinetic energies $T[\rho]$ and $T_s[\rho]$.

Upon substitution of the expression of $F[\rho]$ in equation (3.17), the total energy functional can be rewritten as

$$E[\rho] = T_s[\rho] + J[\rho] + E_{xc}[\rho] + \int \rho(r)V(r)dr \tag{3.33}$$

and the Euler-Lagrange equation now becomes

$$\mu = V_{eff}(r) + \frac{\delta T_s[\rho]}{\delta\rho(r)}, \tag{3.34}$$

where the Kohn-Sham effective potential is defined by

$$\begin{aligned} V_{eff}(r) &= V(r) + \frac{\delta J[\rho]}{\delta\rho(r)} + \frac{\delta E_{xc}[\rho]}{\delta\rho(r)} \\ &= V(r) + \int \frac{\rho(r')}{|r-r'|}dr' + V_{xc}(r), \end{aligned} \tag{3.35}$$

with the exchange-correlation potential

$$V_{xc}(r) = \frac{\delta E_{xc}[\rho]}{\delta\rho(r)}. \tag{3.36}$$

In summary, the KS orbitals satisfy the well-known self-consistent Kohn-Sham equations

$$\left[-\frac{1}{2}\nabla^2 + V_{eff}(r)\right]\varphi_i = \varepsilon_i \varphi_i, \tag{3.37}$$

and the electronic charge density is constructed using the KS orbitals

$$\rho(r) = \sum_{i=1}^{N} |\varphi_i(r)|^2. \tag{3.38}$$

Comparing with the single Euler-Lagrange equation (3.34), we see that, by introducing the N KS orbitals, the Kohn-Sham equations handle $T_s[\rho]$, the dominant part of the true kinetic energy $T[\rho]$, indirectly but exactly. This is a major advance over the Hohenberg-Kohn theorems: the major part of the unknown functional $F[\rho]$ is known exactly; only a residual part $E_{xc}[\rho]$ is unknown now. The relationship between the Hohenberg-Kohn theorems and the Kohn-Sham method is schematically represented in Figure 3.3.

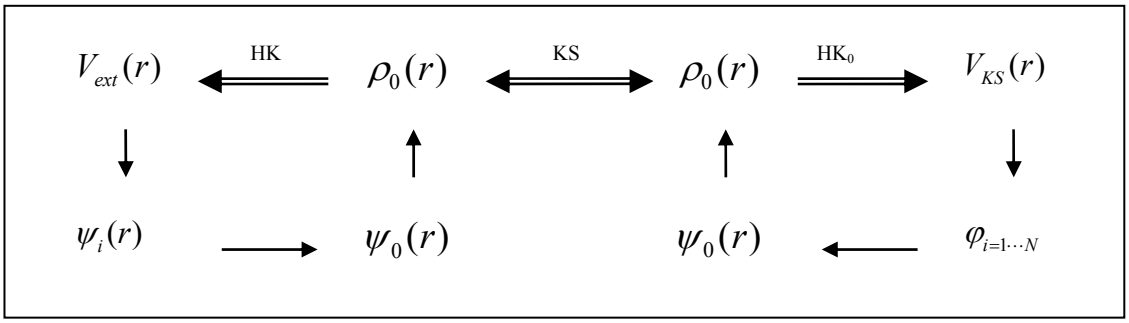


Figure 3.3 Schematic representation of Kohn-Sham method. The notation $HK_0$ denotes the Hohenberg-Kohn theorems applied to the non-interacting problem. The arrow labeled KS provides the connection in both directions between the many-body and single-particle systems. Therefore, in principle, solution of the single-particle Kohn-Sham problem determines all properties of the many-body system. Adapted from Ref. [19].

3.2.3 Spin Density Functional Theory

The density functional theory as it has been discussed up to this point only use the total density $\rho(r)$ as the fundamental variable. However, this is not the widely used density functional theory in practical applications. Much common is the spin density functional theory which works with two fundamental variables, i.e., the up and down spin densities $\rho^{\alpha}(r)$ and $\rho^{\beta}(r)$. They are defined as

$$\rho^{\sigma}(r) = \sum_{i=1}^{N_{\sigma}} \left|\varphi_i^{\sigma}(r)\right|^2 \quad (\sigma = \alpha, \beta), \tag{3.39}$$

with the interpretation that $\rho^{\sigma}(r)d^3r$ is the probability of finding an electron of spin $\sigma$ in $d^3r$ around $r$. These two fundamental variables then can be used to calculate the particle charge density $\rho(r)$ and spin-magnetization density $m(r)$ from

$$\rho(r) = \rho^{\alpha}(r) + \rho^{\beta}(r), \tag{3.40}$$

and

$$m(r) = \mu_B(\rho^{\alpha}(r) - \rho^{\beta}(r)), \tag{3.41}$$

where $\mu_B = eh/2m_ec$ is the Bohr magneton. Then the Hohenberg-Kohn Theorems can be proved, showing that the ground state wavefunction and all ground state observables are unique functionals of $\rho(r)$ and $m(r)$ or, equivalently, $\rho^{\alpha}(r)$ and $\rho^{\beta}(r)$. Similarly, the Kohn-Sham equations can be developed with spin-dependent effective potentials $V_{eff,\sigma}(r)$ as follows,

$$\begin{Bmatrix} \left[ -\frac{1}{2}\nabla^2 + V_{eff,\alpha}(r) \right] \varphi_{i,\alpha} = \varepsilon_{i,\alpha}\varphi_{i,\alpha} \\ \left[ -\frac{1}{2}\nabla^2 + V_{eff,\beta}(r) \right] \varphi_{i,\beta} = \varepsilon_{i,\beta}\varphi_{i,\beta} \end{Bmatrix}, \tag{3.42}$$

where

$$\begin{Bmatrix} V_{eff,\alpha}(r) \\ V_{eff,\beta}(r) \end{Bmatrix} = V(r) + \int \frac{\rho(r')}{|r-r'|} dr' + \begin{Bmatrix} \left( \frac{\delta E_{xc}\left[\rho^\alpha, \rho^\beta\right]}{\delta \rho^\alpha(r)} \right)_{\rho^\beta(r)} \\ \left( \frac{\delta E_{xc}\left[\rho^\alpha, \rho^\beta\right]}{\delta \rho^\beta(r)} \right)_{\rho^\alpha(r)} \end{Bmatrix}, \tag{3.43}$$

i.e.
$$\begin{Bmatrix} V_{eff,\alpha}(r) \\ V_{eff,\beta}(r) \end{Bmatrix} = V(r) + \int \frac{\rho(r')}{|r-r'|} dr' + \begin{Bmatrix} V_{xc,\alpha}(r) \\ V_{xc,\beta}(r) \end{Bmatrix}. \tag{3.44}$$

Spin density functional theory is essential in the theory of atoms and molecules with net spins, as well as solids with magnetic order. In fact, all modern density functional calculations are spin density functional calculations.

## 3.3 Approximations of $\boldsymbol{E}_{xc}\left[\rho\right]$: L(S)DA and GGA

The density functional theory as it has been discussed up to this point is exact and no approximation has been introduced into this theory. However, the exchange correlation energy functional $E_{xc}\left[\rho\right]$, though well defined and exact in principle, is not known exactly. Therefore, to make the density functional theory a practical tool for electronic calculations, we have to introduce approximation to express explicitly the exchange correlation energy functional $E_{xc}\left[\rho\right]$.

The simplest approximation of the exchange correlation energy is the local (spin) density approximation (L(S)DA) proposed by Kohn and Sham in 1965 [6]. The main idea of LSDA is that the real inhomogeneous electronic systems can often be regarded as locally homogeneous as the homogeneous electron gas having the same density. Thus, the exchange correlation energy is simply an integral over all space with the exchange correlation energy density $\varepsilon_{xc}^{h}$ at each point,

$$\begin{aligned} E_{xc}^{LSDA}\left[\rho^{\alpha},\rho^{\beta}\right] &= \int \rho(r)\varepsilon_{xc}^{h}(\rho^{\alpha}(r),\rho^{\beta}(r))d^{3}r \\ &= \int \rho(r)\left[\varepsilon_{x}^{h}(\rho^{\alpha}(r),\rho^{\beta}(r)) + \varepsilon_{c}^{h}(\rho^{\alpha}(r),\rho^{\beta}(r))\right]d^{3}r. \end{aligned} \tag{3.45}$$

In the second step $\varepsilon_{xc}^{h}$ has been divided into two parts: an exchange part $\varepsilon_{x}^{h}$ and a correlation part $\varepsilon_{c}^{h}$

$$\varepsilon_{xc}^{h}(\rho^{\alpha}(r),\rho^{\beta}(r)) = \varepsilon_{x}^{h}(\rho^{\alpha}(r),\rho^{\beta}(r)) + \varepsilon_{c}^{h}(\rho^{\alpha}(r),\rho^{\beta}(r)). \tag{3.46}$$

Since the exchange energy of the homogeneous gas has a simple analytical form and the correlation energy has been calculated to great accuracy using the Quantum Monte Carlo methods, we can obtain an explicit form for the exchange correlation energy based on this approximation and then we can solve the Kohn-Sham equations.

Although it is simple, the LSDA is a very successful approximation for many systems of interest, not only for those where the electronic density is quite homogeneous (these are the systems that the approximation was designed to work with), but also for less uniform systems where the electronic density is rapidly varying. However, there are also a number of problems with the LSDA [26-29]. For instance, it

usually overestimates the bonding energies but underestimates the energy band gap in insulate crystals.

To overcome these and other problems of LSDA, it is natural to improve the exchange correlation energy functional in LSDA by introducing a dependence on the gradient of the electron density, which is call the General Gradient Approximation (GGA) [30-35]. The GGA expression for the exchange correlation energy functional looks like

$$E_{xc}^{GGA}\left[\rho^{\alpha},\rho^{\beta}\right]=\int\rho(r)\varepsilon_{xc}\left[\rho^{\alpha},\rho^{\beta}\right]dr+\int F_{xc}\left[\rho^{\alpha},\rho^{\beta},\nabla\rho^{\alpha},\nabla\rho^{\beta}\right]dr, \qquad (3.47)$$

where the functional $F_{xc}$ is constructed under guidance of wave vector analysis of the exchange correlation energy to satisfy certain formal conditions, such as the sum rule, the physical asymptotic behaviors and so on. Several expressions of the exchange correlation energy density have been described in different formulations of the GGA functionals.

GGA did improve the descriptions of some systems over LSDA. One of the famous examples is that GGA has predicted the correct ground state of bulk Fe to be ferromagnetic body-centered cubic structure [36], while the LSDA has predicted a wrong non-ferromagnetic face-centered cubic structure [37-40]. GGA also reproduces the binding energies, atomic energies and bond lengths better than LSDA. Nevertheless, there still exist some systems which cannot be properly described by GGA because of its semi-local nature. What is worse is that no systematic way has been developed to improve the functionals for exchange and correlation. The problems are most severe in

materials in which the electrons tend to be localized and strongly interacting, such as transition metal oxides and rare earth elements and compounds.

## 3.4 Solving the Kohn-Sham Equations

At this point, we can consider solving the Kohn-Sham equations to obtain the quantities we want. However, it is still a formidable task to handle an infinite number of non-interacting electrons moving in the static potential of an infinite number of nuclei or ions in solids. There exist two difficulties: a wavefunction must be calculated for each of the infinite number of electrons in the system, and since each electronic wavefunction extends over the entire solid, the basis set required to expand each wavefunction is infinite. To overcome these problems, we must invoke some theories and approximations to reduce the infinite systems to finite ones.

### 3.4.1 Bloch's Theorem and $\boldsymbol{k}$ Point Sampling

Although the pure crystal is infinite in principle, the constituent ions are supposed to be at rest in their equilibrium positions and form a periodically repeated structure. In this case the electrons can be considered to move in a static potential $V(r)$ , which may be the Kohn-Sham effective potential. Because of the periodicity of the crystal structure, this potential is also periodic. In mathematic words, the potential satisfies

$$V(L+r)=V(r) \tag{3.55}$$

for all Bravais lattice vectors $L$ .

The Bloch's theorem [41, 42] states that the one-electron wavefunctions of electrons moving in this type of potential can be chosen to have the form of plane wave times a function with the periodicity of the Bravais lattice:

$$\varphi_{nk}(r) = e^{ik\cdot r} u_{nk}(r), \tag{3.56}$$

where $k$ is the wave vector related to the translational properties and $n$ is the band index labeling different eigenstates corresponding to the same $k$, and

$$u_{nk}(L + r) = u_{nk}(r) \tag{3.57}$$

for all $L$ in the Bravais lattice.

Combining the above two equations we obtain

$$\varphi_{nk}(r + L) = e^{ik\cdot L} \varphi_{nk}(r). \tag{3.58}$$

From this equation, we see that the Bloch's theorem have changed the problem of calculating an infinite number of electronic wavefunctions to one of calculating a finite number of electronic wavefunctions at an infinite number of $k$ points.

On the other hand, the wave vector $k$ can always be confined to the first Brillouin zone or to any other convenient primitive cell of the reciprocal lattice. This is because any $k'$ not in the first Brillouin zone can be written as

$$k' = k + G, \tag{3.59}$$

where $k$ does lie in the first Brillouin zone and $G$ is a reciprocal lattice vector defined by

$$G \cdot L = 2\pi m \quad (m \text{ is an integer}) \tag{3.60}$$

for all lattice vectors $L$. Thus we can restrict our attention to those $k$ vectors which lie within the first Brillouin zone.

The $k$ points required in the electronic states calculations can be further reduced by the use of a small special set of $k$ points in the first Brillouin zone, which is based on the fact that the electronic wavefunctions and other properties at $k$ points that are very close together will be almost identical. Different methods [43-45] have been devised to choose the special points for obtaining very accurate approximation to the electronic potential and the total energy. The magnitude of any error due to the selection of special $k$ points can always be reduced by choosing a denser set of $k$ points.

### 3.4.2 Plane Wave Basis Sets and Pseudopotential Approximation

Solving the Kohn-Sham equations is an integral-differential problem, which is hard to attack in practical calculations. Therefore, it is necessary to transform this problem into an easier one. This can be achieved by expanding the electronic wavefunctions with a basis set. The plane wave basis set [46] seems a natural choice since the Bloch's theorem states that the electronic wavefunctions at each $k$ point can be expanded in terms of a discrete plane wave basis set. In addition, plane wave basis sets offer many advantages in density functional calculations for solids, including completeness, an unbiased representation (parameter free), arbitrarily good convergence accuracy and the ability to use the Fast Fourier Transform (FFT) to move back and forth between real and reciprocal spaces.

In principle, to obtain exact expansions of the electronic wavefunctions, an infinite plane wave set is required. But in practice, it is impossible because we can only handle a finite number of plane waves. Thus the plane wave set is usually truncated to include only plane waves that have kinetic energies less than some particular cutoff energy $E_{cut}$:

$$\frac{\hbar^2}{2m}\left|k+G\right|^2 \le E_{cut}. \tag{3.61}$$

In this way, a finite plane wave basis set is produced. The truncation of the plane wave basis set at a finite cutoff energy will certainly lead to the accuracy concerns in the computed results. But it is possible to reach the accuracies we want by increasing the value of the cutoff energy until the calculated results have converged.

However it is still computationally too difficult in the real calculations even after the above methods and approximations are introduced. This is because a large number of plane waves are required to model accurately the core wavefunctions which oscillate rapidly with many nodes. A possible way to overcome this difficulty is the pseudopotential approximation [47-54] which is based on the fact that most physical properties of solids are dependent on the valence electrons to a much greater extent than on the core electrons. The pseudopotential method removes the core electrons and replaces them and the strong Coulomb potential by a much smoother pseudopotential and replaces the valence electron wavefunctions with a set of pseudo, smoothly varying wavefunctions which have no radial nodes in the core region. By doing so, the number of plane waves needed to expand the electronic wavefunctions is reduced significantly

and fewer electronic wavefunctions have to be calculated because of the removal of the core electrons.

The pseudopotential approximation, especially the Vanderbilt's ultrasoft pseudopotential [54] approach is now widely used in the electronic structure calculations [55-59]. But the success of the method is partly hampered by the rather difficult generation of the pseudopotentials. It is also reported that the pseudopotentials fail in spin-polarized calculations for materials with a large magnetic moment [60]. The three methods described in the following sections are alternatives to the pseudopotential approach.

### 3.4.3 The Full Potential Linearized Augmented Plane Wave (FLAPW) Method

The FLAPW method [61-63] is an all-electron method developed within density functional theory, universally applicable to all atoms of the periodic table and to systems with compact as well as open structures and widely considered to be the most precise electronic structure method in solid state physics. It is a generalization of the LAPW (Linearized Augmented Plane Wave) [64-66] method in that it removes the shape approximation to the potential inside the atomic spheres. Unlike the pseudopotential method which uses plane waves as basis set, the FLAPW method employs the augmented plane wave basis set as its predecessors, the APW (Augmented Plane Wave) method [67-69] and the LAPW method, did.

Similar to the motivation of the introduction of the pseudopotential method, the idea leading to APW method is that near an atomic nucleus the potential and

wavefunctions are similar to those in an isolated atom – they are strongly varying but nearly spherical. The electrons in this region can be described more efficiently by atomic like functions. However, in the interstitial space between the atoms both the potential and wavefunctions are smoother. The electrons in this region behave more or less as free electrons, and thus can be described by plane waves. Naturally, space is accordingly partitioned into two regions as shown in Figure 3.4: atom-centered spheres with radius $R_\alpha$, called muffin-tin sphere region (S), and the interstitial region (I). The muffin-tin spheres do not overlap and they are typically chosen such that they nearly fill the maximal possible space. The wavefunction is expanded as

$$\varphi(\vec{r}) = \begin{cases} \Omega^{-1/2} \Sigma_{\vec{G}} c_{\vec{G}} e^{i(\vec{G}+\vec{k})\cdot\vec{r}} & \vec{r} \in I \\ \\ \Sigma_{lm} A_{lm} u_l(r) Y_{lm}(\hat{r}) & \vec{r} \in S, \end{cases} \tag{3.62}$$

where $\varphi$ is a wave function, $\Omega$ is the cell volume, $u_l$ is the regular solution of radial part of the Schrödinger's equation in the sphere

$$[-\frac{d^2}{dr^2} + \frac{l(l+1)}{r^2} + V(r) - E_l)]ru_l(r) = 0. \tag{3.63}$$

Here $c_G$ and $A_{lm}$ are expansion coefficients, $E_l$ is an energy parameter and $V$ is the spherical component of the potential in the sphere. $A_{lm}$ is determined from the requirement that the wavefunctions are continuous (in value but in slope) at the boundary of the muffin-tin spheres in order for the kinetic energy to be well-defined.

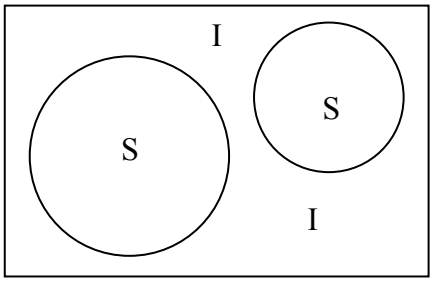


Figure 3.4 Division of the unit cell into muffin-tin regions (S) and the interstitial region (I), for a case with two atoms.

There are several difficulties connected with the APW method. For example, The augmented plane waves are solutions of the Schrödinger's equation inside the spheres, but only at the energy $E_l$. If $E_l$ kept fixed, it turns out that the APW basis does not offer enough variational freedom. An accurate description can only be achieved if the energies are set to the corresponding band energies. Accordingly the Hamiltonian energy dependent and the energy bands at a fixed *k*-point cannot be obtained from a single diagonalization as in pseudopotential method. This makes the APW method inherently much slower than the pseudopotential method.

To circumvent these difficulties with the APW method, several modifications were proposed. One of them is the LAPW method. In the LAPW method, the basis functions inside the spheres are linear combinations of radial functions $u_l(r)Y_{lm}(\hat{r})$ and their derivatives with respect to the parameters, $E_l$. The energy derivative $\dot{u}_l(r)Y_{lm}(\hat{r})$ satisfies

$$[-\frac{d^2}{dr^2}+\frac{l(l+1)}{r^2}+V(r)-E_l)]r\dot{u}_l(r)=ru_l(r). \qquad (3.64)$$

These functions are matched to the values and derivatives of the planewaves on the muffin-tin sphere boundaries. The wavefunctions in terms of the LAPW basis are,

$$\varphi(\vec{r}) = \begin{cases} \Omega^{-1/2}\Sigma_{\vec{G}} c_{\vec{G}} e^{i(\vec{G}+\vec{k})\cdot\vec{r}} & \vec{r}\in I \\ \Sigma_{lm}[A_{lm}u_l(r)+B_{lm}\dot{u}_l(r)]Y_{lm}(\hat{r}) & \vec{r}\in S, \end{cases} \tag{3.65}$$

where the $B_{lm}$ are coefficients for the energy derivative, and determined by the requirement that the first derivatives of wavefunctions are continuous at muffin-tin boundary.

As in the APW method, the LAPWs are planewaves in the interstitial region, but inside the spheres the LAPWs have more variational freedom than APWs. This is because a linear combination will reproduce the APW radial function constructed at the band energy $\varepsilon$ if $E_l$ differs slightly from the band energy.

$$u_l(\varepsilon, r) = u_l(E_l, r) + (\varepsilon - E_l)\dot{u}_l(\varepsilon, r) + O((\varepsilon - E_l)^2). \tag{3.66}$$

The last term in Eq. (3.66) denotes errors that are quadratic in this energy difference. The APW method will yield exactly the correction wavefunction for a converged, infinite planewave set and a muffin-tin potential. For the LAPW method, it will introduce errors of order $(\varepsilon - E_l)^2$ in the wavefunction and errors of order $(\varepsilon - E_l)^4$ in the band energy according to the variational principle. Because of this high order of error, the LAPWs form a good basis set over a relatively large energy region, so that all valence bands may typically be treated with a single set of $E_l$. Therefore, in the LAPW method accurate energy bands at a given *k*-point can be obtained with a single diagonization, an enormous simplification over the APW method.

In the LAPW method, the full potential and charge density are treated everywhere in space except inside the muffin tin sphere, where a spherical-shape approximation is used. While calculations employing the LAPW method yielded accurate results for close-packed metal systems, the spherical-shape approximation cannot be justified for open structures such as semiconductors and reduced symmetry solids, e.g., films and interfaces, and the localization inherent in molecules on solid surfaces.

The FLAPW method was developed to remove this spherical-shape approximation and obtain the Coulomb potential for a general periodic charge distribution. The method is based on the fact that the potential outside the muffin tin spheres does not depend on the actual shape of the charge density inside the spheres but only on the multipole moments of the charge. Hence the true rapidly varying charge inside the muffin tin spheres can be replaced by another smoother pseudo charge density with the correct multipole moments without changing the potential outside the spheres. The potential inside the spheres then can be obtained by solving the boundary value problem using the true charge density in the region.

### 3.4.4 The Projector Augmented Wave (PAW) Method

Some of the disadvantages of the pseudopotential method can be avoided in the all electron projector augmented wave (PAW) method [60, 70-71] proposed by Blöchl. This method combines the ideas of the pseudopotential [47-54] and linearized augmented plane wave (LAPW) [61-66] methods. In the PAW method, the all-electron

(AE) wavefunction is constructed from a pseudo (PS) wavefunction and atom-like functions localized near the nuclei. The PS wavefunction $|\tilde{\varphi}\rangle$ coincides with the AE wavefunction $|\varphi\rangle$ in the interstitial region, i.e., outside the atomic regions. Inside the atomic region, or called augmentation region, the wavefunction is almost atom-like because the effect of the surrounding crystal is small. Therefore, a natural choice is to use solutions $|\phi_\Lambda\rangle$ of Schrödinger equation for the isolated atom, the so-called AE partial waves, as a basis set for the augmentation region. Here $\Lambda = \{t, n, l, m\}$ is a global index for the atom $t$ , the angular momentum $l$ , the magnetic quantum number $m$ , and the index $n$ , the energy for which Schrödinger equation is solved. Then the AE wavefunction is related to the PS wavefunction through a linear transformation:

$$|\varphi_n\rangle = |\tilde{\varphi}_n\rangle + \sum_\Lambda \left( |\phi_\Lambda\rangle - |\tilde{\phi}_\Lambda\rangle \right) \langle \tilde{p}_\Lambda | \tilde{\varphi}_n \rangle \tag{3.67}$$

where $|\tilde{\phi}_\Lambda\rangle$ is introduced PS partial wavefunctions which are centered on the atom. They are equivalent to the AE partial waves $|\phi_\Lambda\rangle$ outside their augmentation regions and match continuous onto $|\tilde{\phi}_\Lambda\rangle$ inside the augmentation regions. The projector functions $\langle \tilde{p}_\Lambda |$ are dual to the PS partial waves:

$$\langle \tilde{p}_\Lambda | \tilde{\phi}_{\Lambda'} \rangle = \delta_{\Lambda\Lambda'}. \tag{3.68}$$

The first term in equation (3.68) represents the PS wavefunction defined over the entire space, which is equal to the AE wavefunction in the interstitial region, and which is expanded in plane waves. The second term is the AE partial wave expansions, which

describes the correct nodal behavior of the wavefunction in the augmentation region. The third term eliminates the spurious contribution of the PS wavefunction in the augmentation region.

From equation (3.68), the AE charge density can be obtained:

$$\rho(r) = \tilde{\rho}(r) + \rho^1(r) - \tilde{\rho}^1(r) \tag{3.69}$$

where $\tilde{\rho}(r)$ is the pseudo charge density related directly to the PS wavefunctions $|\tilde{\varphi}_n\rangle$

$$\tilde{\rho}(r) = \sum_n f_n \langle \tilde{\varphi}_n | r \rangle \langle r | \tilde{\varphi}_n \rangle \tag{3.70}$$

with $f_n$ defined as orbital occupation numbers for the *n*th state. The onsite charge densities $\rho^1(r)$ and $\tilde{\rho}^1(r)$ are only defined inside the augmentation regions of each atom. They are defined as

$$\rho^1(r) = \sum_{(\Lambda,\Lambda')} P^{PAW}_{\Lambda,\Lambda'} \langle \phi_\Lambda | r \rangle \langle r | \phi_{\Lambda'} \rangle, \tag{3.71}$$

and

$$\tilde{\rho}^1(r) = \sum_{(\Lambda,\Lambda')} P^{PAW}_{\Lambda,\Lambda'} \langle \tilde{\phi}_\Lambda | r \rangle \langle r | \tilde{\phi}_{\Lambda'} \rangle. \tag{3.72}$$

The matrix $P^{PAW}_{\Lambda,\Lambda'}$ describes the occupancies of each augmentation channel $(\Lambda, \Lambda')$ and is calculated from the PS wavefunctions applying the projector functions:

$$P^{PAW}_{\Lambda,\Lambda'} = \sum_n f_n \langle \tilde{\varphi}_n | \tilde{p}_\Lambda \rangle \langle \tilde{p}_{\Lambda'} | \tilde{\varphi}_n \rangle. \tag{3.73}$$

Generally speaking, the PAW potentials are more accurate than the pseudopotentials. This is because that firstly the radial cutoffs (core radii) are smaller than the radii used for the pseudopotentials. Thus the required energy cutoffs and basis

sets are somewhat larger. Secondly, the PAW potentials reconstruct the exact valence wavefunctions with all nodes in the core region through the cut-and-paste way as given by equation (3.68).

### 3.4.5 The Linearized Muffin-tin Orbitals (LMTO) Method

As in the LAPW method, the space in the LMTO method [64, 72-73] is also divided into muffin-tin spheres and interstitial region (Fig 3.4). In open systems such as the diamond structure, additional empty spheres are added to the large empty spaces. The difference between the LAPW method and the LMTO method is that different mathematical functions are used to describe the one-electron wavefunctions. In the LAPW method, Bessel function is involved in the expansion coefficients, whereas in the LMTO method, we use Hankel function. In our calculations, the atomic-spheres approximation (ASA) is also employed. This approximation assumes that the potential is spherically symmetric around each atom and constant between the atoms:

$$V(\vec{r}) = \begin{cases} \sum_R V_R(r_R) & \vec{r} \in \text{sphere} \\ V_0 & \vec{r} \in \text{interstitial}, \end{cases} \tag{3.74}$$

where $V$ is the approximated atomic potential.

The wavefunctions can be written as

$$\varphi(\vec{r}) = \begin{cases} \sum_{lm} u_l Y_{lm}(\hat{r}) & \vec{r} \in sphere \\ \sum_{lm} i_l k^{(l+1)} h_l(kr) Y_{lm}(\hat{r}) & \vec{r} \in interstitial, \end{cases} \tag{3.75}$$

Where $h_l$ is a Hankel function and $k = \sqrt{E - V_0}$ is a constant wave number and other symbols have the same meanings as explained previously. As in the (F)LAPW method, the LMTOs constructed as such are energy-independent.

### 3.4.6 The Self-Consistent Procedure

The solution of Kohn-Sham equations has to be obtained by an iterative, self-consistent procedure. The reason is that the effective potential $V_{eff}(r)$ depends on the charge density $\rho(r)$ , which we are solving for. This procedure begins with initially guessed charge densities $\rho^{\alpha}(r)$ and $\rho^{\beta}(r)$ , constructs the KS effective potentials from equation (3.43), and then finds the new output charge densities from equations (3.42) and (3.39) to begin another loop until the input and output charge densities are self-consistent. Then the interested quantities can be computed from the self-consistent charge densities or wavefunctions.

This self-consistent loop is shown schematically in Figure 3.5.

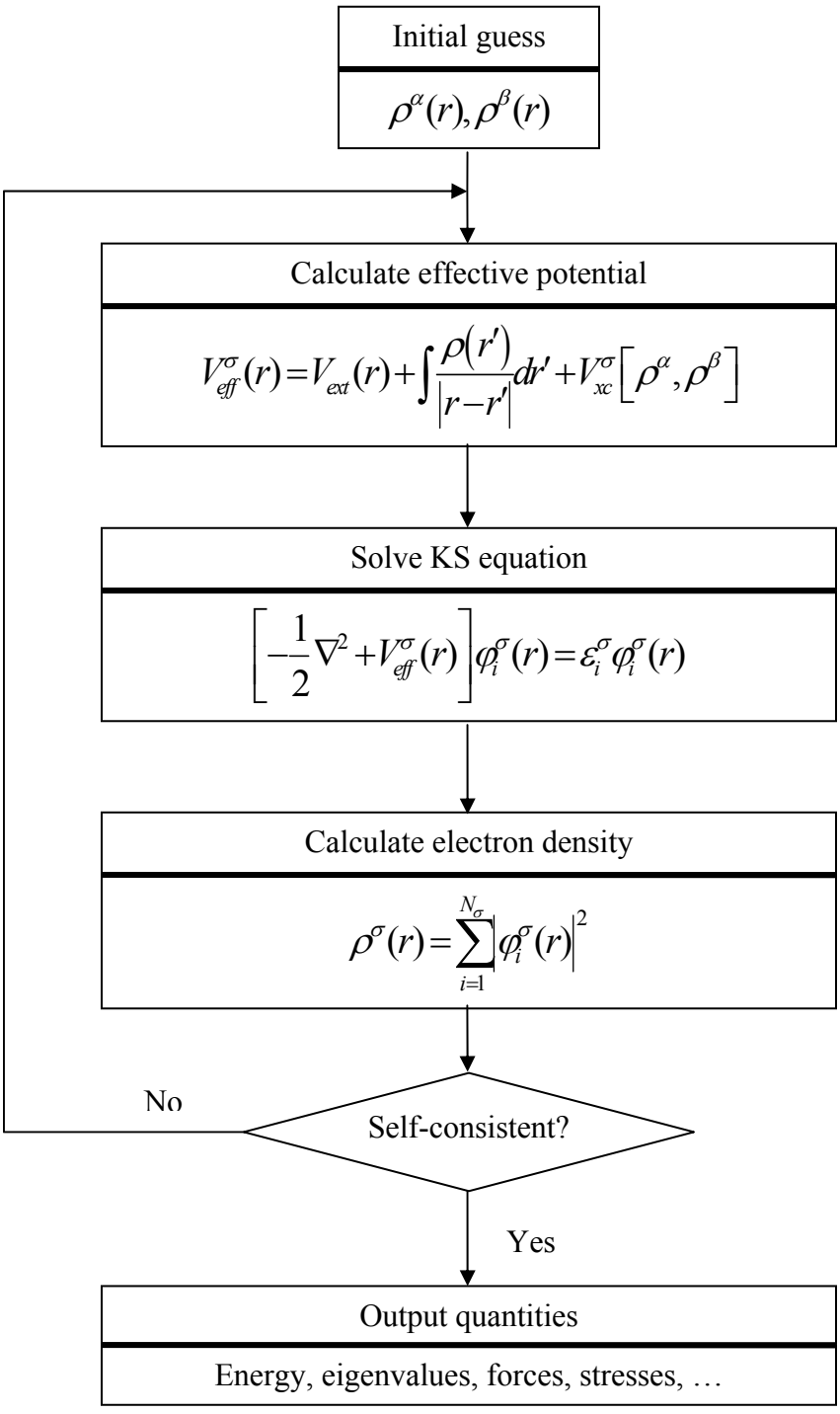


Figure 3.5 Schematic representation of the self-consistent loop to solve the Kohn-Sham equations. Adapted from [19].

# CHAPTER 4

# STRUCTURAL AND MAGNETIC PROPERTIES OF SOFT PHASE MATERIALS

As a component of the nanocomposite magnets, soft phase materials certainly will affect the performance and properties of the nanocomposite magnets. It is known that the critical size of soft phase strongly depends on various bulk-like parameters such as saturated magnetization, interatomic exchange interaction and magnetic anisotropy [13-16]. Appropriate soft magnetic materials for the synthesis of exchange coupled soft/hard magnets should have both high magnetization and high magnetocrystalline anisotropy energy. To this end, FeCo alloys are particularly attractive because of their peculiar properties. For instance, stoichiometric FeCo alloys show the largest magnetic permeability of any material and the magnetic anisotropy coefficient, $K_1$, is vanishingly small. Depending on temperature and composition, FeCo may adopt either ordered or disordered phases in bcc, fcc or hcp Bravais lattice. For the manipulation of their physical properties, one needs to understand the key factors that govern the phase stability, magnetization and magnetic anisotropy of these systems. In this chapter, I focus on the stability and magnetic properties of soft phase FeCo alloys from our systematic density functional studies. Specifically, we have found that while the bcc-type FeCo alloys are stable, the fcc- or hcp-type FeCo alloys are not. For the stable bcc-type FeCo alloys, non-cubic geometries are preferred in a wide range of composition.

Accordingly this produces appreciable uniaxial magnetic anisotropy, which facilitates the magnetic interaction between the hard and soft phases and eventually enhancing the maximum energy product of the exchange-coupled nanocomposite systems [74].

## 4.1 Stability and Structure of FeCo Alloys

The structural stability of FeCo alloys is quantitatively characterized through their formation energies defined as

$$E_b(Co_mFe_n) = E_{tot}(Co_mFe_n) - m\mu_{Co} - n\mu_{Fe}, \quad (4.1)$$

where $E_{tot}(Co_mFe_n)$ is the total energy of the structurally optimized $Co_mFe_n$ alloy with *m* Co atoms and *n* Fe atoms in the unit cell. $\mu_{Co}$ and $\mu_{Fe}$ represent chemical potentials, or practically total energies per atom, of pure Co and Fe source metals, respectively. As usual, alloys with negative $E_b$ are stable while those with positive $E_b$ tend to segregate apart into elemental Fe and Co metals.

To compute the total energies and the chemical potentials, we used the VASP package [60, 75-78]. The projector augmented wave (PAW) method [60, 70-71] implemented in VASP was used to describe the electron-ion interactions. The PAW potentials for Fe and Co were generated from the atomic configuration of [Ar]$3d^74s^1$ and [Ar] $3d^84s^1$, respectively. The *3d* and *4s* electrons were treated as valence electrons. The spin-polarized generalized gradient approximation (GGA) was adopted for the description of exchange-correlation interactions among electrons. At the level of the LSDA, the exchange-correlation functional proposed by Perdew and Zunger [94] based on the quantum Monte Carlo calculations of Ceperley and Alder [95] was used.

In the total energy calculations, the integrations over the irreducible first Brillouin zone were carried out by using an 8×8×8 *k*-point set generated according to the Γ centered Monkhorst-Pack scheme [45]. The plane wave energy cutoff was set at 335 eV (24.62 Ry) to ensure the convergence of the calculations. The systems under investigation were initially set with a certain structure (bcc, hcp or fcc, hereafter we call these systems accordingly bcc-, hcp- or fcc-type alloys), then all atomic degrees of freedom, i.e., the unit cell axis, as well as the position of the atoms, were optimized to find the lowest total energy of a given system. For the bcc- and hcp-type systems, there are 16 atoms totally in the supercell, whereas in the fcc-type systems, there are only 8 atoms in the supercell.

We have considered all non-equivalent configurations for every specific system with certain atomic composition. For example, in the bcc-type alloys, there are 12 different configurations for $Fe_{11}Co_5$ system and there are 7 different configurations for $Fe_{12}Co_4$ system. Figure 4.1 shows the 12 possible configurations of bcc-type $Fe_{11}Co_5$ system. We optimized all these configurations for each system and compared their total energies and then chose the configuration with the lowest total energy as our optimized structure for the system. We found that the optimized structures for most of the systems are not in cubic geometry anymore even though we initially started their structures as cubic. For instance, $Fe_{12}Co_4$ has a tetragonal structure with a=b=5.69 Å and c=5.67 Å after full relaxation and optimization. We also noticed that the atoms with minor composition tends to separate apart in these alloys, which is in agreement with the conclusion reported previously [79]. In a recent density functional calculation, Fu *et al.*

found the site-exchange energy in the stoichiometric $B_2$ FeCo alloy is 0.34 eV, which gives an excellent order-disorder transition temperature, 987 K [80]. In addition, there is no energy barrier between fcc and bcc lattice for the stoichiometric B2. Our VASP calculations for stoichiometric FeCo with a well-separated antisite pair give 0.26 eV for the site-exchange energy, slightly smaller than the value of Fu *et al* obtained from the all electron FLAPW calculations.

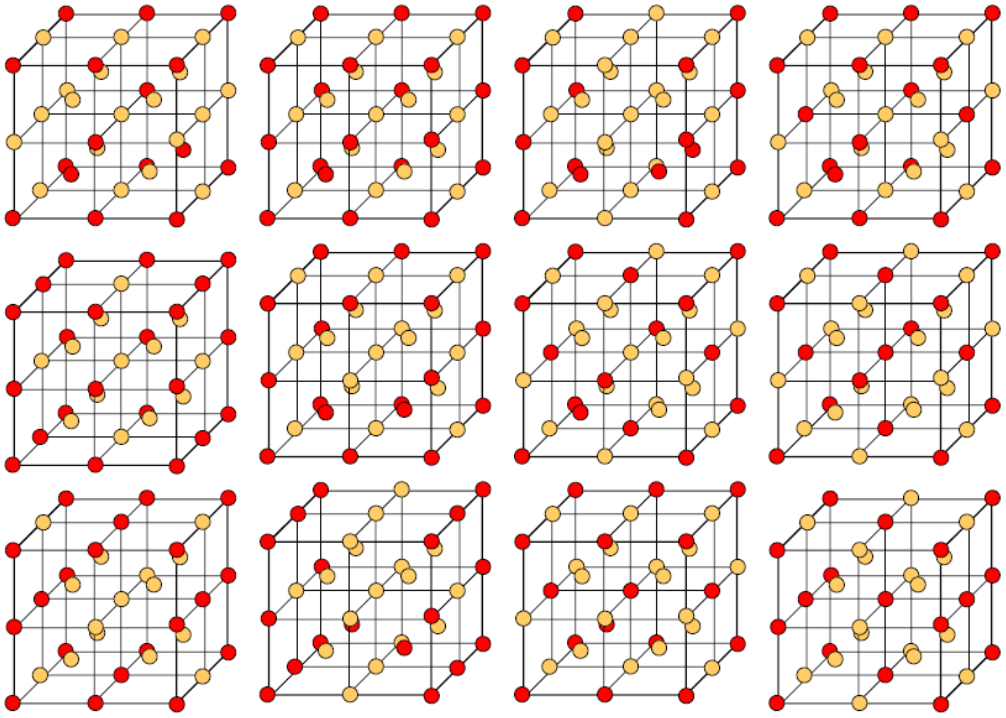

Figure 4.1 Twelve (all) possible configurations for the bcc-type $Fe_{11}Co_5$. For every specific system with certain atomic composition, all non-equivalent configurations have been considered in the calculations. Then the configuration with the lowest total energy was chosen as the optimized structure for the system.

To obtain the chemical potentials of Fe and Co, separate calculations were performed to get the total energies of metallic Fe and metallic Co. A 16×16×16 *k*-point set generated by the Monkhorst-Pack scheme is used in these calculations. The

optimized lattice constants from our calculations for Fe and Co are 2.83 Å and 2.49 Å, c/a=1.617, respectively. They are in good agreement with the experimental values of 2.87 Å for Fe and 2.51 Å, c/a=1.622 for Co [81]. The calculated magnetic moments per atom for Fe (2.16 $\mu_B$) and Co (1.56 $\mu_B$) from our study are also in very good agreement with experimental values [7].

The computed formation energies for these FeCo alloys are shown below in Table 4.1. As we can see from the table, the formation energies for the bcc-type FeCo alloys (m>n) are negative whereas for the hcp- or fcc-type alloys, the formation energies are positive. This means that the bcc-type FeCo alloys are stable but the hcp- and fcc-type alloys are not, which is in good accordance with previous studies [80, 82, 83]. Specifically, the formation energies for the Fe-rich bcc-type alloys are all negative except for $Fe_{15}Co_1$, which has a very small positive formation energy. Generally, the Fe-rich bcc-type alloys have larger (in absolute value) formation energies with increasing Co concentration. This indicates that the Fe-rich bcc-type FeCo alloys become more stable when the Co concentration increases. For the Co-rich hcp-type FeCo alloys, the formation energies become larger and larger with increasing Fe concentration. However, because they all have positive formation energies, these hcp-type alloys thus become less and less stable when the Fe concentration increases. Strikingly, $E_b$ for the *hcp* $Co_8Fe_8$ becomes as large as 1.73 eV, indicating that Fe-Co bonds are rather directional and the alloy rather form separated Fe and Co phases. For the fcc-type alloys, the positive formation energies generally increase with increasing

Fe concentration and decreasing Co concentration. Therefore, these fcc-type FeCo alloys become less stable when Fe concentration increases.

Table 4.1 Formation energies for FeCo alloys as defined in Eq. (4.1). The systems were initially set in bcc, fcc or hcp structures and then fully relaxed, including the cell shape and volume. A negative value implies a stable alloy versus the two segregative Fe and Co metals.

| System | | Formation energy (eV) | System | | Formation energy (eV) | System | | Formation energy (eV) |
|---|---|---|---|---|---|---|---|---|
| bcc | $Fe_8Co_8$ | -0.51 | hcp | $Co_8Fe_8$ | 1.73 | fcc | $Fe_1Co_7$ | 0.15 |
| | $Fe_9Co_7$ | -0.50 | | $Co_9Fe_7$ | 0.38 | | $Fe_2Co_6$ | 0.17 |
| | $Fe_{10}Co_6$ | -0.55 | | $Co_{10}Fe_6$ | 0.46 | | $Fe_3Co_5$ | 0.37 |
| | $Fe_{11}Co_5$ | -0.49 | | $Co_{11}Fe_5$ | 0.51 | | $Fe_4Co_4$ | 0.56 |
| | $Fe_{12}Co_4$ | -0.36 | | $Co_{12}Fe_4$ | 0.70 | | $Fe_5Co_3$ | 0.76 |
| | $Fe_{13}Co_3$ | -0.23 | | $Co_{13}Fe_3$ | 0.51 | | $Fe_6Co_2$ | 0.87 |
| | $Fe_{14}Co_2$ | -0.11 | | $Co_{14}Fe_2$ | 0.25 | | $Fe_7Co_1$ | 0.74 |
| | $Fe_{15}Co_1$ | 0.03 | | $Co_{15}Fe_1$ | 0.10 | | | |

Another important finding from our study is that chemically non-cubic geometries are preferred in a wide composition range, in agreement with previous studies [82-83]. As illustrated in the first row of Figure 4.2, $Fe_{11}Co_5$, $Fe_{12}Co_4$, and $Fe_{13}Co_3$ can be arranged with the cubic symmetry. However, according to our calculations, these cubic structures appear to be the least stable one among all possible geometries as long as there are no Co atoms as first neighbor. For $Fe_{12}Co_4$ (or equivalently $Fe_3Co$), the $L6_0$ structure is more stable than the cubic $DO_3$ structure by 60 meV/cell through VASP calculations or 70 meV/cell through more precise FLAPW calculation. Since the phase transition can be achieved by swapping only one Co-Fe pair

in the cell along either the (100) or (110) direction, it should be easy to occur if the sample is annealed. For $Fe_{11}Co_5$ and $Fe_{13}Co_3$, the non-cubic geometries as shown in the second row in Figure 4.2 are also more stable than their corresponding cubic geometries, by 30 meV/cell and 21 meV/cell respectively, from our VASP calculations.

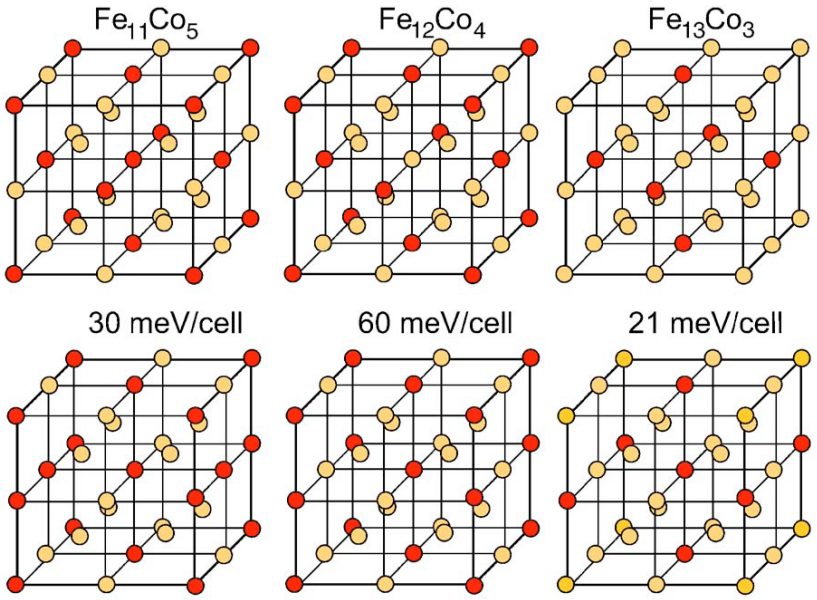


Figure 4.2 Atomic configurations for the cubic (in the top row) and ground state (in the bottom row) structures of $Fe_{11}Co_5$, $Fe_{12}Co_4$, and $Fe_{13}Co_3$ alloys. Fe and Co atoms are represented by yellow and red circles, respectively. The numbers in between the two rows indicate the energy gains after the tetragonal distortion for each corresponding system.

To explain this phenomenon, we plotted the density of states (DOS) for $Fe_{12}Co_4$ in both $L6_0$ and $DO_3$ structures as shown in Figure 4.3. In the plot, solid and dashed curves represent the DOS for the $L6_0$ and $DO_3$ structures, respectively, and their corresponding thinner lines represent contributions from the Co atoms. The DOS for the majority and minority spins are plotted in positive and negative regions along the

vertical axis, respectively. The Fermi level is set at zero energy. Obviously, the major difference occurs in -1.8~-1.0 eV and +1.5~+2.0 eV, mostly on the Co sites. Corresponding to the large magnetic moments, the majority spin bands are fully occupied for both Co and Fe. The difference in DOS around the Fermi level is very small. However, the blip in the minority spin channel for the $DO_3$ structure appears to be higher than that of the $L6_0$ structure, which might be a cause for the slight instability of the former phase.

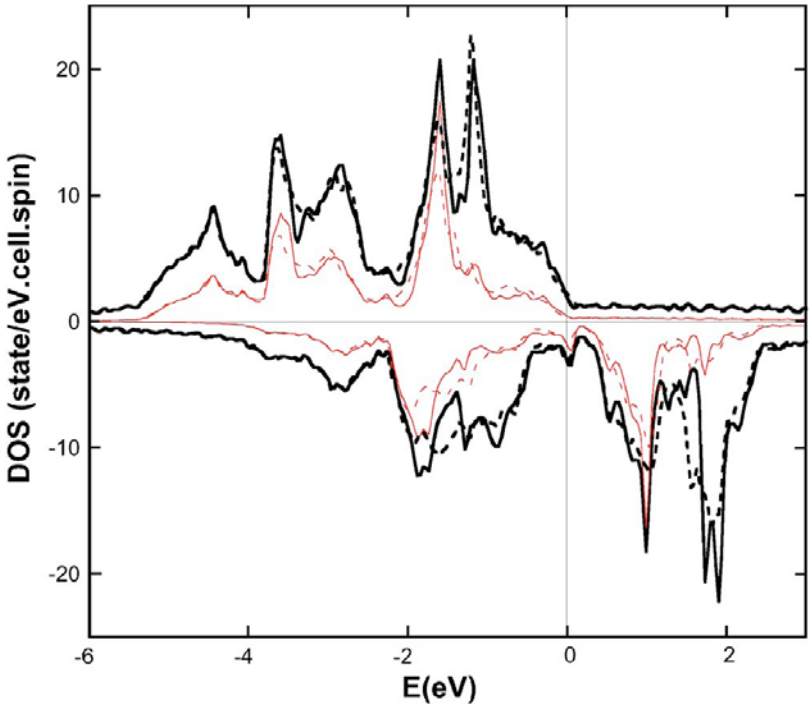


Figure 4.3 The calculated density of states (DOS) of the $Fe_{12}Co_4$ in the $L6_0$ (solid lines) and $DO_3$ (dashed lines) structures. Contributions from the Co atoms are represented by thin lines. Positive and negative regions along the vertical axis are for the majority and minority spins, respectively. Zero energy is the position of the Fermi level.

In contrast with the non-cubic geometry preference of $Fe_{11}Co_5$, $Fe_{12}Co_4$ and $Fe_{13}Co_3$, $Fe_8Co_8$ and $Fe_{15}Co_1$ remain in cubic structure, while other stable Fe-rich bcc-

type systems under investigation also possess non-cubic structures. As we will see in the next section, the non-cubic geometry preference has a very important consequence, i.e., appreciable magnetocrystalline anisotropy energies will be produced in these non-cubic systems.

## 4.2 Magnetic Properties of Stable bcc-type FeCo Alloys

Magnetic anisotropy energy is one of the most important quantities for the integration of hard and soft magnets. In general, FeCo forms disordered alloys and therefore there is no distinction between x, y and z-axes. However, uniaxial magnetic anisotropy for a finite grain might be induced by non-uniform local atomic arrangements and also by lattice distortion (magnetostriction). To estimate the strength of the first effect, we calculate the magnetocrystalline anisotropy energies for $Fe_mCo_n$ alloys in the bcc lattice with a 16-atom unit cell. These calculations are done in FLAPW using the optimized structures of the systems obtained in VASP. In these calculations, no shape approximation is assumed for charge, potential and wave function expansions. The core electrons are treated fully relativistically, while the spin-orbit coupling (SOC) term was invoked second variationally for the valence states. The energy cutoff for the basis functions in the interstitial region is 16 eV. In the muffin-tin (MT) region ($R_{Fe}$=1.22 Å and $R_{Co}$=1.22 Å), the basis functions were expanded in terms of spherical harmonics with a maximum angular momentum of $l_{max}$=8. The convergence of electronic and magnetic properties against the choice of number of k-points and wave function expansion were carefully monitored. The self-consistence was assumed when

the root-mean-square differences between the input output charge and spin densities are less than $3.0\times10^{-5}\ e/(\text{a.u.})^3$.

As proposed by van Vleck [99] more than 70 years ago, the magnetocrystalline anisotropy originates mainly from the spin-orbit coupling (SOC) interaction between spin magnetic moment and orbit magnetic moment. The SOC Hamiltonian, $H^{SOC} = \xi\sigma \cdot L$ (here $\sigma$ and $L$ are spin and orbital angular momentum operators, respectively), however, is very weak compared to the crystal-field effects. Thus, it has been very difficult to determine the magnetocrystalline anisotropy from first-principles calculations, which usually require a large number of k-points and accurate band structure. Pioneering first-principles calculations of magnetocrystalline anisotropy were carried out by Gay *et al.* for ferromagnetic Fe, Co, Ni and V monolayers, and thicker Fe slabs and Fe/Ag(001) [100, 101] by incorporating $H^{SOC}$ as a perturbation. In most of first-principles calculations, the magnetocrystalline anisotropy energy $E_{MCA}$ is obtained from force theorem [84-86] as

$$E_{MCA} = E(\rightarrow) - E(\uparrow) = \sum_{occ'} \varepsilon_i(\rightarrow) - \sum_{occ''} \varepsilon_i(\uparrow), \qquad (4.2)$$

where $E(\rightarrow)$ and $E(\uparrow)$ are the total energies with the magnetization along the directions perpendicular and parallel to the *c* axis, respectively and $\varepsilon_i$ stands for the band energy of the *i*th state. A positive $E_{MCA}$ means that the easy axis of the magnetic anisotropy is parallel to the c axis, while a negative $E_{MCA}$ indicates that the easy axis of the magnetic anisotropy is perpendicular to the c axis. Strong numerical uncertainties are inherent in this approach because the sets of occupied states, i.e., $\{occ'\}$ and $\{occ''\}$,

were determined through the Fermi filling scheme which relies on the very limited information from the eigenvalues $\varepsilon_i$. Using this approach, one has to use a huge number of *k* points for sampling, which is very computationally expensive, to obtain reliable $E_{MCA}$ values.

In our calculations, we chose to use the torque method proposed by Wang *et al.* [87-88] to obtain the magnetocrystalline anisotropy energies of the stable FeCo alloys. To demonstrate the torque method, we note that the total energy of a uniaxial system can be well approximated as

$$E(\theta) = E_0 + K_2 \sin^2(\theta) + K_4 \sin^4(\theta), \tag{4.3}$$

where θ is the angle between the magnetization and the c axis. $K_2$ and $K_4$ are anisotropy constants. The torque, $T(\theta)$, is defined as the angular derivative of the total energy

$$T(\theta) \equiv \frac{dE(\theta)}{d\theta} = K_2 \sin(2\theta) + 2K_4 \sin(2\theta)\sin^2(\theta). \tag{4.4}$$

Combing equations (4.2)-(4.4), it is easy to show that

$$\begin{aligned} E_{MCA} &\equiv E(\theta = 90^\circ) - E(\theta = 0^\circ) \\ &= K_2 + K_4 = T(\theta = 45^\circ). \end{aligned} \tag{4.5}$$

Thus, instead of calculated as a very small difference between two large total energy values, the $E_{MCA}$ can be evaluated very efficiently through calculating the torque at $\theta = 45^\circ$.

To calculate the torque, we then apply the Feynman-Hellman theorem

$$T(\theta) = \sum_{occ} \left\langle \psi_i' \left| \frac{\partial H^{SOC}}{\partial \theta} \right| \psi_i' \right\rangle, \tag{4.6}$$

where $H^{SOC}$ is the spin-orbit coupling Hamiltonian, the only $\theta$-dependent term in the system Hamiltonian, and $\psi_i^{'}$ is the *i*th perturbed wavefunction.

The advantage of the torque method is obvious since $E_{MCA}$ is expressed as the expectation value of the angular derivative of spin-orbit coupling Hamiltonian $H_{soc}$ and thus it is much more insensitive to distortions of the Fermi surface and only one Fermi surface needs to be determined. Therefore, compared to the force theorem approach, the numerical uncertainties in the torque approach are greatly reduced and much less *k* points are needed to obtain stable results of $E_{MCA}$. It has been shown [88] that the torque method is indeed efficient and reliable for the determination of uniaxial and high order magnetic anisotropy energies.

The calculated magnetic moments for bcc-type $Fe_mCo_n$ alloys in the bcc lattice are listed in Table 4.2. It is interesting that the average magnetic moment is insensitive to the change in composition. Nevertheless, the magnetic moment appears to maximize at a ratio m/n=3/1 to 4/1. More explicitly for $Fe_{12}Co_4$ in the $L6_0$ structure, the magnetic moment in Co is 1.80 $\mu_B$, while those for two types of Fe atoms are 2.38 $\mu_B$ (coplanar to Co) and 2.63 $\mu_B$ (in the pure Fe plane). Obviously, the reduction in magnetization by the presence of Co is excessively compensated by the strong enhancement of Fe magnetic moments. In addition, Fe and Co also contribute orbital magnetic moments in the size of 0.21~0.22 $\mu_B$ /cell. For the B2 $Fe_8Co_8$ alloy, the calculated magnetic moments are 2.80 $\mu_B$ for Fe and 1.80 $\mu_B$ for Co, respectively. Compared with pure Fe, which has a magnetic moment of 2.2 $\mu_B$, the magnetic moments of Fe in alloys show significant enhancement. The magnetic moments of the Co atoms remain roughly constant

compared to those of pure Co atoms. As a result, the average magnetization of the B2 $Fe_8Co_8$ alloy is much larger than that of the constituent elements. This is in excellent agreement with the results from neutron diffraction experiments [102, 103], and the enhancement of the magnetic moments of Fe atoms can be explained in terms of the spin-flips of *d* electrons and most of the spin-flip in the Fe atoms occurs on the $t_{2g}$ electrons [104].

Table 4.2 Magnetocrystalline anisotropy energies ($E_{MCA}$) for the bcc-type FeCo alloys. The average magnetic moment per atom, which is proportional to the saturation magnetization, is also listed.

| Composition | Magnetic moment ($\mu_B$/atom) | $E_{MCA}$ ($\mu$eV/supercell) |
|---|---|---|
| $Fe_8Co_8$ (B2) | 2.21 | 0.00 |
| $Fe_9Co_7$ | 2.26 | 0.45 |
| $Fe_{10}Co_6$ | 2.28 | 0.13 |
| $Fe_{11}Co_5$ | 2.29 | 36.00 |
| $Fe_{12}Co_4$ | 2.29 | -196.00 |
| $Fe_{13}Co_3$ | 2.31 | 8.00 |
| $Fe_{14}Co_2$ | 2.28 | -0.85 |
| $Fe_{15}Co_1$ | 2.22 | 0.00 |

The calculated magnetocrystalline anisotropy energies of these alloys are also listed in Table 4.2. As a consequence of the preference of non-cubic structures, the magnetocrystalline anisotropy energies for $Fe_{11}Co_5$, $Fe_{12}Co_4$, and $Fe_{13}Co_3$ are extraordinarily large compared to those of other systems, which possess more symmetrical structures. For $Fe_8Co_8$ and $Fe_{15}Co_1$, the uniaxial magnetocrystalline

anisotropy energies are essentially zero since these two systems have cubic structures. In contrary, the ground-state non-cubic $Fe_{12}Co_4$, $Fe_{11}Co_5$ and $Fe_{13}Co_3$ have large magnetocrystalline anisotropy energies. For example, $Fe_{12}Co_4$ with $L6_0$ structure (see Fig. 4.2) has a magnetocrystalline anisotropy energy of value up to -196 μeV/cell. For $Fe_{11}Co_5$ and $Fe_{13}Co_3$ with non-cubic structures, the magnetocrystalline anisotropy energies are smaller than that of $Fe_{12}Co_4$ with $L6_0$ structure, but they are still relatively very large against those of other systems. It is worth noting that most of the bcc-type alloys under investigation have positive magnetocrystalline anisotropy energies, suggesting their easy axes of the magnetic anisotropy are parallel to *c* axis. However, the magnetocrystalline anisotropy of $Fe_{12}Co_4$ and $Fe_{14}Co_2$ is perpendicular to *c* axis, since they have negative magnetocrystalline anisotropy energies.

The results in Table 4.2 indicate that the magnetic anisotropy energy can be increased by several orders of magnitude even only two atoms in the supercell cell are placed differently (*c.f.*, the difference between the cubic and non-cubic geometries in Fig. 4.2). Clearly, sizeable magnetocrystalline anisotropy energy can be attained in small grains or thin films that comprise pure non-cubic phases of $Fe_{11}Co_5$, $Fe_{12}Co_4$, and $Fe_{13}Co_3$. In turn, this will facilitate inter-phase magnetic interaction and enhances the overall magnetization in exchange coupled nanocomposite systems. Therefore, they are good candidates for the soft magnetic materials in the exchange coupled nanocomposite magnetic systems.

In summary, the structural, electronic, and magnetic properties of FeCo alloys have been studied by first-principles calculations. It is found that only the bcc-type

alloys are stable. These alloys prefer chemically non-cubic geometries in a wide composition range. This produces appreciable uniaxial magnetocrystalline anisotropy, which facilitates inter-phase magnetic exchange coupling between soft phase and hard phase magnetic materials and enhances the overall magnetization in exchange coupled nanocomposite systems. Based on our calculations, it is found that non-cubic phases of $Fe_{11}Co_5$, $Fe_{12}Co_4$, and $Fe_{13}Co_3$ are good candidates for soft magnetic materials in exchange coupled nanocomposite magnets since they have large magnetization as well as large uniaxial magnetocrystalline anisotropy compared to other systems.

# CHAPTER 5

# INTERFACE EFFECTS

As mentioned previously, the idea of exchange-coupled nanocomposite magnets is to achieve high maximum energy product values by combining high saturation magnetization of a soft phase and large anisotropy of a hard phase. In this regard, the hard magnetic materials such as Sm-Co and the soft magnetic materials such as Fe-Co are particularly attractive because of their peculiar properties. Among the commonly used magnetic materials, for instance, $SmCo_5$ has the largest anisotropy energy ($1.7\times10^7$ $J/m^3$) with high Curie temperature, while Co, Fe and their alloys have very high Curie temperatures with large saturation magnetizations [10]. Indeed, high maximum energy product values have been reported [96] recently in exchange-coupled systems with SmCo5 as hard phase and Fe as soft phase. According to early models by Kneller and Hawig [1], an ideal hard/soft phase multilayer achieves maximum energy product at the optimum thickness of the soft phase which is equal to two domain wall thickness in the hard phase (it is about 7nm for $SmCo_5$). However, many recent experimental and theoretical studies show the important effect of the soft phase parameters and interface conditions [14-16, 97-98]. Thus it is important to understand the influence of these factors in the inter-phase exchange coupling, in order to achieve better energy products. In this chapter, I will focus on the effects of interface conditions and present our results

of dependence of exchange coupling on the interfacial conditions between the hard phase $SmCo_5$ and soft phase Co or CoFe alloys. By comparing the exchange coupling strengths in different interface conditions, and verified by calculating the site-to-site exchange parameters across the interface, we found that the inter-phase exchange coupling strength is indeed strongly dependent on the interface condition between the hard and soft phases [89].

## 5.1 Computational Details

The superlattice model is adopted to construct the structure for our simulation. Our original model is a supercell consists of one formula unit of $SmCo_5$ and 5 layers of Co stacking along $(10\bar{1}0)$ direction as shown in Figure 5.1 (a). $SmCo_5$ and *hcp* Co lattice constants have a mismatch of only 0.2% along this direction. Considering Fe doping in both soft phase and hard phase, we have constructed five other model systems, representing five different interface conditions. They are also shown in Figure 5.1: (b) $SmCo_5$/CoFe: Co atoms in one sublattice in soft phase replaced by Fe; (c) in $SmCo_5$/CoFe: Fe atoms diffused into and substituted a Co atom in the 1$^{st}$ layer of the hard phase; (d) in $SmCo_5$/CoFe: Fe atoms diffused into the 2$^{nd}$ layer of the hard phase; (e) Fe substitution in the 1$^{st}$ layer in hard phase, pure Co as soft phase; and (f) Fe substitution in the 2$^{nd}$ layer in the hard phase, pure Co as the soft phase. There are totally 18 atoms in a supercell in all these model systems.

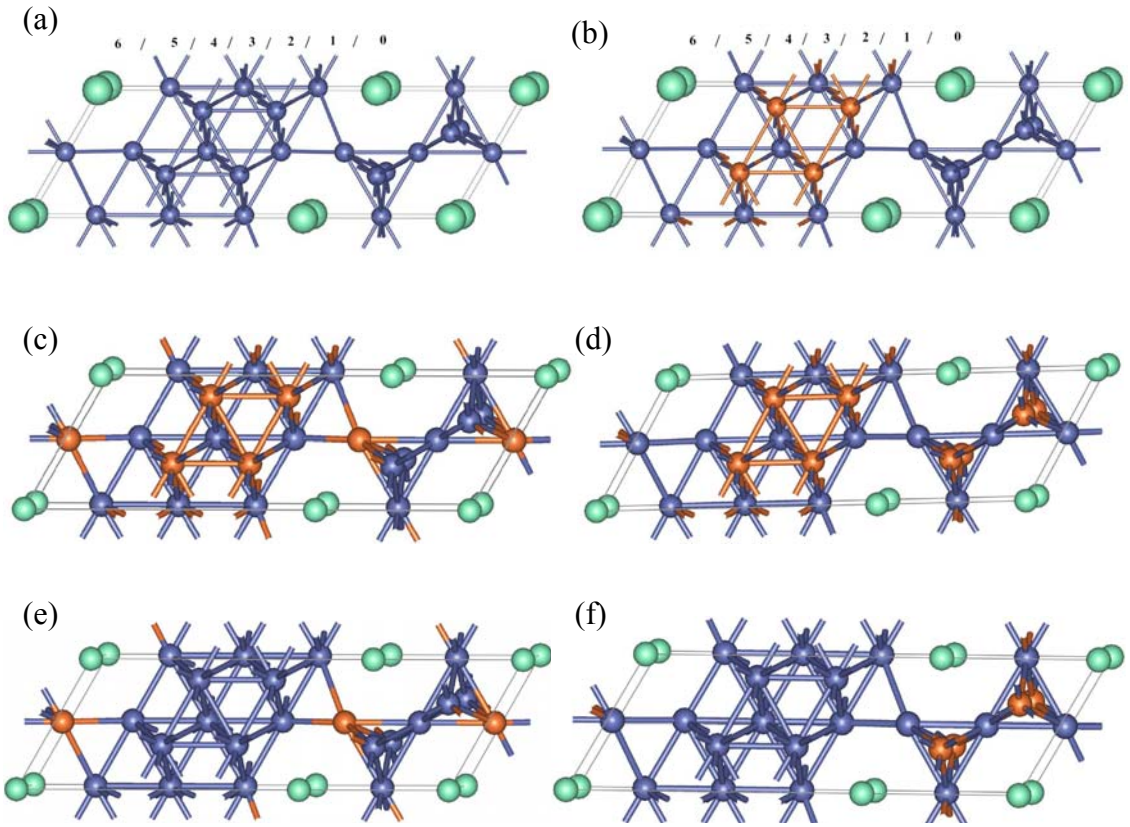


Figure 5.1 Atomic configurations of the two-phase model systems. Soft and hard phases are aligned along $(10\bar{1}0)$ direction. The green, blue and orange balls represent Sm, Co and Fe atoms, respectively. (a) The "original" system $SmCo_5$/Co: $SmCo_5$ as hard phase and pure hcp Co as soft phase; (b) $SmCo_5$/CoFe: Co atoms in one sublattice in soft phase replaced by Fe; (c) $SmCo_5$/CoFe: Fe atoms diffused into 1st layer hard phase; (d) $SmCo_5$/CoFe: Fe atoms diffused into 2nd layer hard phase; (e) Fe substitution in 1st layer in hard phase, pure Co as soft phase; and (f) Fe substitution in 2nd layer in hard phase, pure Co as soft phase. The label on top of each panel indicates the planes parallel to the interface. The periodic boundary condition has been used in the graph.

In the study we consider the nanocomposite exchange-spring multilayer with the sizes of the hard and soft layer smaller than the thickness of a usual domain wall, so that the exchange-coupling between the two phases will be in effect. A single domain case is considered for both the hard and the soft phase in the present modeling interface. The

self-consistent spin-polarized electronic structure calculations were performed using both the Vienna *ab initio* simulation package (VASP) [60, 75-78] and the linear-muffin-tin-orbital (LMTO) method [64, 72] in atomic sphere approximation and in near orthogonal representation generalized to treat noncollinear magnetic configurations [90].

In the VASP calculations, which are performed to optimize the structure of the system, the projector augmented wave (PAW) method [60, 70-71] implemented in VASP was used describe the electron-ion interactions. The PAW potentials for Sm, Co and Fe were generated from the atomic configuration of [Xe]$5s^2 5p^6 5d^1 6s^2$, [Ar]$3d^8 4s^1$ and [Ar]$3d^7 4s^1$, respectively. Using these PAW potentials were justified by reproducing excellently the lattice constants of crystal $SmCo_5$, Co and Fe. The lattice constants for $SmCo_5$ are a=4.970 Å, c/a=0.797 from our calculations. The calculated lattice constants for Fe and Co are reported in Chapter 4. They are all in good agreement with experimental values. Integrations in the reciprocal space were evaluated as summations over an 8×8×8 *k*-point set in the irreducible first Brillouin zone generated according to the Γ centered Monkhorst-Pack scheme [45]. The plane wave energy cutoff was set at 335 eV (24.6 Ry) to ensure the convergence of the calculations. Because of the two-phase structure, the coordinates of atoms as well as the alignment and spacing between the hard and soft phases are all needed to be optimized. These are done according to the energy minimization procedures guided by atomic forces. The optimized spacing between the soft and the hard phases is 2.5 Å according to our calculations. As an example, Figure 5.2 shows the structures of system (a) before and after relaxations.

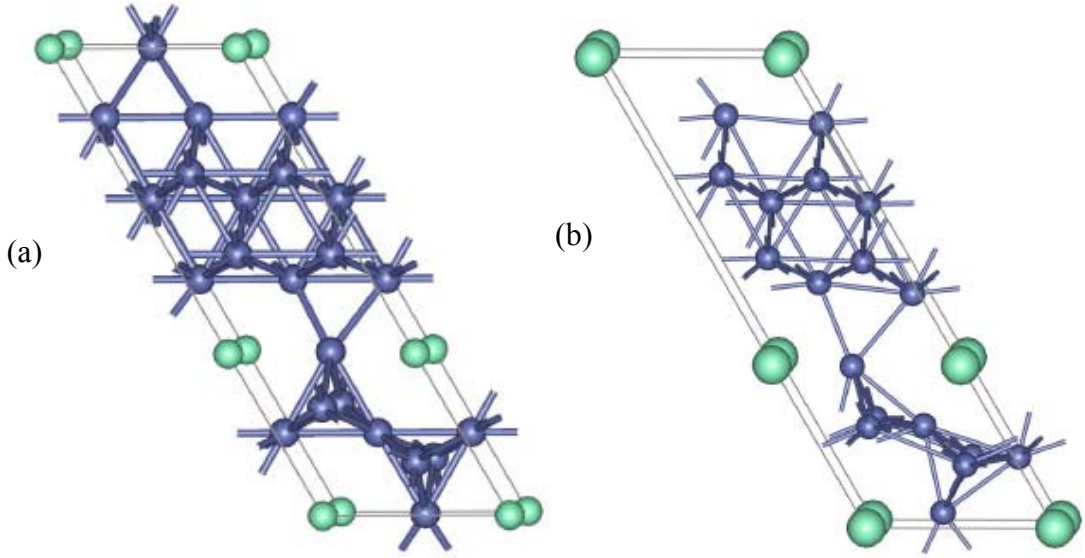


Figure 5.2 Comparisons of the structures of $SmCo_5$/Co system (a) before relaxation; and (b) after relaxation. The green and blue balls represent Sm and Co atoms, respectively.

After the optimized structure was obtained, the structural parameters are used as inputs to do LMTO magnetic ground state and noncollinear calculations in the LMTO package. Our model mimics a domain wall which forms in the demagnetization process. In these calculations, the ratio of the Wigner-Seitz radii of Sm, Fe and Co in the composite systems was set to be 1.4: 1.04: 1.00, as the ratio of their corresponding atomic radii. An 8×3×10 *k*-point set were used in the 1$^{st}$ Brillouin zone. The number of *k*-points chosen was assured by monitoring the convergence of electronic and magnetic properties of the systems. The self-consistence was assumed when the root-mean-square differences between the input and output charges and spin densities are less than $1.0\times10^{-8}$ *e*/(a.u.)$^3$. In the noncollinear calculations, which is adopted to simulate the demagnetizing process of the magnetic system, the directions of the magnetic moments of the atoms in the hard phase were fixed to the easy magnetization axis direction (*c*

direction in our case, $\theta$=0°) as shown in Figure 5.3. The magnetic moments of the atoms of the middle layer in the soft phase are also fixed at a given angle $\theta$ relative to the direction of the magnetic moments of the hard phase, but the magnetic moments of other atoms in the soft phase are free to relax. Upon the convergence of the calculation is reached, the total energy is obtained for each initial angle $\theta$. It is worth noting that by setting the magnetic moments in this way, we do not take account of the effects of 4*f* electrons in Sm atoms on the exchange coupling. The very localized 4*f* electrons are still a challenge to handle within the framework of local density approximation (LDA) and generalized gradient approximation (GGA). The 4*f* electrons of Sm are frozen in the core potential in our LMTO calculations.

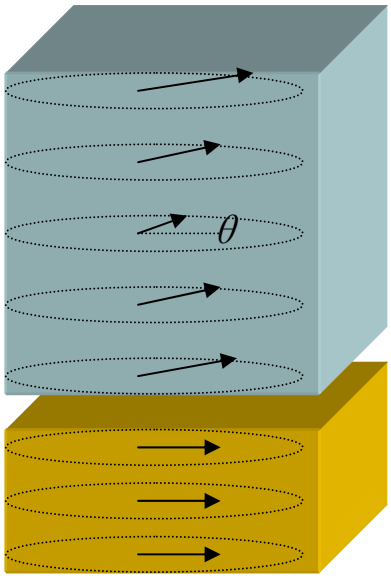


Figure 5.3 A schematic view of noncollinear magnetic orderings in the two-phase systems. The arrows represent the directions of magnetic moments of the atoms in each layer. $\theta$ is the angle between the directions of magnetic moments of the atoms in the hard phase and in the middle layer of the soft phase, which are fixed.

Besides from the noncollinear magnetic structure calculations, the exchange coupling strength is also described complementarily in our study by calculating the site-to-site exchange parameters across interface using a perturbative method. The expression for the site-to-site exchange parameters $J_{ij}$ in a Heisenberg Hamiltonian is given in Ref. 91 by perturbation theory:

$$J_{ij} = \frac{1}{4\pi} \sum_{LL'} \mathrm{Im} \int_{-\infty}^{\varepsilon_F} d\varepsilon \Delta_l^i(\varepsilon) T_{LL'}^{ij\uparrow}(\varepsilon) \Delta_{l'}^j(\varepsilon) T_{LL'}^{ij\downarrow}(\varepsilon). \quad (5.1)$$

Here $T_{LL'}^{ij\sigma}(\varepsilon)$ is the scattering path operator in the site (i, j) representation for different spin projections ($\sigma = \uparrow, \downarrow$), and $\Delta_l^i(\varepsilon) = t_{i\uparrow}^{-1} - t_{i\downarrow}^{-1}$ is the difference of the inverse single-site scattering matrices. Since $J_{ij}$ decreases fairly rapidly as a function of the distance, the calculation is limited to the few nearest neighboring pairs only.

## 5.2 The Original $SmCo_5$/Co System

We first focus on the original model systems (a), $SmCo_5$/Co where $SmCo_5$ serves as hard phase and pure *hcp* Co serves as soft phase. Upon the convergence of the calculations is reached, the total energy is obtained for each given angle $\theta$. The range of the initial finite angle $\theta$ in our calculation is from $0^\circ$ to $67.5^\circ$. The total energy difference for the system, $\delta E(\theta) = E(\theta) - E(\theta = 0°)$ , as a function of the turning angle $\theta$ as well as its fitting to to a quadratic curve are shown in Figure 5.4. We find that $\delta E(\theta)$ can be perfectly fitted as a quadratic function of $\theta$, manifesting the spring behavior and the exchange coupling between the soft and hard phases in this system. If

there is no exchange coupling between the soft and hard phases in this system, $\delta E(\theta)$ vs. $\theta$ will not be well fitted with a quadratic function and the curve will be as smooth as shown in Figure 5.4.

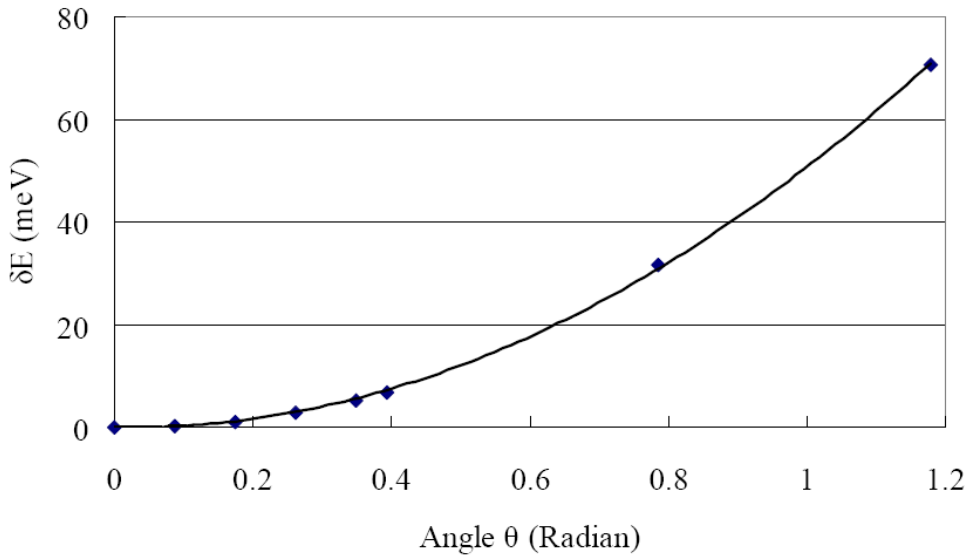


Figure 5.4 The calculated total energy differences, $\delta E(\theta) = E(\theta) - E(\theta = 0^{\circ})$ (the marks) and their fitting to a quadratic curve for systems (a) as illustrated in Fig 5.1.

The layer resolved angle of rotations of atomic moment across the soft phase Co with $\theta$ set at 20° is shown in Figure 5.5. With $\theta$ set with other finite angles, we observe similar curves (not shown). Clearly, this also demonstrates that the hard phase and soft phase are exchange coupled. Because of this exchange coupling, the closer the soft phase layers to the hard phase, the closer the directions of their magnetic moments orient to that of the hard phase due to the exchange coupling between the two phases. If no exchange coupling exists between the soft and hard phases, the atomic magnetic moments that can freely relax in the soft phase would orient to the direction of the

magnetic moments of the middle layer atoms in the soft phase, which is fixed at 20° in this case.

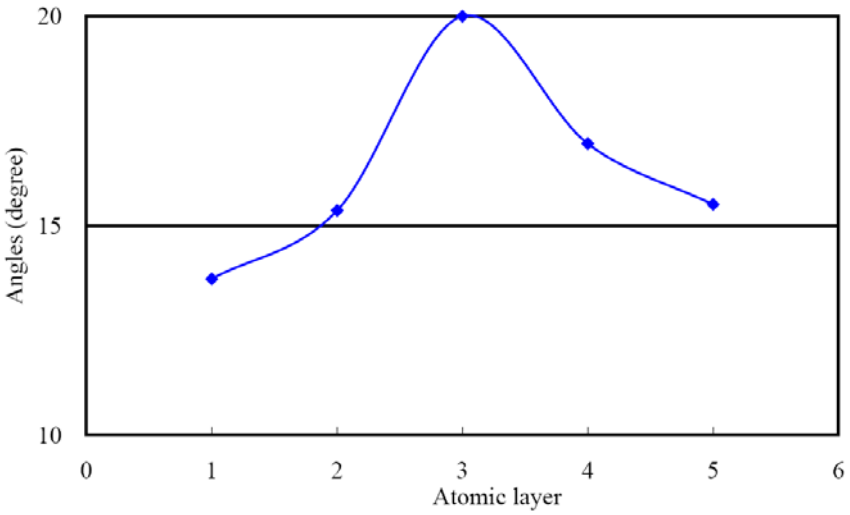


Figure 5.5 The angle distributions of magnetic moments for the soft phase atomic layers parallel to the interface plane (refer to Fig. 5.1(a)). Layer 0 and layer 6 are the fixed hard phase layers in the superlattice model. Layer 3 is the middle layer of the soft phase, whose atomic magnetic moments are turned at a fixed value ($20^o$ here) away from those in the hard phase layers. All the atomic magnetic moment orientation in layers 1, 2, 4, and 5 are obtained self-consistently.

## 5.3 Comparison between $SmCo_5$/Co and $SmCo_5$/CoFe

We now discuss the effects by introducing Fe into the soft phase as illustrated in model system (b), $SmCo_5$/CoFe where the hard phase is still $SmCo_5$ but Co atoms in one *hcp* sublattice in soft phase replaced by Fe atoms. Again the total energy is obtained for each given angle θ upon the convergence of the calculations. The total energy difference for the system, $\delta E(\theta) = E(\theta) - E(\theta = 0°)$ , as a function of the turning angle θ is shown in Figure 5.6. We find that $\delta E(\theta)$ also behaves as a quadratic function of θ, indicating the soft and hard phases in this system are also exchange coupled. We

compare results in the case of soft phase made of pure hcp Co (model system (a)) and the Fe-doped Co soft phase (model system (b)). The iron doping is expected to strengthen the exchange coupling because FeCo alloy have stronger exchange than a pure Co phase, and, at the same time, an increased magnetization. Furthermore, an iron doping can produce more gradual variation of anisotropy across interface.

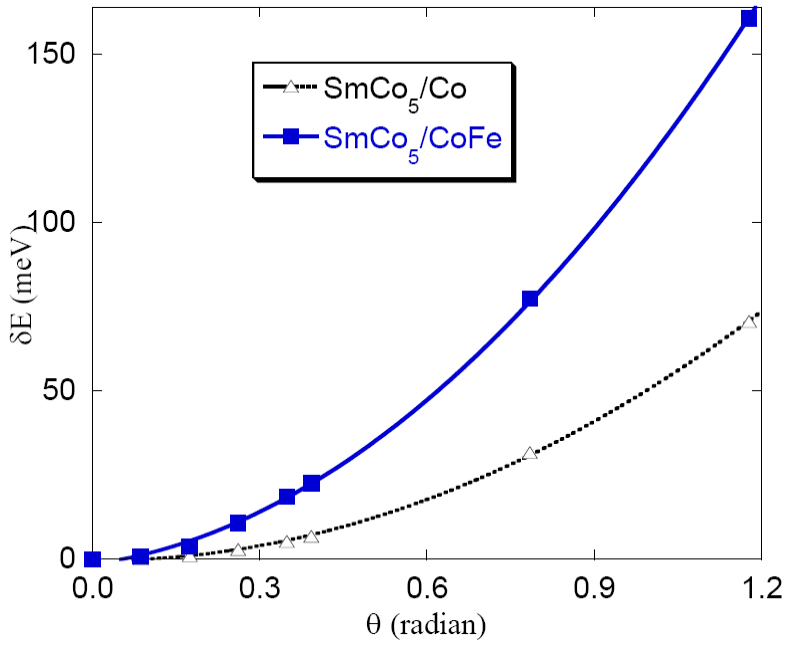


Figure 5.6 The calculated total energy differences, $\delta E(\theta) = E(\theta) - E(\theta = 0)$ (the marks) and their fitting to a quadratic curve for systems (a) and (b) as depicted in Fig 5.1.

The structure of the interface shows a substantial change in the local coordination of Co atoms when going from $SmCo_5$ to hcp Co phase. Co atoms near the interface lack some of their nearest neighbors as can be seen from Fig. 5.1. Thus, we can expect that the exchange coupling near the interface should be different from the one in either phase. Because of the reduction of number of nearest neighbors across the

interface, the interface exchange coupling is reduced. It can be seen from the variation of the layer resolved angle of rotations of atomic moment across the soft phase as shown in Figure 5.7. The middle-layer angle is fixed at $\theta = 15°$ in this example but the phenomenon is similar with other fixed angles (see Fig 5.8). Two other layers have their relaxed angles at 10 and 11.5 degrees which is indication that coupling is the strongest between first and second layer, but weakest across the interface. In the system with uniform exchange coupling these angles are expected to be close to 5 and 10 degrees, respectively. Thus, the exchange coupling oscillates in the soft phase as function of distance from the interface. Using one dimensional Heisenberg model we fit the inter-phase exchange coupling parameter per cross-section of the unit cell to be about 16 meV and 25 meV in case of *hcp* Co, and FeCo alloy, respectively. The exchange between Co plane at the interface and next layer of Co in the soft phase is order of magnitude larger. Such large difference is due to a large increase in number of bonds across planes (by factor of 6) and the increase in the pair exchange parameters (by factor of 1.5).

We find that the effect of doping on the exchange coupling is significant. Fig. 5.1(b) illustrates our model where Co atoms in the hcp-Co film are replaced by Fe atoms in the second layer. By introducing Fe atom in this extreme model, Fe atoms were counted as 40% in the soft phase. In this system, as mentioned, $\delta E(\theta)$ is also a quadratic function of θ (Fig. 5.6). However, the curve of this system is much steeper than that of pure Co, indicating that the exchange coupling in system with Fe-doped soft phase is stronger than the exchange coupling in system with pure Co as soft phase.

According to micromagnetics, the exchange energy density is equal to exchange stiffness constant multiplied by a function of the gradient of magnetization in the materials. If we assume the same function of the gradient for both interface models, since we have the same lattice structure and the same angle rotated at the central layer in the soft phase side, then the energy ratio should equal to the ratio of their exchange stiffness constant. From Fig.5.6, this ratio is evaluated between 2.2 (for larger θ's) to 3.6 (for smaller θ's). Therefore, the enhancement to the exchange-coupling for the system (b) with FeCo alloy as soft phase is a factor of two. Comparing the layer resolved relaxed angles of atomic magnetic moments for both systems, we observe a smaller angle of rotation in the interface layer for system (b) (Figs 5.7 and 5.8, solid line). This also indicates that the inter-phase exchange coupling between the hard and soft phases is stronger in system (b). Because of this stronger exchange coupling interaction between the soft and hard phases, the directions of the magnetic moments of soft phase atoms orient closer to those of the hard phase, which is fixed to zero degree. Therefore, comparing to system (a), the atomic magnetic moments in the soft phase of system (b) have smaller angles of rotation.

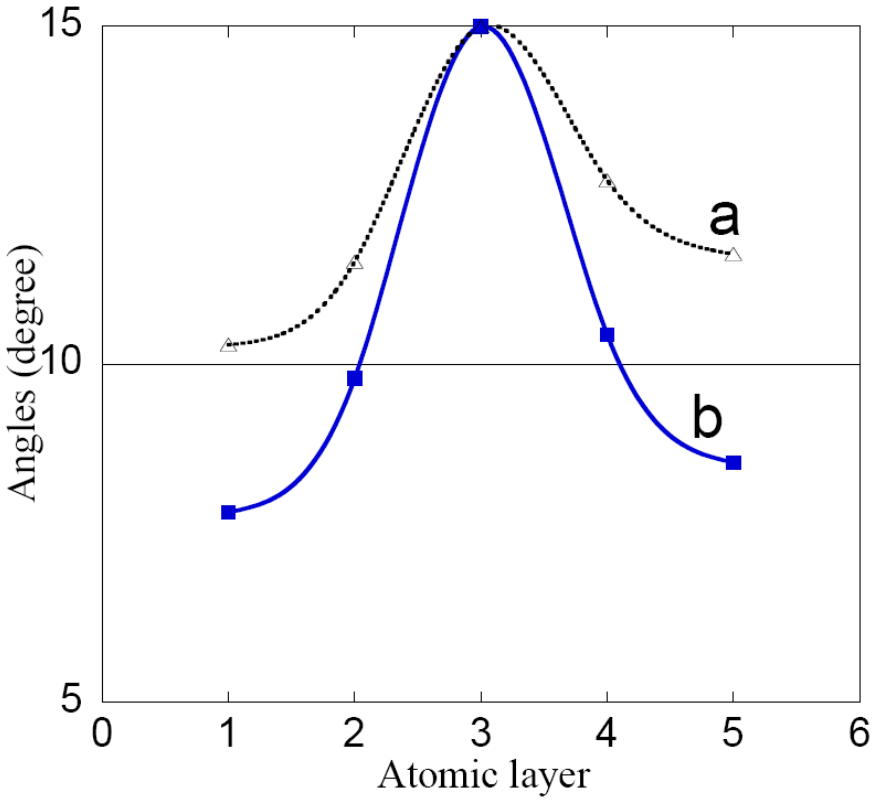


Figure 5.7 The angle distributions for the soft phase atomic layers parallel to the interface plane (refer to Figs. 5.1(a) and 5.1(b)). Layer 0 and layer 6 are the fixed hard phase layers in the superlattice model. Layer 3 is the middle layer of the soft phase, whose atomic magnetic moments are turned at a fixed value ($15^{o}$ here) away from those in the hard phase layers. All the atomic magnetic moment orientation in layers 1, 2, 4, and 5 are obtained self-consistently.

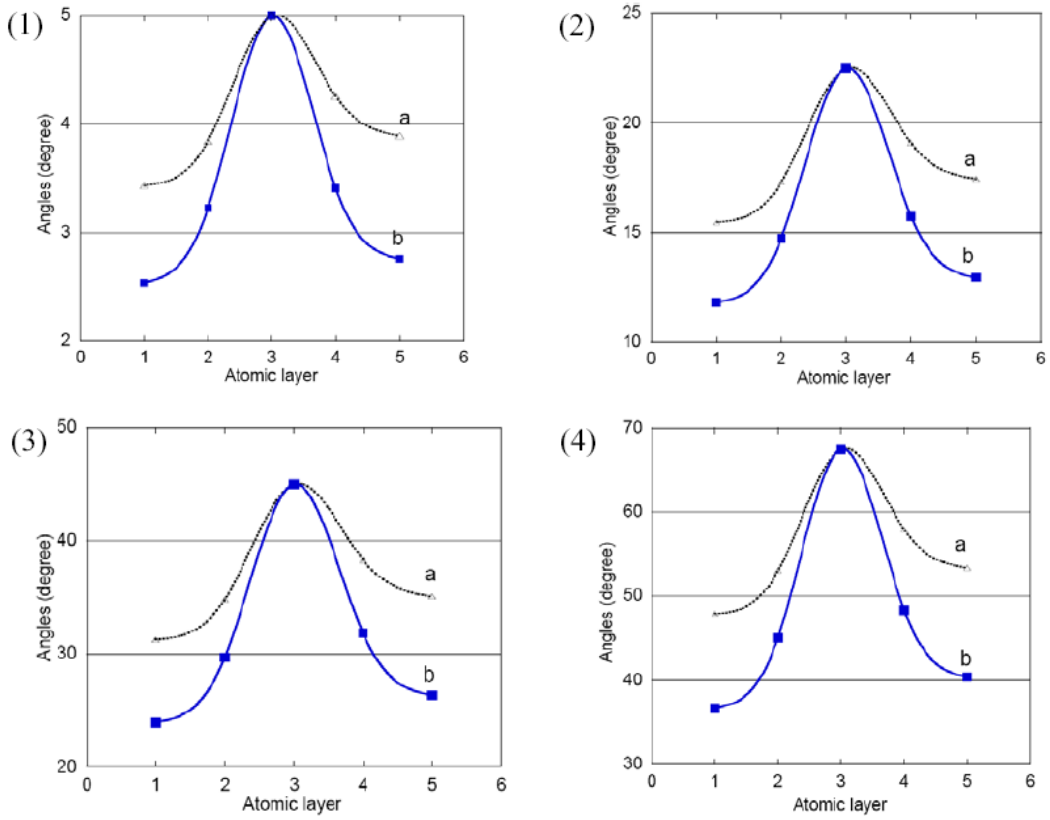


Figure 5.8 The angle distributions for the soft phase atomic layers parallel to the interface plane (refer to Figs. 5.1(a) and 5.1(b)). Layer 0 and layer 6 are the fixed hard phase layers in the superlattice model. Layer 3 is the middle layer of the soft phase, whose atomic magnetic moments are turned at a fixed value (1)5$^{o}$; (2)22.5$^{o}$; (3)45$^{o}$; and (4)67.5$^{o}$ away from those in the hard phase layers. All the atomic magnetic moment orientation in layers 1, 2, 4, and 5 are obtained self-consistently.

The calculated site-to-site exchange parameters $J_{ij}$ as given by Eq. (5.1), averaged over the atomic pairs between the layers for model systems (a) and (b) are listed in Table 5.1. The minus sign of $J_{ij}$ ensures that the systems are in the ferromagnetic state. It is clear that the site-to-site exchange parameters of the interface atomic pairs in system (b) are larger (absolute values) than those of the corresponding pairs in system (a). This also supports that the inter-phase exchange coupling in system

(b) is stronger than that in system (a), in agreement with the present noncollinear magnetic ordering simulation as discussed above.

Table 5.1 The atomic site-to-site exchange parameters averaged within the layers at the interface for systems (a) and (b) as shown in Fig 5.1.

| Interface models | Pair of layers (*cf*. Fig.5.1) | Averaged $J_{ij}$ (meV) |
|---|---|---|
| (a) | 0 - 1 | -3.23 |
| | 6 - 5 | -14.30 |
| (b) | 0 - 1 | -34.30 |
| | 6 - 5 | -28.90 |

## 5.4 Comparison among Systems with the Same Hard Phase

As discussed in last section, when the hard phase is pure $SmCo_5$, the introduction of Fe atoms to the soft phase will enhance the exchange coupling between the hard and soft phases. Besides this pair of systems, (a) and (b), which have the same hard phase pure $SmCo_5$, there are two other pairs of systems with the same hard phase materials, i.e., systems (c) and (e), and systems (d) and (f).

In systems (c) and (e), the same hard phase is $SmCo_5$ with Co atom in first layer from the interface substituted by Fe atom. The soft phase material in system (c) is CoFe, while in system (e), the soft phase materials is pure Co. Figure 5.9 shows $\delta E(\theta)$ vs. $\theta$ for these two systems. Obviously the soft phase and the hard phase are exchange coupled in both systems, as evidenced by the well fitted curves with quadratic functions. Comparing the two curves, we can see that the exchange coupling in system (c), in

which the soft phase is CoFe, is stronger than that in system (e), in which the soft phase is pure Co, since the curve for system (c) is steeper than the curve for system (e).

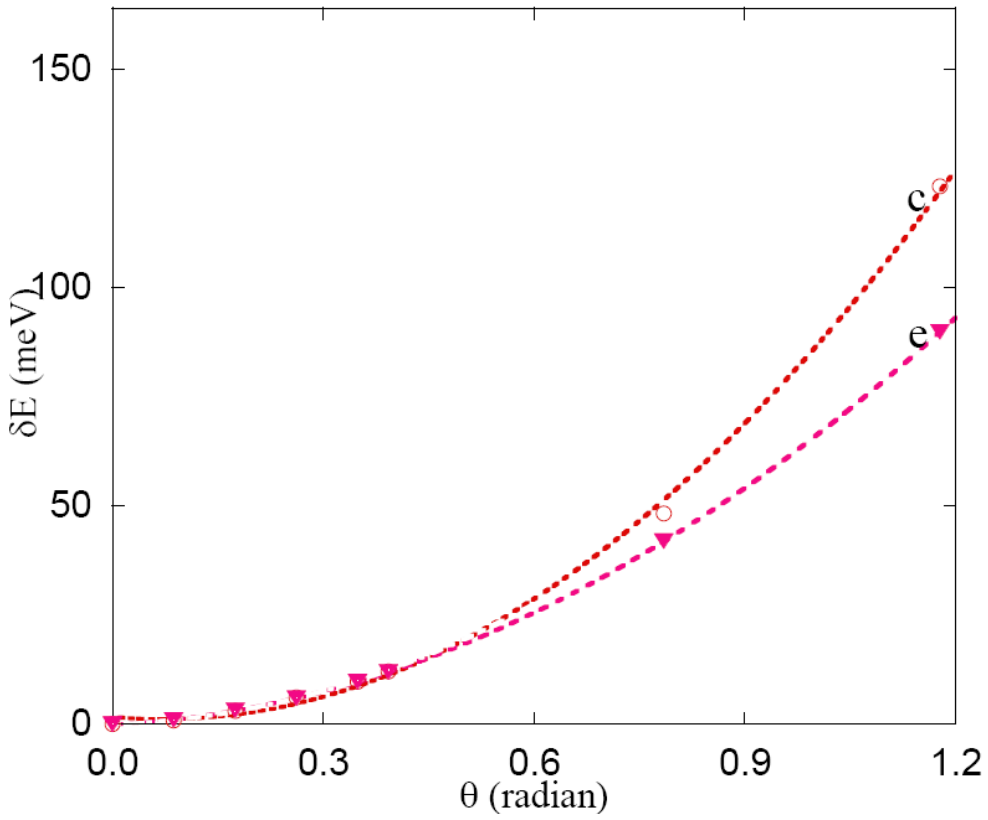


Figure 5.9 The calculated total energy differences, $\delta E(\theta) = E(\theta) - E(\theta = 0)$ (the marks) and their fittings to a quadratic curve for systems (c) and (e) as depicted in Fig 5.1. These two systems have the same hard phase material but different soft phase materials.

Systems (d) and (f) also have the same hard phase, which is $SmCo_5$ with Co atom on second layer from the interface substituted by Fe atom. The difference between them is their soft phase materials. In system (d), the soft phase material is CoFe, whereas the soft phase in system (f) is pure Co. As shown in Figure 5.10, $\delta E(\theta)$ can be fitted very well as a quadratic function of $\theta$ for both systems. This means that the exchange coupling interactions between the soft phase and the hard phase are strong in

these systems. Because the curve for system (d) is steeper than that for system (f), the exchange coupling between the soft and hard phases is stronger in system (d).

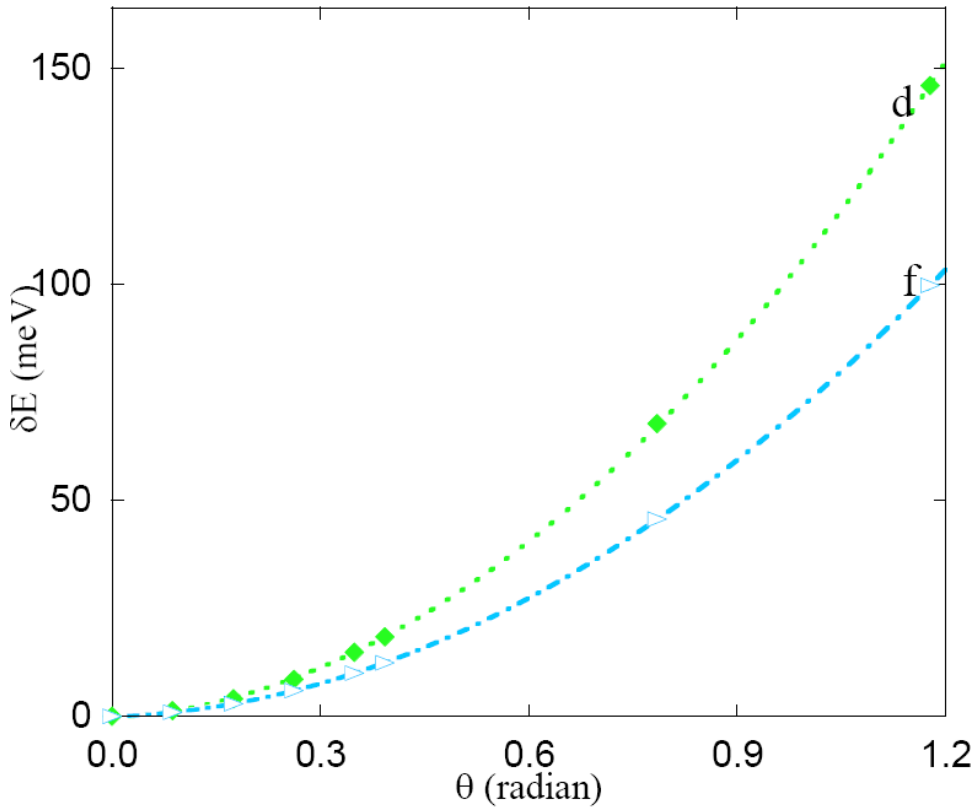


Figure 5.10 The calculated total energy differences, $\delta E(\theta) = E(\theta) - E(\theta = 0)$ (the marks) and their fittings to a quadratic curve for systems (d) and (f) as depicted in Fig 5.1. These two systems have the same hard phase material but different soft phase materials.

By comparing the three pairs of systems, (a) and (b), (c) and (e), and (d) and (f), where the hard phase is the same for each pair, we can conclude that with the same hard phase, doping of Fe in soft phase will improve the exchange coupling between the hard phase and the soft phase. As discussed above, the three systems with CoFe as soft phase have steeper $\delta E(\theta)$ vs. $\theta$ curves than their corresponding systems with the same hard phase material but with pure Co as soft phase.

## 5.5 Comparison among Systems with the Same Soft Phase

In the six systems as illustrated in Fig. 5.1, systems (a), (e) and (f) have the same soft phase materials, which is pure Co. In system (a), the hard phase is pure $SmCo_5$. In systems (e) and (f), Co atoms of hard phase in first and second layer from the interface are substituted by Fe atoms, respectively. As shown in Figure 5.11, with the pure Co as soft phase, both Fe doping to the first and second layer of the hard phase will strengthen the exchange coupling since the two corresponding curves are above the curve for system (a). In addition, system (f), in which Fe is in the second layer of the hard phase, has a stronger exchange coupling than that of system (e), where Fe is in the first layer of the hard phase.

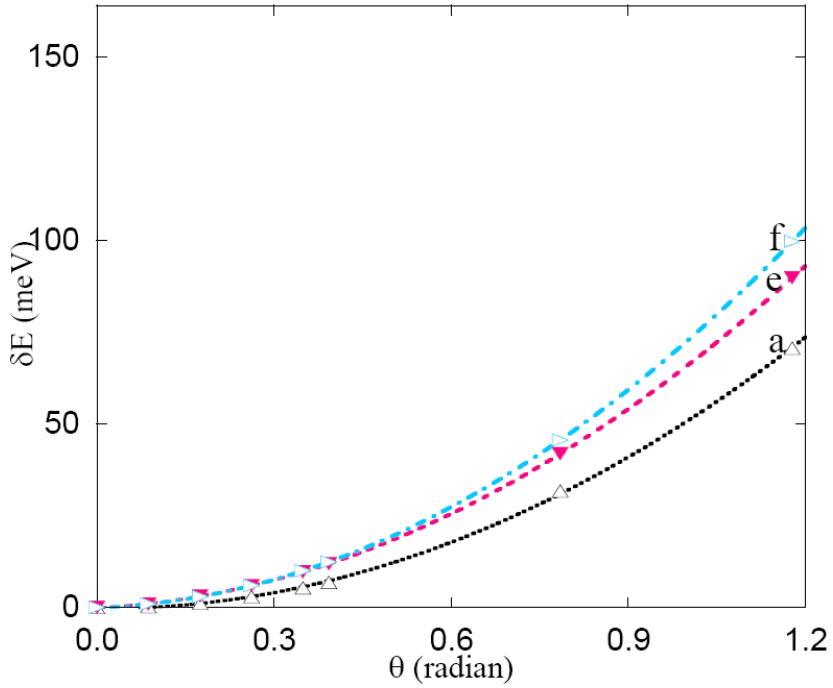


Figure 5.11 The calculated total energy differences, $\delta E(\theta) = E(\theta) - E(\theta = 0)$ (the marks) and their fitting to a quadratic curve for systems (a), (e) and (f) as depicted in Fig 5.1. These three systems have the same soft phase material but different hard phase materials.

Systems (b), (c) and (d) also have the same soft phase material CoFe. The difference between them is also on their hard phase materials. The hard phase in system (b) is pure $SmCo_5$. Co atoms of hard phase in first and second layer from the interface are substituted by Fe atoms in systems (c) and (d), respectively. Figure 5.12 shows $\delta E(\theta)$ vs. $\theta$ for these three systems. Unlike the effects we just discussed among systems (a), (e) and (f), for CoFe as the soft phase material, an Fe in the second layer and in the first layer in the hard phase causes degradation of the exchange coupling, showing by the curves for systems (c) and (d) lying right below the curve for system (b). Comparing the curves for system (c) and (d), it is found the curve for system (d) is steeper than that for system (c). This means that the degradation of the exchange coupling is less in system (d), where Fe substitution is in second layer of the hard phase, than in system (c), where Fe substitution is in first layer of the hard phase.

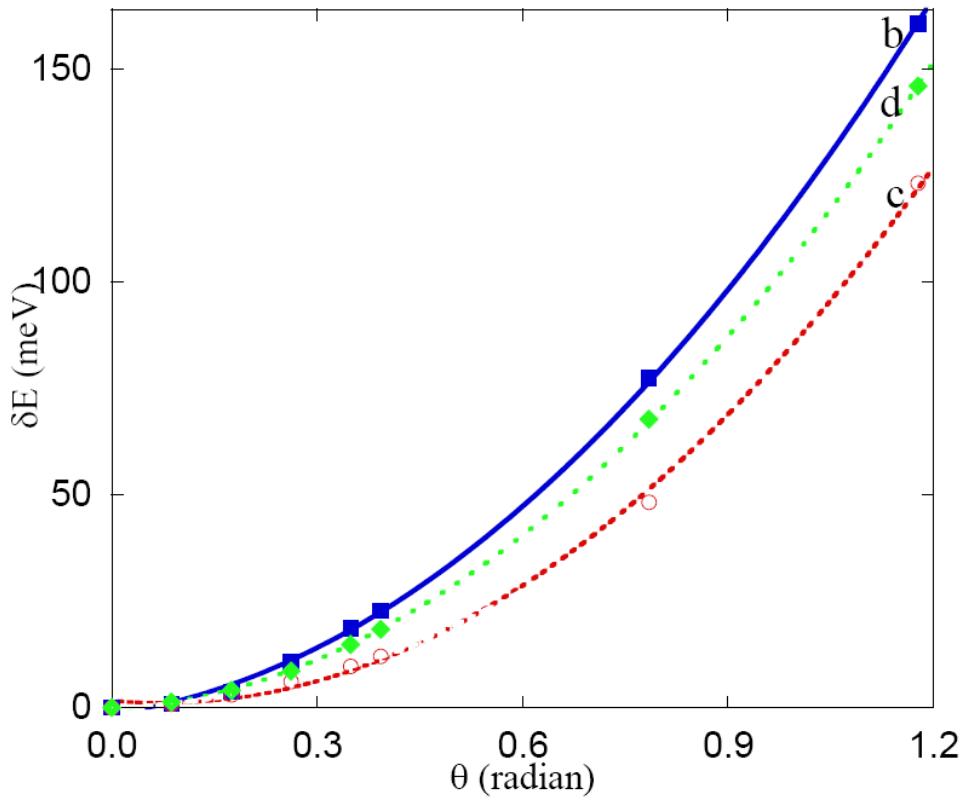


Figure 5.12 The calculated total energy differences, $\delta E(\theta) = E(\theta) - E(\theta = 0)$ (the marks) and their fitting to a quadratic curve for systems (b), (c) and (d) as depicted in Fig 5.1. These three systems have the same soft phase material but different hard phase materials.

Overall, as shown in Figure 5.13, in which we plotted δE(θ) vs θ curves of all the systems from the noncollinear magnetic ordering calculations, the hard phase and the soft phase in all these systems are exchange coupled, as evidenced by the smooth fittings by quadratic functions. It is clear that the curve of $SmCo_5$/CoFe model (system (b)) serves as upper bound while the $SmCo_5$/Co model (system (a)) serves as the lower bound. Therefore, among all the systems we considered, system (b), in which $SmCo_5$ is the hard phase and Fe doped Co is the soft phase, has the strongest exchange coupling. And system (a), in which $SmCo_5$ is the hard phase and pure Co is the soft phase, has the

weakest exchange coupling. The strengths of inter-phase exchange coupling in other systems are between those of these two systems. The order of the strengths of exchange coupling in all these systems, from strong to weak, is (b), (d), (c), (f), (e) and (a).

Table 5.2 The atomic site-to-site exchange parameters averaged within the layers at the interface for all the systems as shown in Fig 5.1.

| Interface models | Pair of layers (*cf*. Fig.5.1) | Averaged $J_{ij}$ (meV) |
|---|---|---|
| (a) | 0 - 1 | -3.23 |
| | 6 - 5 | -14.30 |
| (b) | 0 - 1 | -34.30 |
| | 6 - 5 | -28.90 |
| (c) | 0 - 1 | -24.01 |
| | 6 - 5 | -21.30 |
| (d) | 0 - 1 | -32.68 |
| | 6 - 5 | -27.93 |
| (e) | 0 - 1 | -15.09 |
| | 6 - 5 | -18.72 |
| (f) | 0 - 1 | -17.27 |
| | 6 - 5 | -19.58 |

The calculated site-to-site exchange parameters $J_{ij}$ averaged over the atomic pairs between the layers for all the model systems are listed in Table 5.2, with the data for systems (a) and (b) shown again for comparison purpose. As mentioned earlier, the minus sign of $J_{ij}$ indicates that the systems are in the ferromagnetic state. Obviously, the

site-to-site exchange parameters of the interface atomic pairs in these systems have the order (in absolute values) of (b), (d), (c), (f), (e) and (a). This is in agreement with the conclusion from the noncollinear magnetic ordering simulations.

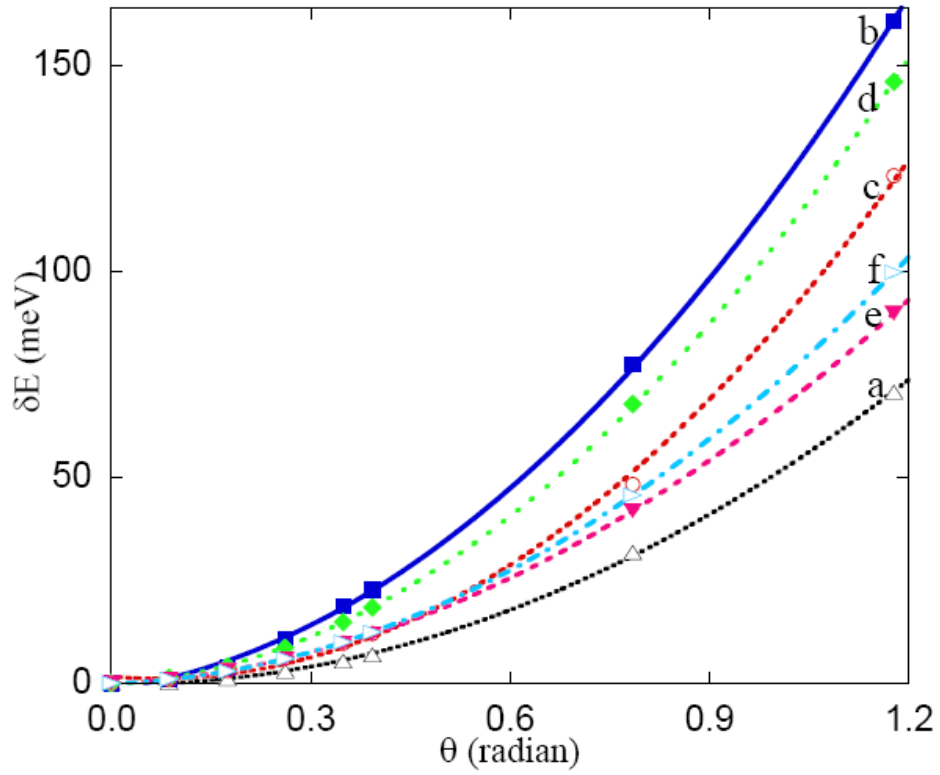


Figure 5.13 The calculated total energy differences, $\delta E(\theta) = E(\theta) - E(\theta = 0)$ (the marks), together with their fittings for the systems illustrated in Fig 5.1. It is clear that the curve for system (b) serves as the upper bound and the curve for system (a) is the lower bound among all the systems.

In summary, we have performed first-principles calculations to study the inter-phase exchange coupling in hard/soft SmCo5/Co(Fe) multilayer model systems. We have considered six different models, representing six different interfacial conditions. Using both the noncollinear magnetic ordering simulation and the calculation of the

site-to-site exchange parameters across the interface, we found that the inter-phase exchange coupling is strongly dependent on the variation of the atomic composition across the interface. It is found in our study that the exchange coupling in $SmCo_5$/Co is enhanced by introducing Fe in the soft phase. However, the introduction of Fe atom into the hard phase, $SmCo_5$, will have different effects, depending on the soft phase composition. For a pure hcp Co as soft phase, it enhances the exchange coupling. But for CoFe as soft phase, it leads to the degradation of the exchange coupling. Nevertheless, in both soft phase cases, the system with Fe in the second layer of the hard phase has a stronger exchange coupling than that of the system with Fe in the first layer of the hard phase. The findings were further confirmed by the calculated site-to-site exchange parameters across the interface.

# CHAPTER 6

# FeCo NANOWIRES

Ferromagnetic nanowires have been widely investigated for decades for magnetic applications [105-110] because of their inherent high shape anisotropy, which provides a high intrinsic coercivity to the material. Among numerous magnetic nanowires, FeCo nanowires provide a potential way to produce high-performance nanocomposite permanent magnets due to their high Curie temperature, large saturation magnetization and inherent large shape anisotropy and appreciable magnetocrystalline anisotropy. In this chapter, I present the results of our first-principles study of FeCo nanowires. We investigated the geometric structure, stability and magnetic properties of these nanowires and conclude that the FeCo nanowires under our investigation indeed could be used as potential permanent magnets with high maximum energy product or as soft phase component in an anisotropic assembled nanocomposite system [92].

## 6.1 Structures of Nanowires

Nanowires made of pure B2 FeCo alloy in (001) direction are considered. In the calculations, we used two supercells as shown in Figure 6.1: one consists of 2×2×1 B2 FeCo unit cell (Fig 6.1(a)) plus vacuum and the other one consists of 3×3×1 B2 FeCo unit cell (Fig 6.1(b)) plus vacuum. The vacuum is between wires in a periodic boundary

condition, in x- and y-directions in the calculations. There are 13 and 25 atoms in total in the two supercells respectively. Considering that the positions of Fe and Co atoms can be exchanged, we have initially 4 structures, namely $Fe_9Co_4$, $Fe_4Co_9$, $Fe_{16}Co_9$ and $Fe_9Co_{16}$. In addition, we have used pure *bcc* Fe nanowires in the same modeling arrangement, denoted by $Fe_{13}$ and $Fe_{25}$, respectively, as reference systems.

(a) (b)

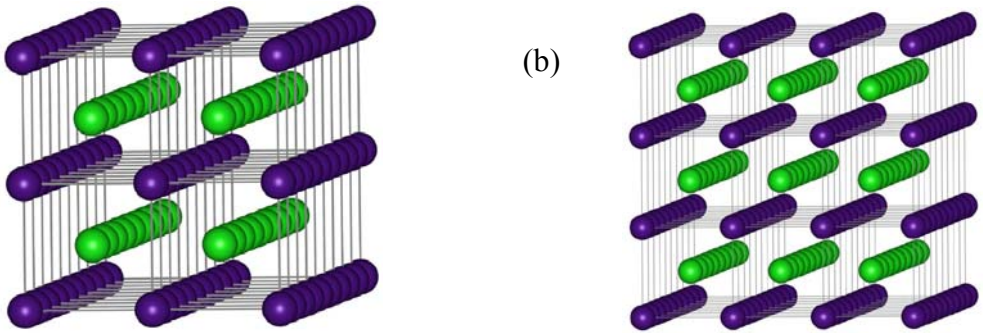

Figure 6.1 Geometric structures before relaxation: (a) $Fe_9Co_4/Fe_4Co_9$; (b) $Fe_{16}Co_9/Fe_9Co_{16}$. If all the atoms are Fe, we will have our reference systems, bcc Fe nanowires.

The structures of Fe-Co nanowires were optimized by PAW method [60, 70-71] implemented in VASP [60, 75-78]. We found that compared to the bulk B2 FeCo alloy (a=b=c=2.83 Å), the lattice constants of these nanowires all shrink slightly along the wire direction as shown in Table 6.1. Specifically, the lattice constants along the wire direction (i.e., lattice c) are 2.64 Å, 2.66 Å, 2.73 Å, and 2.74 Å for $Fe_9Co_4$, $Fe_4Co_9$, $Fe_{16}Co_9$ and $Fe_9Co_{16}$, respectively. For the pure Fe nanowires, the lattice constants along the wire direction also shrink slightly. The optimized lattice constants along the wire direction are 2.74 Å and 2.78 Å for $Fe_{13}$ and $Fe_{25}$, respectively, while c=2.83 Å in

bulk *bcc* Fe metal. We also found that after full relaxations the cross sections of these nanowires become slightly rounder, whereas the cross sections before relaxations are all square. Figure 6.2 shows an example of the cross sections of $Co_4Fe_9$ before and after relaxations.

Table 6.1 Lattice constants along the wire direction of the FeCo nanowires. For comparison, the lattice constants of bulk B2 FeCo alloy and bcc Fe are also listed.

| System | Length of c (Å) |
|---|---|
| $Fe_4Co_9$ | 2.66 |
| $Fe_9Co_4$ | 2.64 |
| $Fe_{13}$ | 2.73 |
| $Fe_9Co_{16}$ | 2.74 |
| $Fe_{16}Co_9$ | 2.73 |
| $Fe_{25}$ | 2.78 |
| Bulk B2 FeCo | 2.83 |
| Bulk bcc Fe | 2.83 |

After the structures of these nanowires are optimized, we used FLAPW method [61-63] to calculate the electronic structure and magnetic properties such as saturation magnetization and magnetocrystalline anisotropy energies. The details of these calculations are similar to those described in Chapter 4.

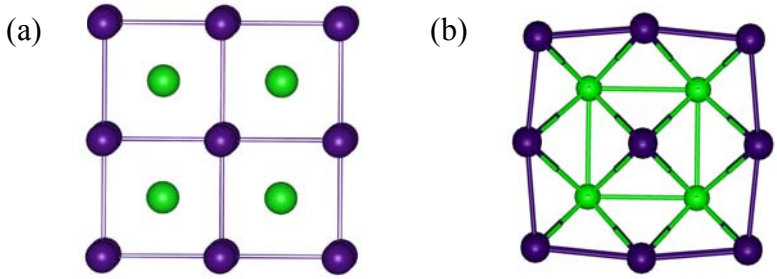


Figure 6.2 The cross sections of the $Co_4Fe_9$: (a) before relaxation; and (b) after optimization. The green and dark blue balls represent Co atoms and Fe atoms, respectively.

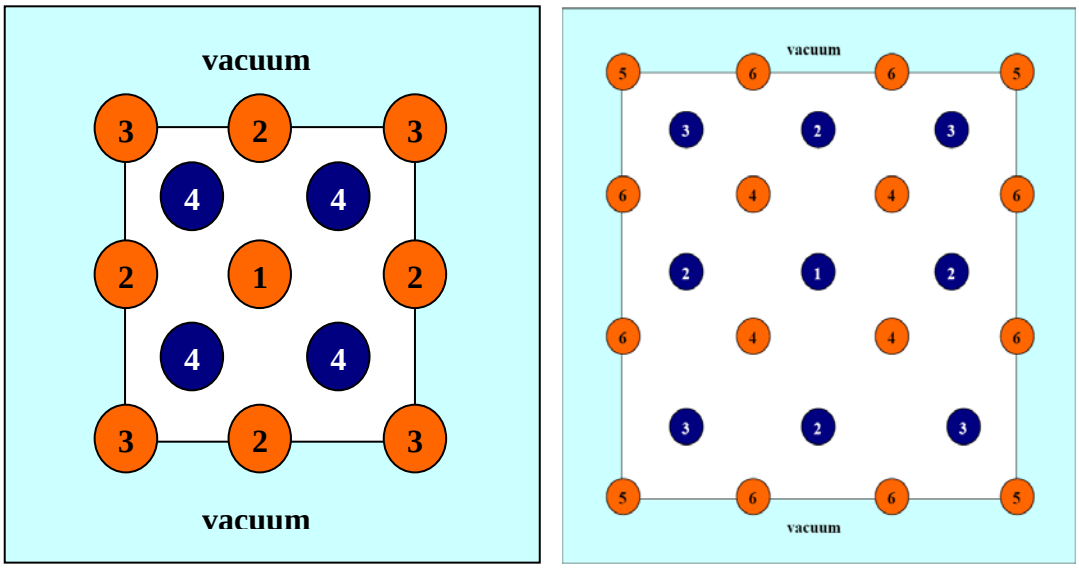


Figure 6.3 Top-down views of the 2×2×1 (left) and 3×3×1 (right) FeCo nanowires. Different colors indicate different layers of the atoms and the numbers inside the atoms represent different types of local symmetry.

From the perspective of local symmetry, the atoms in a supercell can be categorized into four types in systems $Fe_4Co_9$, $Fe_9Co_4$ and $Fe_{13}$, and six types in systems $Fe_9Co_{16}$, $Fe_{16}Co_9$ and $Fe_{25}$, as shown in Figure 6.3, where the atoms with different colors represent the atoms in different layers from a top-down view along *z* axis. The numbers inside the atoms represent different types of local symmetry. Later on, we shall

find that the magnetic moments of atoms are highly dependent on where they reside and their local symmetry.

## 6.2 Stability

To check if the FeCo nanowires are stable, we calculated their cohesive energies and formation energies. The cohesive energy $E_{coh}$ and formation energy $E_{for}$ are defined as

$$E_{coh} = (E_{Fe_mCo_n} - mE_{Fe}^{isolated} - nE_{Co}^{isolated})/(m+n) \quad (6.1)$$

and

$$E_{for} = (E_{Fe_mCo_n} - m\mu_{Fe} - n\mu_{Co})/(m+n), \quad (6.2)$$

respectively. Here $E_{Fe_mCo_n}$ is the total energy of structurally optimized nanowire $Fe_mCo_n$ with m Fe atoms and n Co atoms. $E_{Fe}^{isolated}$ and $E_{Co}^{isolated}$ are the energies of an isolated Fe atom and an isolated Co atom from our calculations and $\mu_{Co}$ and $\mu_{Fe}$ represent chemical potentials of pure Co and Fe metals, respectively, as mentioned in Chapter 4. The value of the cohesive energy determines if the nanowires are stable against isolated Fe and Co atoms while the value of the formation energy reflects if the nanowires are stable against pure Fe or Co metals. A negative value means the nanowire is stable, otherwise it is unstable.

Our calculated cohesive energies and formation energies of these nanowires are shown in Table 6.2. We can see that all the FeCo nanowires under investigation are stable against isolated atoms because they all have negative cohesive energies. But they

are unstable compared to the bulk iron or cobalt metals since they have positive formation energies. Nevertheless, it is still feasible that these nanowires can be synthesized by some experimental techniques [111-113] at a non-equilibrium environment, considering their small positive formation energies. Figure 6.4 shows the TEM image of FeCo nanowires synthesized by our collaborating experimental group [114]. At high temperatures, however, the nanowires may segregate into pure metals or alloys. On the other hand, the nanowires with larger diameters are more stable than the nanowires with smaller diameters, as evidenced by the smaller cohesive energies and formation energies of the thinner nanowires.

Table 6.2 Cohesive energies and formation energies of FeCo nanowires.

| System | Cohesive Energy (eV/atom) | Formation Energy (eV/atom) |
|---|---|---|
| $Fe_9Co_4$ | -6.85 | 0.96 |
| $Co_9Fe_4$ | -6.40 | 0.96 |
| $Fe_{13}$ | -7.18 | 1.00 |
| $Fe_{16}Co_9$ | -7.06 | 0.69 |
| $Co_{16}Fe_9$ | -6.73 | 0.69 |
| $Fe_{25}$ | -7.45 | 0.73 |

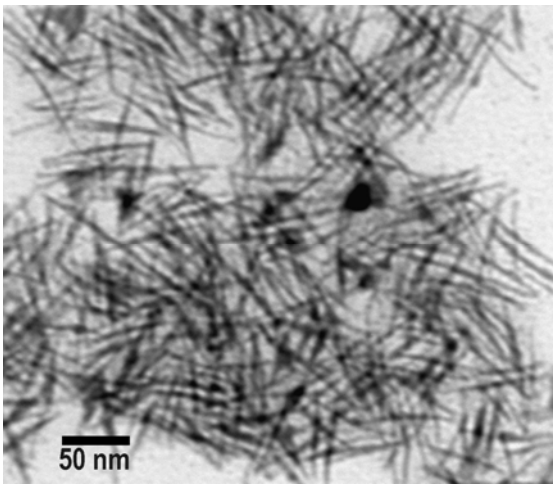


Figure 6.4 TEM image of FeCo nanowires. Reference [114].

## 6.3 Magnetic Moments

It is found that the magnetic moments of atoms are highly dependent on where they reside in the wire as shown in Tables 6.3 and 6.4. Generally, for the same type of atoms, the magnetic moments become smaller if they are closer to the center of the wire. For example, for system $Fe_9Co_4$, the Fe atom sitting in the center of the wire has magnetic moment of 2.64 $\mu_B$, much smaller than the magnetic moments in the outer part of the wire. This is reasonable since the behavior of the atoms in the inner part of the wire should be closer to the atoms in bulk materials (magnetic moments of Fe and Co atoms in bulk are 2.16 $\mu_B$ and 1.56 $\mu_B$, respectively from our previous calculations).

Table 6.3 Magnetic moments of atoms in different symmetric positions for systems $Fe_4Co_9$, $Fe_9Co_4$ and $Fe_{13}$. Numbers 1-4 represent different symmetric positions as shown in the left plot in Fig. 6.3.

| System | Atomic magnetic moments ($\mu_B$) | | | |
|---|---|---|---|---|
| | 1 | 2 | 3 | 4 |
| $Fe_4Co_9$ | 1.69 | 1.86 | 1.94 | 2.52 |
| $Fe_9Co_4$ | 2.63 | 2.88 | 2.90 | 1.62 |
| $Fe_{13}$ | 2.02 | 2.93 | 2.85 | 2.16 |

Table 6.4 Magnetic moments of atoms in different symmetric positions for systems $Fe_9Co_{16}$, $Fe_{16}Co_9$ and $Fe_{25}$. Numbers 1-6 represent different symmetric positions as shown in the right plot in Fig. 6.3.

| System | Atomic magnetic moments ($\mu_B$) | | | | | |
|---|---|---|---|---|---|---|
| | 1 | 2 | 3 | 4 | 5 | 6 |
| $Fe_9Co_{16}$ | 2.79 | 2.73 | 2.62 | 1.87 | 2.08 | 2.20 |
| $Fe_{16}Co_9$ | 1.74 | 1.71 | 1.68 | 2.75 | 2.96 | 2.97 |
| $Fe_{25}$ | 2.17 | 2.64 | 2.34 | 2.65 | 3.18 | 3.16 |

Compared to bulk materials, the average magnetic moment per atom of the same specie in these systems is larger due to the symmetry broken by introducing surface area. For instance, the average magnetic moment of Fe atom in $Fe_{16}Co_9$ is 2.91 $\mu_B$, significantly larger than the magnetic moment of Fe atom in bulk bcc iron, 2.16 $\mu_B$. This is also true for the two reference systems, $Fe_{13}$ and $Fe_{25}$.

## 6.4 Magnetocrystalline Anisotropy Energies

The magnetocrystalline anisotropy energies of these FeCo nanowires are calculated with the torque method [87] described in Chapter 4 using the optimized geometric structures obtained by VASP calculations.

Table 6.5 Magnetocrystalline anisotropy energies of FeCo nanowires.

| System | Magnetocrystalline anisotropy Energy (meV/cell) |
|---|---|
| $Fe_9Co_4$ | 0.81 |
| $Co_9Fe_4$ | 1.67 |
| $Fe_{13}$ | -0.58 |
| $Fe_{16}Co_9$ | -0.60 |
| $Co_{16}Fe_9$ | -0.41 |
| $Fe_{25}$ | -0.44 |

Table 6.5 shows the results of our calculation. We can see from this table that except for $Fe_9Co_4$ and $Co_9Fe_4$, the easy axis of the magnetocrystalline anisotropy for these nanowires is actually perpendicular to the wire direction, since they have negative magnetocrystalline anisotropy energies. Comparing $Fe_9Co_4$ and $Fe_{16}Co_9$, we can see that when the radius of the nanowires increases, the easy axis changes from the wire direction (z-axis in our calculations) to the direction perpendicular to the wire (x-axis in our calculations). This is also true for $Co_9Fe_4$ and $Co_{16}Fe_9$ but not the case for $Fe_{13}$ and $Fe_{25}$, where increasing dimension does not change the easy axis of magnetization. Comparing the 2×2×1 systems with 3×3×1 systems, we can also conclude that with

increasing radius of the nanowires, the magnetocrystalline anisotropy energies actually decrease. If we take into account the volumes of the nanowires, this effect is more evident. Compared to the magnetocrystalline anisotropy energies of the bulk FeCo alloys as we discussed in Chapter 4, the magnetocrystalline anisotropy energies of the FeCo nanowires are significantly larger. Of course, when the radius of a wire becomes larger and larger, it should converge to the bulk value.

Considering that the nanowires may grow on different substrates, it is expected that their lattice constant along certain direction will vary to reduce the stress produced by the lattice mismatch between the nanowires and the substrates. We also expect the magnetocrystalline anisotropy energy of the nanowires will change because of the lattice change. To simulate the effects of substrates on the magnetocrystalline anisotropy, we have calculated the magnetocrystalline anisotropy energies of $Co_4Fe_9$ nanowires with different lattice constant along the wire. The nanowire structures are again optimized with pre-set lattice constants along the wire axis before the magnetocrystalline anisotropy energies are calculated. Table 6.6 shows the results of the magnetocrystalline anisotropy energies from our calculations.

It is interesting that when the lattice constant along wire direction is shortened or elongated, the magnetocrystalline anisotropy easy axis of $Co_4Fe_9$ nanowire changed from parallel to the wire axis to perpendicular to the wire. This change may have important consequences: when combined with the shape anisotropy of the nanowires, as we will discuss in the following section, the total magnetic anisotropy will be either strengthened or compromised, depending on the directions of these two anisotropies.

Table 6.6 Magnetocrystalline anisotropy energies of $Co_4Fe_9$ nanowires with different lattice constant along the wire direction (z axis in our calculation). The percentage of change of lattice constant compared to our optimized lattice constant is listed in the parentheses.

| lattice length (Å) | Magnetocrystalline anisotropy Energy (meV/cell) |
|---|---|
| 4.69 (-6%) | -0.991 |
| 4.84 (-3%) | -0.936 |
| 4.99 (0%) | 0.810 |
| 5.14 (+3%) | -0.695 |
| 5.29 (+6%) | -2.849 |
| 5.44 (+9%) | -3.059 |

We can also see from the table that the magnetocrystalline anisotropy energy varies with varying lattice constant along the wire axis. For example, the value of the magnetocrystalline anisotropy energy of the nanowire with 9% increased lattice constant c will be about four times larger than that of the structurally optimized nanowire.

Based on our results, we can deduce that it is possible that both the direction and the value of the magnetocrystalline anisotropy energy of these FeCo nanowires can be engineered by varying the substrate during the growth of the nanowires. Their magnetic anisotropy can be further engineered by combining the magnetocrystalline anisotropy and the shape anisotropy.

## 6.5 Shape Anisotropy Energies

Shape anisotropy is another source of magnetic anisotropy which origins in the non-spherical shape of a ferromagnetic sample, associated with the magnetostatic

energy. For a non-spherical sample, it will be easier to magnetize it along a long axis than along a short axis because the demagnetizing field along a short axis is stronger than along a long axis. The shape anisotropy energy, i.e. the energy difference along these axes, can be calculated from the magnetostatic energies along these two magnetization directions.

We computed the shape anisotropy energies of the FeCo nanowires with two different methods. The first method is a theoretical approach we derived from the classical electromagnetic theory. The second method approximates the nanowires as prolate spheroids and uses empirical formula to calculate their shape anisotropy energy.

To derive the formula to calculate the shape anisotropy energy in the first, theoretical method, we note that the magnetostatic energy $u$ associated with a permanent magnetic moment in an external magnetic field can be expressed as [93]

$$u = -\vec{m} \cdot \vec{B}, \tag{6.3}$$

where $\vec{m}$ is magnetic moment and $\vec{B}$ is magnetic induction. Therefore, the magnetostatic energy of the nanowires per supercell is just the summation of the magnetostatic energies associated with all the magnetic moments inside the nanowires, i.e.,

$$U = \sum u = -a \sum_{i=1}^{q} \sum_{\substack{j=1 \\ j \neq i}}^{\infty} \vec{m}_i \cdot \vec{B}_j, \tag{6.4}$$

where q is the number of the atoms inside the supercell and $a$ is a constant introduced to avoid double counting inside the supercell. So $a = 1/2$ if atom $j$ is inside the

supercell and $a = 1$ otherwise. The magnetic induction $\vec{B}_j$ originating from magnetic moment $\vec{m}_j$ is evaluated as

$$B_j(\vec{r}) = \frac{\mu_0}{4\pi}\left[\frac{3\vec{n}(\vec{n}\cdot\vec{m}_j) - \vec{m}_j}{|\vec{r}|^3}\right]. \tag{6.5}$$

Here $\vec{n}$ is a unit vector in the direction $\vec{r}$ ($\vec{n} = \vec{r}/|\vec{r}|$). Therefore equation (6.4) becomes

$$U = -a\frac{3\mu_0}{4\pi}\sum_{i=1}^{q}\sum_{\substack{j=1\\ j\neq i}}^{\infty}\frac{(\vec{n}_{ij}\cdot\vec{m}_i)(\vec{n}_{ij}\cdot\vec{m}_j)}{|\vec{r}_{ij}|^3}. \tag{6.6}$$

And the shape anisotropy energy can be written as

$$\begin{aligned} E_{ani\_shape} &= U(\rightarrow) - U(\uparrow) \\ &= -a\frac{3\mu_0}{4\pi}\sum_{i=1}^{q}\sum_{\substack{j=1\\ j\neq i}}^{\infty}\frac{\vec{m}_i\vec{m}_j(x_{ij}^2 - z_{ij}^2)}{|\vec{r}_{ij}|^5}, \end{aligned} \tag{6.7}$$

where $U(\rightarrow)$ and $U(\uparrow)$ are the magnetostatic energies when all the magnetic moments are aligned perpendicular to the wire ((100) direction) and parallel to the wire ((001) direction), respectively. $x_{ij} = x_i - x_j$ and $z_{ij} = z_i - z_j$ are the differences of the $x$ coordinates and $z$ coordinates, respectively, of atom $i$ and atom $j$ in the Cartesian coordinate system.

In the second, empirical method, the magnetostatic energy $E_D$ (in erg/cm$^3$) associated with a particular magnetization direction can be expressed as [7]

$$E_D = \frac{1}{2}N_d M_s^2 \quad \text{erg/cm}^3, \tag{6.8}$$

where $N_d$ is the demagnetization factor along the magnetization direction and $M_s$ is the saturation magnetization of the nanowire in unit of emu/cm$^3$.

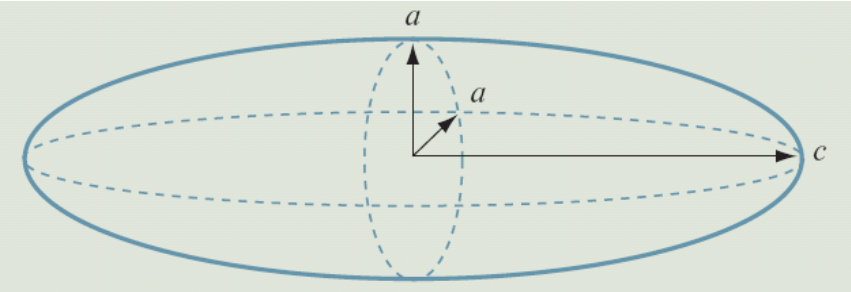


Figure 6.5 An illustration of a prolate spheroid

The nanowires can be approximated as prolate spheroids (as shown above in Figure 6.5, the demagnetization factor can only be calculated exactly for an ellipsoid, of which prolate spheroid is one type) with high aspect ratio c/a. In this case, the demagnetization factor along the hard axis, perpendicular to the wire axis, is equal to 2 $\pi$, and the demagnetization factor along the easy axis, parallel to the wire axis, is 0. The exact solutions for the demagnetization factors for a prolate spheroid, suppose c/a=r, are provided as follows:

$$N_c = \frac{4\pi}{(r^2-1)}\left[\frac{r}{\sqrt{r^2-1}}\ln(r+\sqrt{r^2-1})-1\right]; \tag{6.9}$$

$$N_a = N_b = \frac{4\pi - N_c}{2}. \tag{6.10}$$

Based on these equations, the shape anisotropy energy of these nanowires can be written as

$$E_{shape} = \frac{1}{2}(N_a - N_c)M_s^2 = \pi M_s^2 \text{ erg/cm}^3. \tag{6.11}$$

Notice that the calculation of shape anisotropy with this method is approximate. The result becomes closer to the theoretical value with higher c/a value.

Table 6.7 Shape anisotropy energies for the FeCo nanowires. As comparison, the magnetocrystalline anisotropy energies are also listed with the same units.

| System | Shape anisotropy energy ($10^6$ J/m$^3$) | | Magnetocrystalline anisotropy energy ($10^6$ J/m$^3$) |
|---|---|---|---|
| | Theoretical | Empirical | |
| $Fe_9Co_4$ | 4.39 | 4.06 | 1.53 |
| $Co_9Fe_4$ | 3.04 | 2.65 | 3.14 |
| $Fe_{13}$ | 4.34 | 4.25 | -1.06 |
| $Fe_{16}Co_9$ | 3.76 | 2.81 | -0.49 |
| $Co_{16}Fe_9$ | 2.87 | 1.80 | -0.33 |
| $Fe_{25}$ | 3.90 | 2.80 | -0.19 |

The results of our calculations are shown in Table 6.7. To compare them with our calculated magnetocrystalline anisotropy energies, we converted both types of magnetic anisotropy energies to the same SI unit, i.e., J/m$^3$. Comparing the results of the shape anisotropy energies calculated from both methods, we can see that the empirical method is accurate for approximately evaluating the shape anisotropy energy of nanowires with small diameters. For nanowires with larger diameters such as the $3\times3\times1$ systems under our consideration, they are less accurate and have an error of calculation around 30% compared to our calculated theoretical values. The reason of the error originates from our approximation, in which high c/a ratio is an assumption. In our

study, the c/a values of $2\times2\times1$ systems are larger than those of $3\times3\times1$ systems. Thus the approximation is more accurate in the $2\times2\times1$ systems. Nevertheless, the shape anisotropy energies from the empirical method are in the same magnitude with those calculated from the theoretical method.

It is obvious that for these FeCo nanowires, shape anisotropy is the dominant magnetic anisotropy compared with the magnetocrystalline anisotropy. As we mentioned earlier, the easy axes of magnetocrystalline anisotropy for these nanowires except $Fe_9Co_4$ and $Co_9Fe_4$ are actually perpendicular to the wire direction. As a result, when both types of anisotropies are present together, the direction of the easy magnetization of these nanowires is along the wire axis. For systems $Fe_9Co_4$ and $Co_9Fe_4$, the shape anisotropy will be reinforced by the magnetocrystalline anisotropy, producing a larger total magnetic anisotropy. For other systems, because of the perpendicular directions of the shape anisotropy and magnetocrystalline anisotropy, the shape anisotropy will be compromised by the magnetocrystalline anisotropy.

In summary, we have performed first-principles calculations to study the structural, electronic and magnetic properties of FeCo nanowires. FeCo nanowires with larger diameters are more stable than those with smaller diameters. It is found that the average magnetic moment per atom of the same specie in FeCo nanowires is larger compared to bulk materials due to the symmetry broken by introducing surface area. By calculating the magnetocrystalline anisotropy energies and shape anisotropy energies of these FeCo nanowires, we found that shape anisotropy is the dominant magnetic anisotropy in these nanowires. Our study implies that both the direction and the value of

the magnetocrystalline anisotropy energy of these FeCo nanowires can be engineered by varying the substrate during the growth of the nanowires. Their magnetic anisotropy can be further engineered by combining the magnetocrystalline anisotropy and the shape anisotropy.

# CHAPTER 7

# SUMMARY

In this dissertation, density-functional-theory based first-principles study has been performed on the hard/soft nanocomposite magnetic $SmCo_5$/Co(Fe) systems. The PAW method implemented in VASP, the FLAPW method and the LMTO method have been employed in our calculations. We have investigated the effects of soft phase properties and interfacial conditions on the strength of the exchange coupling between soft and hard phase materials. Calculations to study the FeCo nanowires as potential high performance permanent magnets or as potential soft phase materials in a nanocomposite magnetic system have also been carried out.

In the study of soft phase effects, the structural, electronic and magnetic properties of FeCo alloys have been investigated. The FeCo alloys were initially set with bcc-, hcp-, or fcc-type structures and then fully relaxed to find their lowest total energies and corresponding ground state structures. For the systems having two or more configurations, we have considered all possible non-equivalent configurations and identified the configuration with lowest total energy as the ground state structure for the system. We found that only bcc-type FeCo alloys are stable, whereas fcc- and hcp-type alloys are not. For the stable bcc-type alloys, it is found that they prefer non-cubic geometries in a wide composition range. This produces appreciable uniaxial magnetic

anisotropy, according to our calculations, and facilitates inter-phase magnetic interaction and enhances the overall magnetization in exchange coupled hard/soft nanocomposite systems. Specifically, we found that $Fe_{11}Co_5$, $Fe_{12}Co_4$ and $Fe_{13}Co_3$ alloys have sizable magnetocrystalline anisotropy energies with high magnetizations and they may be used as target soft phase materials in the nanocomposite system.

On the effects of interfacial conditions on the exchange coupling, we have used layered $SmCo_5$/Co(Fe) as a prototype system to study the exchange coupling strength between the soft phase material Co or FeCo alloys and hard phase material $SmCo_5$. The exchange coupling strength is described in two complimentary ways. In the first method, we performed noncollinear magnetic structure calculations to simulate the demagnetization process of the magnetic system. In the second method, we directly calculated the site-to-site exchange parameters across the hard/soft interface. Through both methods, we found that the exchange coupling in $SmCo_5$/Co is enhanced by introducing Fe atom in the soft phase. However, the introduction of Fe atom into hard phase $SmCo_5$ will have different effects, depending on the soft phase composition. For a pure hcp Co soft phase, it enhances the exchange coupling. But for the FeCo alloys as soft phase, it leads to the degradation of the exchange coupling.

On the exploration of FeCo nanowires as potential high performance permanent magnets or potential soft phase material in a nanocomposite magnetic system, we studied their stability, the electronic and magnetic properties. It is found that the nanowires with larger diameters are more stable than the nanowires with smaller diameters. We also calculated the magnetocrystalline anisotropy energies and shape

anisotropy energies of these FeCo nanowires and found that shape anisotropy is the dominant magnetic anisotropy in these nanowires. Depending on the relations of the axes of shape anisotropy and magnetocrystalline anisotropy, the total magnetic anisotropy will be either enhanced or compromised.

As discussed in this dissertation, our research work completed so far has provided guidance on the effects of the soft phase material properties and interfacial conditions on the exchange coupling between soft and hard phases. On the other hand, there still remain many important areas for future research. In this study, we only considered Fe doping. The effects of doping by other materials on the exchange coupling should also be studied in detail. Apart from the layered and abrupt interface structures, other interface structures such as a gradient interface or core-shell structures will also be interesting topics. Furthermore, the more realistic $Sm_2Co_{17}$/Fe model will be investigated as we mentioned in the beginning.

REFERENCES


[1] E. F. Kneller, and R. Hawig, IEEE Trans. Magn. **27**, 3588 (1991).

[2] Hao Zeng, Jing Li, J. P. Liu, Z. L. Wang, and Shouheng Sun, Nature 420, 395 (2002).

[3] R. Skomski, and J. M. D. Coey, Phys. Rev. B **48**, 15812 (1993).

[4] R. Skomski, and J. M. D. Coey, IEEE Trans. Magn. **30**, 607 (1994).

[5] P. Hohenberg, and W.Khon, Phys. Rev. **136**, B864 (1964).

[6] W. Kohn, and L. J. Sham, Phys. Rev. **140**, A1133 (1965).

[7] B. D. Cullity, *Introduction to magnetic materials*, Addison-Wesley Pub. Co., Reading, Mass., 1972.

[8] Nicola A. Spaldin, *Magnetic materials: fundamentals and device applications*, Cambridge University Press, Cambridge, U.K., 2003.

[9] Robert C. O'Handley, *Modern Magnetic Materials: Principles and Applications*, John Wiley and Sons, New York, 1999.

[10] R. Skomski and J. M. D. Coey, *Permanent Magnetism,* Institute of Physics, Bristol, 1999.

[11] http://www.aacg.bham.ac.uk/magnetic_materials/hysteresis.htm.

[12] http://www.aacg.bham.ac.uk/magnetic_materials/history.htm.

[13] R. Skomski and J. M. D. Coey, IEEE Trans. Magn. 30, 607 (1996).

[14] Z.S. Shan, J.P. Liu, V.M. Chakka, H. Zeng, and J. S. Jiang, IEEE Trans. Magn. 38, 2907 (2002).

[15] Z. J. Guo, J. S. Jiang, J. E. Pearson, S. D. Bader, and J. P. Liu, Appl. Phys. Lett. 81, 2029 (2002).

[16] G. Asti, M. Solzi, M. Ghidini, F.M. Neri, Phys. Rev. B 69, 174401 (2004).

[17] M. Born and J. R. Oppenheimer, Ann. Phsik **84**, 457 (1927).

[18] M. Born and K. Huang, *Dynamical Theory of Crystal Lattices*, Oxford University Press, Oxford, 1954.

[19] R. M. Martin, *Electronic Structure: Basic Theory and Practical Methods*, Cambridge University Press, Cambridge, UK, 2004.

[20] M. Levy, Proc. Nat. Acad. Sci. USA **76**, 6062 (1979).

[21] M. Levy, Phys. Rev. A **26**, 1200 (1982).

[22] M. Levy and J. P. Perdew, in *Density Functional Methods in Physics*, edited by R. M. Dreizler and J. da Providencia, Plenum, New York, 1985, p. 11.

[23] E. Lieb, in *Physics as Natural Philosophy*, edited by A. Shimony and H. Feshback, MIT Press, Cambridge, 1982, p. 111.

[24] E. Lieb, Int. J. Quant. Chem. **24**, 243 (1983).

[25] E. Lieb, in *Density Functional Methods in Physics*, edited by R. M. Dreizler and J. da Providencia, Plenum, New York, 1985, p. 31.

[26] J.P. Perdew and A. Zunger, Phys. Rev. B **23**, 5048 (1981).

[27] J.P. Perdew, R. G. Parr, M. Levy and J. L. Balduz, Jr., Phys. Rev. Lett **49**, 1691 (1982).

[28] V. I. Anisimov, J. Zaanen, and O. K. Andersen, Phys. Rev. B **44**, 943 (1991).

[29] P. Raybaud, G. Kresse, J. Hafner and H. Toulhoat, J. Phys.: Condens. Matter **9**, 11085 (1997).

[30] J. P. Perdew and Y. Wang, Phys. Rev. B 33, 8800 (1986).

[31] J. P. Perdew in Electronic Structure of Solids, edited by Ziesche and H. Eschrig Akademie Verlag, Berlin, 1991.

[32] J. P. Perdew and Y. Wang, Phys. Rev. B 45, 13244 (1992).

[33] J. P. Perdew and K. Burke, Int. J. Quantum Chem. 57, 309 (1996).

[34] J. P. Perdew, K. Burke, and Y. Wang, Phys. Rev. B 54, 16533 (1996).

[35] J. P. Perdew, K. Burke, and M. Ernzerhof, Phys. Rev. Lett. 77, 3865 (1996).

[36] J. Cho and M. Scheffler, Phys. Rev. B **53**, 10685 (1996).

[37] D. J. Singh, W. E. Pickett, and H. Krakauer, Phys. Rev. B **43**, 11628 (1991).

[38] T. C. Leung, C. T. Chan, and B. N. Harmon, Phys. Rev. B **44**, 2923 (1991).

[39] J. Zhu, X. W. Wang, and S. G. Louie, Phys. Rev. B **45**, 8887 (1992).

[40] M. Körling and J. Häglund, Phys. Rev. B **45**, 13293 (1992).

[41] F. Bloch, Z. Phys. **52**, 555 (1928).

[42] N. W. Ashcroft and N. D. Mermin, *Solid State Physics*, Holt Saunders, Philadelphia. 1976.

[43] A. Baldereschi, Phys. Rev. B **7**, 5212 (1973).

[44] D. J. Chadi and M. L. Cohen, Phys. Rev. B **8**, 5747 (1973).

[45] H. J. Monkhorst and J. D. Pack, Phys. Rev. B **13**, 5188 (1976). Phys. Rev. B 16, 1748 (1977).

[46] W. E. Pickett, Comput. Phys. Rep. 9, 115 (1989).

[47] J. C. Phillips, Phys. Rev. 112, 685 (1958).

[48] J. C. Phillips and L. Kleinman, Phys. Rev. 116, 287 (1959).

[49] W. A. Harrison, Pseudopotentials in the Theory of Metals, Benjamin, New York, 1966.

[50] V. Heine, in Solid State Physics, edited by H. Ehrenreich, F. Seitz, and D. Turnbull, Academic, New York, 1970, p. 1.

[51] M. L. Cohen and V. Heine, in Solid State Physics, edited by H. Ehrenreich, F. Seitz, and D. Turnbull, Academic, New York, 1970, p. 37.

[52] M. T. Yin and M. L. Cohen, Phys. Rev. B 25, 7403 (1982).

[53] P. E. Blöchl, Phys. Rev. B 41, 5414 (1990).

[54] D. Vanderbilt, Phys. Rev. B 41, 7892 (1990).

[55] K. Laasonen, A. Pasquarello, R. Car, C. Lee, and D. Vanderbilt, Phys. Rev. B 47, 10142 (1993).

[56] G. Kresse and J. Hafner, Phys. Rev. B 48, 13115 (1993).

[57] G. Kresse and J. Hafner, J. Phys.: Condens. Matter 6, 8245 (1994).

[58] J. Yamauchi, M. Tsukada, S. Watanabe, and O. Sugino, Phys. Rev. B 54, 5586 (1996).

[59] A. Dal Corso, A. Pasquarello, and A. Baldereschi, Phys. Rev. B 56, R11369 (1997).

[60] G. Kresse and D. Joubert, Phys. Rev. B **59**, 1758 (1999).

[61] E. Wimmer, H. Krakauer, M. Weinert, and A. J. Freeman, Phys. Rev. B **24**, 864 (1981).

[62] M. Weinert, E. Wimmer, and A. J. Freeman, Phys. Rev. B **26**, 4571 (1982).

[63] M. Weinert, J. Math. Phys. **22**, 2433 (1981).

[64] O. K. Andersen, Phys. Rev. B **12**, 3060 (1975).

[65] D. D. Koelling and G. O. Arbman, J. Phys. F **5**, 2041 (1975).

[66] D. J. Singh, *Planewaves, Pseudopotentials, and the LAPW Method*, Kluwer Academic Publishers, Boston, 1994.

[67] J. C. Slater, Phys. Rev. **51**, 846 (1937).

[68] J. C. Slater, Advances in Quantum Chemistry **1**, 35 (1964).

[69] T. L. Loukes, *The Augmented-Plane-Wave Method*, Benjamin, New York, 1967.

[70] P. E. Blöchl, Phys. Rev. B **50**, 17953 (1994).

[71] N. A. W. Holzwarth, G. E. Matthews, R. B. Dunning, A. R. Tackett, and Y. Zeng, Phys. Rev. B **55**, 2005 (1997).

[72] O. Gunnarsson, O. Jepsen, and O. K. Andersen, Phys. Rev. B **27**, 7144 (1983).

[73] H. Skriver, *The LMTO Method*, Springer, New York, 1984.

[74] Dangxin Wu, Qiming Zhang, J. Ping Liu, Dingwang Yuan, and Ruqian Wu, Appl. Phys. Lett. **92**, 052503 (2008).

[75] G. Kresse and J. Hafner, Phys. Rev. B **47**, R558 (1993).

[76] G. Kresse and J. Hafner, Phys. Rev. B **49**, 14251 (1994).

[77] G. Kresse and J. Furthmüller, Phys. Rev. B **54**, 11169 (1996).

[78] G. Kresse and J. Furthmüller, Comput. Mater. Sci. 6, 15 (1996).

[79] R. Drautz, A. Díaz-Orbiz, M. Fähnle, and H. Dosch, Phys. Rev. Lett. **93**, 067202 (2004).

[80] C.L Fu and M. Krcmar, Phys. Rev. B **74**, 174108 (2006).

[81] R.W.G. Wyckoff, *Crystal Structures*, Interscience Publishers, New York, 1963.

[82] R. Drautz, A. Díaz-Orbiz, M. Fähnle, and H. Dosch, Phys. Rev. Lett. **93**, 067202 (2004).

[83] R. Drautz and A. Díaz-Orbiz, Phys. Rev. B **73**, 224207 (2006).

[84] G. H. O. Daalderop, P. J. Kelly, and M. F. H. Schuurmans, Phys. Rev. B **42**, 1553 (1990).

[85] A. R. Mackintosh and O. K. Andersen, in *Electrons at the Fermi Surface*, edited by M. Springford, Cambridge University Press, Cambridge, 1980.

[86] X. D. Wang, D. S. Wang, R. Q. Wu, and A. J. Freeman, J. Magn. Magn. Mater. **159**, 337 (1996).

[87] X. D. Wang, R. Q. Wu, D. S. Wang, and A. J. Freeman, Phys. Rev. B **54**, 61 (1996).

[88] R. Q. Wu and A. J. Freeman, J. Magn. Magn. Mater. **200**, 498 (1999).

[89] Dangxin Wu, Qiming Zhang, J. Ping Liu, and Renat F. Sabirianov, J. Nanosci. Nanotechnol. **8**, 3036 (2008)

[90] O. N. Mryasov, R. F. Sabiryanov, A. J. Freeman, and S. S. Jaswal, Phys. Rev. B **56**, 7255 (1997).

[91] A. I. Liechtenstein, M. I. Katsnelson, V. P. Antropov, and V. A. Gubanov, J. Magn. Magn. Mater. **67**, 65 (1987).

[92] Dangxin Wu, Qiming Zhang, J. Ping Liu, and Ruqian Wu, unpublished.

[93] J. D. Jackson, Classical Electrodynamics, 3rd ed., John Wiley & Sons, New York, 1998.

[94] J. P. Perdew and A. Zunger, Phys. Rev. B **23**, 5048 (1981).

[95] D. M. Ceperley and B. J. Alder, Phys. Rev. Lett. **45**, 566 (1980).

[96] J. Zhang, K. Takahashi, R. Gopalan, and K. Hono, Appl. Phys. Lett. **86**, 122509 (2005).

[97] Y. Choi, J. S. Jiang, Y. Ding, R. A. Rosenberg, J. E. Pearson, S. D. Bader, A. Zambano, M. Murakami, I. Takeuchi, Z. L. Wang, and J. P. Liu, Phys. Rev. B **75**, 104432 (2007).

[98] A. J. Zambano, H Oguchi, I. Takeuchi, Y. Choi, J. S. Jiang, J. P. Liu, S. E. Lofland, D. Josell and L. A. Bendersky, Phys. Rev. B **75**, 144429 (2007).

[99] J. H. van Vleck, Phys. Rev. **52**, 1178 (1937).

[100] J. G. Gay, R. Richter, Phys. Rev. Lett. **56**, 2728 (1986).

[101] J. G. Gay, R. Richter, J. Appl. Phys. **61**, 3362 (1987).

[102] M. F. Collins and J. B. Forsyth, Philos. Mag. **8**, 401 (1963).

[103] R. H. Victora and L. M. Falicov, Phys. Rev. B **30**, 259 (1984).

[104] C. H. Park, I. G. Kim, B. C. Lee and J. I. Lee, Phys. Stat. sol. (b) **241**, 1419 (2004).

[105] L. I. Mendelsohn, F. E. Luborsky, and T. O. Paine, J. Appl. Phys. **26**, R1274 (1955).

[106] R. B. Falk, J. Appl. Phys. **37**, R1108 (1966).

[107] D. J. Craik and R. Lane, J Appl. Phys. **38**, R1269 (1967).

[108] T. Thurn-Albrecht, J. Schotter, G. A. Kästle, N. Emley, T. Shibauchi, L. Krusin-Elbaum, K. Guarini, C. T. Black, M. T. Tuominen, and T. P. Russell, Science **290**, 2126 (2000).

[109] D. J. Sellmyer, M. Zheng, and R. Skomski, J. Phys.: Condens. Matter **13**, R433 (2001).

[110] T. Maurer, F. Ott, G. Chaboussant, Y. Soumare, J. –Y. Piquemal, and G. Viau, Appl. Phys. Lett. **91**, 172501 (2007).

[111] Qingfeng Zhan, Ziyu Chen, Desheng Xu, Fashen Li, Henry Kunkel, Xuezhi Zhou, Roy Roshko, and Gwyn Williams, Phys. Rev. B **66**, 134436 (2002).

[112] H. L. Su, G. B. Ji, S. L. Tang, W. Chen, Z. Li, B. X. Gu, and Y. W. Du, J. Appl. Phys. **97**, 116104 (2005).

[113] Lin Cao, Xinping Qiu, Jingbo Ding, Hulin Li, and Liquan Chen, J. Mater. Sci. **41**, 2211 (2006).

[114] J. P. Liu, private communication.

# BIOGRAPHICAL INFORMATION

Dangxin Wu received his Bachelor degree in Materials Science from Sichuan University in China in 1998. He received his Master of Science degree in Physics in August 2005 from the University of Texas at Arlington. He continued his study in the same university and received his Ph. D. degree in Physics in August 2008.